Theory and Modelling of Electron Transport in Molecular-Scale Condensed Matter

Asma Mohammed Alajmi

Ph.D. Thesis in Physics

Department of Physics, Lancaster University, UK

2025

This Thesis is submitted in partial fulfillment of the requirements for the degree of Doctor of Philosophy

Declaration

This thesis is all my work and effort and has not been submitted in substantially the same form for the award of a higher degree elsewhere. Other sources of information have been used, and they have been acknowledged. This thesis documents work carried out between October 2022 and February 2025 at Lancaster University under the supervision of Professor Colin J. Lambert and Dr. Ali Ismael with the support of Prince Sattam bin Abdulaziz University, KSA.

Asma Alajmi

2025

Acknowledgement

My great thanks to ALLAH for his mercy and blessing. I could not have achieved what I have done without ALLAH.

I am writing to express my deepest gratitude to Prof. Colin John Lambert for his support, kindness, and patience. Also, I am grateful for his tutorials, which provide me with a deep understanding of molecular electronics and would be helpful for my future study and research.

I would also like to thank Dr. Ali Ismael for his encouragement, valuable guidance, insightful comments and suggestions, and dedicated time throughout my PhD journey. Also, many thanks to the theory of molecular-scale groups and the collaborating experimental groups. I thank all my friends and colleagues in Colin's group.

I express my heartfelt gratitude to my sponsor, the Saudi Ministry of Higher Education, the Saudi Cultural Mission in London, and Prince Sattam bin Abdulaziz University in Saudi Arabia, for providing me with the invaluable opportunity to pursue a Ph.D. Program in the United Kingdom. Their support has been instrumental in making my academic journey possible.

I wish to extend my heartfelt appreciation and gratitude to my mother, brothers, and sisters, who supported me in pursuing my dream. I thank my beloved father, who instilled in me the love of achieving dreams despite his death. Also, I am grateful to my children (Hissah ‘Nada’, Salman and Danah). My gratitude to them is beyond words. I am profoundly grateful to my brother Ghazi, and my sister Malak, for their unwavering care and support. Their kindness and constant help have been a blessing, and I feel incredibly fortunate to have them by my side. Thank you, Ghazi and Malak, for everything you do and always being there for me.

Finally, I extend my warmest thanks to my dear friends Bashayr Alanazi, Sarah Alsubaie, and Hajar Algamdi, as well as my wonderful neighbors Hadeel Taleb and Kawthar Alfurqani. Your love, support, and constant encouragement have meant the world to me throughout this journey. I am deeply grateful to each of you and all you've done to uplift me.

Abstract

Studying electron transport properties in molecular junctions, comprising a molecule as the scattering region coupled to metallic electrodes is critical for nano- and molecular-scale applications. This thesis focuses on the thermoelectric properties of a specific type of two-terminal molecular junction involving gold electrodes, forming gold-molecule-gold structures. The investigation into these molecular junctions' electrical and thermoelectric behaviour relies on theoretical approaches detailed in Chapters 2 and 3. Chapter 2 introduces the principles of density functional theory DFT, while Chapter 3 provides an overview of transport theory, emphasizing Green's function formalism. Chapter 4 examines the electron transport properties of cross-linked molecular junctions, consisting of a dimer formed by two OPE3 molecules connected through two different bridges. These junctions feature six connection points with thiol groups (*SH*). To validate the findings, three theoretical approaches are employed: the orbital product rule OPR, the tight-binding model TBM, and density functional theory DFT calculations. Additionally, these cross-linked systems' electrical conductance and Seebeck coefficient are analysed using DFT simulations. Chapter 5 explores the impact of the bridge type on electron transport properties by studying another two different bridge configurations in the junctions. Finally, this thesis is concluded with a summary and future works in chapter 6.

List of publications

1- Bashayr Alanazi, Asma Alajmi, Alaa Aljobory, Colin J. Lambert, and Ali Ismael, Tuning quantum interference through molecular junctions formed from cross-linked OPE-3 dimers. *Journal of Materials Chemistry* C, 2024. **12**(19): p. 6905-6910.

2- Xintai Wang, Asma Alajmi, Zhangchenyu Wei, Mohammed Alzanbaqi, Naixu Wei, Colin Lambert, and Ali Ismael, Enhancing the Pressure-Sensitive Electrical Conductance of Self-Assembled Monolayers. *ACS Applied Materials & Interfaces*, 2024. ***16*** (48): 66290-66300.

Table of Contents

List of abbreviations

ME	Molecular electronics
STM	Scanning Tunnelling Microscopy
DFT	Density Functional Theory
TBM	Tight-Binding Models
SIESTA	Spanish Initiative for Electronic Simulations with Thousands of Atoms
CQI	Constructive Quantum Interference
DQI	Destructive Quantum Interference
C-L	Cross-linked
MD	Molecular Dynamics
LDA	Local Density Approximation
GGA	Generalized Gradient Approximation
LCAOs	Linear Combination of Atomic Orbitals
BSSE	Basis set superposition error
SCF	Self-Consistent Field
CP	Counterpoise correction
T(E)	Transmission coefficient
S (E)	Seebeck coefficient
HOMO	Highest Occupied Molecular Orbital
LUMO	Lowest Occupied Molecular Orbital
SAMs	Self-Assembled Monolayers
OPE	Oligo Phenylene-Ethylene
OPR	Orbital Product Rule
MOs	Molecular Orbitals

QI	Quantum interference

Chapter 1

Molecular electronics

1.1 Molecular electronics and thermopower

Moore’s Law has stimulated thousands of studies to reduce the size of electrical components since 1965. Over the years, electronic components, notably transistors, have progressively reduced in size, nearing the nano or molecular scale. To continue this trend, molecular electronics (ME) has developed as a scientific field that explores the electronic and thermal transport characteristics of circuits built with individual molecules or assemblies as the foundational units [1-3]. This involves utilising either individual molecules or combinations of molecules as the fundamental units for creating electrical components or devices [4]. These devices involve a range of functionalities, including transistors [5], sensors [6, 7], memories [8], current rectifiers [9], and photovoltaics [10]. The idea of driving single-molecule electronics involves crafting and engineering molecules to form complex structures, functional components, and interconnecting pathways. With its potential for sub-10nm electronic switches and rectifiers, as well as its ability to provide sensitive platforms for detecting single molecules, molecular electronics holds significant promise in the field of nanoscale electronics [11]. Additionally, there is interest in exploring the capability of these systems to investigate quantum properties at the molecular level, particularly at room temperature, involving phenomena such as quantum interference [12] and thermoelectric effects [13, 14].

1.2 History of molecular electronics

In 1974, Aviram and Ratner proposed a downsizing of electronic components by upholding the replacement of silicon chips with molecules [15]. Their proposal laid the groundwork for the evolution of molecular electronics. Subsequently, collaborative efforts from experts across various disciplines, integrating both experimental and theoretical approaches, have significantly broadened the scope of this field. A notable advancement has been creating computational and modelling tools capable of producing theoretical outcomes closely aligned with experimental observations. Recent experimental methods, like scanning tunnelling microscopy (STM) and break junctions, have further enhanced our capabilities in this area [16, 17]. Advancements in nanofabrication techniques and the refinement of quantum theories related to electronic transport over the past few decades have enabled researchers to explore and comprehend the fundamental characteristics of electrical circuits employing molecules as crucial building blocks. These studies have revealed how a range of molecular features affect electron transport, including molecular conformation [18], heteroatom substitution [19], Fermi energy tuning [20] and molecular orientation [21, 22].

Developing single-molecule devices is a complex task due to various difficulties and constraints. The challenges faced by single-molecule electrical systems can be summarised as follows:

- The small size of molecules makes it challenging to maneuver them into nanogaps directly. Instead, molecular interaction with the electrode is necessary to position the molecule within the gap.

- Ensuring that only one molecule is inserted into each functional device becomes more complex, especially when electrodes are considerably more significant than the molecules.

- Additionally, stability, uniformity, and scalability challenges further complicate the development process.

One of the essential challenges in molecular electronics is creating device platforms and understanding the mechanisms controlling molecular charge transport within them [23-25]. The most common platform involves molecules between two electrodes, serving as the quintessential molecular electronics device and a widely adopted method for examining molecular characteristics [23, 26, 27]. Theoretical approaches have progressed alongside experimental frameworks [28]. With advances in calculating molecular electrical properties, researchers can now handle more intricate molecules and achieve closer alignment between their calculations and real-world observations. Density functional theory DFT has become highly trusted and extensively utilised in theoretical research to analyse atomic structure's electronic configuration and predict charge flow in complex systems.

Additionally, tight-binding models TBMs offer a straightforward approach to simulating quantum transport in smaller systems [29-31]. These models simplify the understanding of the fundamental properties of molecules and examine their potential as active components in nano applications. By integrating DFT, utilised in the SIESTA code [32], and TBMs, alongside a Green's function formalism for electron transport found in the Gollum code, researchers have been able to elucidate fundamental principles in quantum transport theory necessary for describing essential characteristics of molecular junctions at the nanoscale. In contrast with the model of incoherent transport used by Aviram and Ratner [33], one of the surprising discoveries during the past decade was that transport through molecules can be phase coherent, even at room temperature, so that electron transport can be controlled by a range of room-temperature interference properties [34]. The theory used to describe these interference effects is based on theories derived in the 1990s to describe interference effects are mesoscopic superconductors[35-37], which occur at much lower temperatures. These techniques have been used to describe a range of interference effects, including conductance oscillations in atomic chains [38] and carbon nanotubes [39, 40], Seebeck oscillations thermoelectric voltage periodic oscillations in the stacked molecular junctions [41] and electron transport through molecular-scale junctions formed from graphene electrodes [42-44]. Recently, such studies have been extended towards new designs for nanotube-based sensors [45-47].

This thesis investigates the use of cross-linking to improve the on-off ratio in molecular junctions. It focuses on applying renormalization principles to enhance the electrical conductivity of individual molecules.

1.3 Molecular junctions

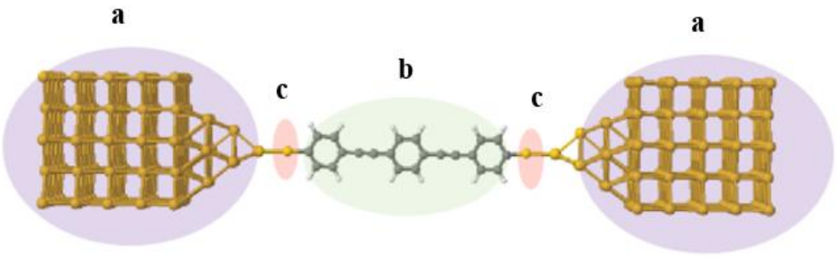

Figure 1. 1: Schematic representing a molecular junction comprising (a) left and right electrodes, (b) core molecule, and (c) linker. In this example, the electrodes are gold; the central molecule is oligo (Phenylene-ethylene) (OPE), and methyl sulfur is employed as the anchor group.

The term "molecular junction" refers to the configuration where a molecule is positioned between two metal electrodes, forming an extended metal-molecule-metal system. This structure includes left and right electrodes, linkers or anchor groups, and the central molecule, as shown in **Figure 1. 1**. One of the key factors in creating functional contact between the molecules and the electrodes is the selection of the electrode material. As noted above, graphene, a non-metallic material, is a promising candidate for electrodes in molecular junctions and has been widely studied in organic electronics [42-44, 48].

The most commonly used electrode material in junctions is gold (Au), because it is the highest conductor of electricity among metals and is chemically stable. This ensures effective charge transfer across the junction, minimising energy loss and boosting the performance of electronic devices. Moreover, gold has well-established methods for self-assembling with molecules[49, 50], making it highly suitable for such applications. On account of these beneficial properties, gold (Au) has been selected as the electrode material in this study and for this purpose, a range of anchor groups have been developed. An anchor group is a functional group that links an organic molecule to a metal surface, facilitating strong and stable binding between the two. It works to stabilise the junction and efficient electronic communication between organic molecules. The anchor atoms play a role in mediating electron transport between the organic molecule and the metal electrode. The most common anchor groups for binding to gold are amines (-NH_2), thioacetate (*SAc*) (–$SCOCH_3$), methylation (*SMe*) (–SCH_3), and thiols (-*SH*). In this thesis I use a thiol as the anchor group [51-54].

In what follows, I will explore the molecular designs to increase the on/off conductance ratio of molecular switches and improve the thermoelectric performance of molecular-scale materials at room temperature, building upon recent progress in this direction [55-65]. For example is has been shown that where one anchor group binds much more strongly to the electrodes than the other, the thermoelectric behaviour of the molecular junction is primarily influenced by the more substantial anchor group [60]. Similarly, destructive quantum interference DQI is known to significantly suppress charge transport and lowers conductance in meta-connected molecules.

Interestingly, adding a bridging carbonyl group nearly eliminates DQI, creating a cross-conjugated fluorenone with enhanced conductance. This behaviour contrasts with other π-systems, like *para*-connected anthraquinone, where cross-conjugation still leads to low conductance [61]. This effect was also highlighted in research by Alaa A. Al-Jobory and Ali K. Ismael, which revealed that substituting a conjugated bridging atom with a non-conjugated one switches the conductance from constructive CQI to destructive quantum interference DQI, effectively toggling the on/off state. This switching behaviour suggests that molecules with alternating conjugated and non-conjugated structures could enhance thermo-voltage in nanoscale thermoelectric devices when deposited on a metal surface [62]. Numerous studies have demonstrated that the electron pathway gives rise to two types of quantum interference: constructive quantum interference CQI and destructive quantum interference DQI [63-66]. This phenomenon forms the central focus of this thesis.

1.4 Thesis Outline

This thesis will provide theoretical simulations focusing on nanoscale electron transport and molecular electronics. Chapter 2 displays a brief survey of density functional theory DFT, a fundamental theoretical method used in this research to explore and comprehend the electronic characteristics of single-molecule junctions. Chapter 3 provides information related to single-particle transport theory, discussing the Landauer formula, Green's functions applicable to different transport scenarios derived from scattering theory, and examples illustrating the computation of transmission coefficients for various systems utilising the Hamiltonian and Green's functions. Following establishing the using of nanoscale transport modelling techniques, I will examine theoretical investigations of specific molecular junctions. This work dedicates two chapters to exploring the electrical and thermal characteristics of the molecules under study. Chapter 4 analyses the transport properties within cross-linked **1** (C-L**1**) OPE3 dimer analysis and cross-linked **2** (C-L**2**). In contrast, Chapter 5 investigates the transport properties within another OPE3 dimer with different bridges, cross-linked **3** (C-L**3**) junctions and cross-linked **4** (C-L**4**). Chapter 6 will provide conclusions drawn from the study and offer recommendations for future research endeavours.

1.5 Bibliography

[1] R. Reichardt, Moore's Law and the Pace of Change, Internet Reference Services Quarterly, 11 (2006) 117-124.

[2] J.C. Love, L.A. Estroff, J.K. Kriebel, R.G. Nuzzo, G.M. Whitesides, Self-Assembled Monolayers of Thiolates on Metals as a Form of Nanotechnology, Chemical Reviews, 105 (2005) 1103-1170.

[3] Y. Li, J.A. Mol, S.C. Benjamin, G.A.D. Briggs, Interference-based molecular transistors, Scientific Reports, 6 (2016) 33686.

[4] L.A. Wilkinson, T.L. Bennett, I.M. Grace, J. Hamill, X. Wang, S. Au-Yong, A. Ismael, S.P. Jarvis, S. Hou, T. Albrecht, Assembly, structure and thermoelectric properties of 1, 1′-dialkynylferrocene ‘hinges’, Chemical Science, 13 (2022) 8380-8387.

[5] J. Nossa, M.F. Islam, C.M. Canali, M. Pederson, Electric control of a {Fe 4} single-molecule magnet in a single-electron transistor, Physical Review B, 88 (2013) 224423.

[6] H. Sadeghi, L. Algaragholy, T. Pope, S. Bailey, D. Visontai, D. Manrique, J. Ferrer, V. Garcia-Suarez, S. Sangtarash, C.J. Lambert, Graphene sculpturene nanopores for DNA nucleobase sensing, The Journal of Physical Chemistry B, 118 (2014) 6908-6914.

[7] H. Sadeghi, S. Bailey, C.J. Lambert, Silicene-based DNA nucleobase sensing, Applied Physics Letters, 104 (2014).

[8] K.J. Yoon, M.H. Lee, G.H. Kim, S.J. Song, J.Y. Seok, S. Han, J.H. Yoon, K.M. Kim, C.S. Hwang, Memristive tri-stable resistive switching at ruptured conducting filaments of a Pt/TiO2/Pt cell, Nanotechnology, 23 (2012) 185202.

[9] A. Martin, J. Sambles, G. Ashwell, Molecular rectifier, Physical review letters, 70 (1993) 218.

[10] A. Kolmakov, M. Moskovits, Chemical sensing and catalysis by one-dimensional metal-oxide nanostructures, Annu. Rev. Mater. Res., 34 (2004) 151-180.

[11] E.H. Lieb, B. Simon, The Thomas-Fermi theory of atoms, molecules and solids, Advances in mathematics, 23 (1977) 22-116.

[12] L. Yang, Y. Zhang, W. Cai, J. Tan, H. Hansen, H. Wang, Y. Chen, M. Zhu, J. Mu, Electrochemically-driven actuators: from materials to mechanisms and from performance to applications, Chemical Society Reviews, (2024).

[13] H. Sadeghi, S. Sangtarash, C.J. Lambert, Enhanced thermoelectric efficiency of porous silicene nanoribbons, Scientific reports, 5 (2015) 9514.

[14] H. Sadeghi, S. Sangtarash, C.J. Lambert, Oligoyne molecular junctions for efficient room temperature thermoelectric power generation, Nano letters, 15 (2015) 7467-7472.

[15] E. Scheer, Visions for a molecular future, (2013).

[16] M.G. Moula, S. Suzuki, W.J. Chun, S. Otani, S.T. Oyama, K. Asakura, Surface structures of Ni2P (0001)—scanning tunneling microscopy (STM) and low‐energy electron diffraction (LEED) characterizations, Surface and Interface Analysis: An International Journal devoted to the development and application of techniques for the analysis of surfaces, interfaces and thin films, 38 (2006) 1611-1614.

[17] D.J. Wold, C.D. Frisbie, Formation of metal− molecule− metal tunnel junctions: microcontacts to alkanethiol monolayers with a conducting AFM tip, Journal of the American Chemical Society, 122 (2000) 2970-2971.

[18] C.M. Finch, S. Sirichantaropass, S.W. Bailey, I.M. Grace, V.M. Garcia-Suarez, C.J. Lambert, Conformation dependence of molecular conductance: chemistry versus geometry, Journal of Physics: Condensed Matter, 20 (2007) 022203.

[19] Y. Yang, M. Gantenbein, A. Alqorashi, J. Wei, S. Sangtarash, D. Hu, H. Sadeghi, R. Zhang, J. Pi, L. Chen, Heteroatom-induced molecular asymmetry tunes quantum interference in charge transport through single-molecule junctions, The Journal of Physical Chemistry C, 122 (2018) 14965-14970.

[20] X. Wang, A. Ismael, S. Ning, H. Althobaiti, A. Al-Jobory, J. Girovsky, H.P. Astier, L.J. O'Driscoll, M.R. Bryce, C.J. Lambert, Electrostatic Fermi level tuning in large-scale self-assembled monolayers of oligo (phenylene–ethynylene) derivatives, Nanoscale Horizons, 7 (2022) 1201-1209.

[21] S. Afsari, Z. Li, E. Borguet, Orientation‐Controlled Single‐Molecule Junctions, Angewandte Chemie International Edition, 53 (2014) 9771-9774.

[22] T. Alotaibi, M. Alshahrani, M. Alshammari, M. Alotaibi, T.A.M. Taha, A.A. Al-Jobory, A. Ismael, Orientational Effects and Molecular-Scale Thermoelectricity Control, ACS omega, 9 (2024) 29537-29543.

[23] J.L. Zhang, J.Q. Zhong, J.D. Lin, W.P. Hu, K. Wu, G.Q. Xu, A.T. Wee, W. Chen, Towards single molecule switches, Chemical Society Reviews, 44 (2015) 2998-3022.

[24] J.R. Heath, Molecular electronics, Annual Review of Materials Research, 39 (2009) 1-23.

[25] F.J. Giessibl, Advances in atomic force microscopy, Reviews of modern physics, 75 (2003) 949.

[26] H. Li, M.H. Garner, Z. Shangguan, Y. Chen, Q. Zheng, T.A. Su, M. Neupane, T. Liu, M.L. Steigerwald, F. Ng, Large variations in the single-molecule conductance of cyclic and bicyclic silanes, Journal of the American Chemical Society, 140 (2018) 15080-15088.

[27] S. Bock, O.A. Al-Owaedi, S.G. Eaves, D.C. Milan, M. Lemmer, B.W. Skelton, H.M. Osorio, R.J. Nichols, S.J. Higgins, P. Cea, Single-Molecule Conductance Studies of Organometallic Complexes Bearing 3-Thienyl Contacting Groups, Chemistry–A European Journal, 23 (2017) 2133-2143.

[28] Y. Xue, M.A. Ratner, Theoretical principles of single-molecule electronics: a chemical and mesoscopic view, International journal of quantum chemistry, 102 (2005) 911-924.

[29] C.J. Lambert, Quantum transport in nanostructures and molecules: an introduction to molecular electronics, IoP Publishing, 2021.

[30] H. Sadeghi, Theory of electron and phonon transport in nano and molecular quantum devices: design strategies for molecular electronics and thermoelectricity, Lancaster University (United Kingdom), 2016.

[31] M. Thoss, F. Evers, Perspective: Theory of quantum transport in molecular junctions, The Journal of chemical physics, 148 (2018).

[32] E. Artacho, E. Anglada, O. Diéguez, J.D. Gale, A. García, J. Junquera, R.M. Martin, P. Ordejón, J.M. Pruneda, D. Sánchez-Portal, The SIESTA method; developments and applicability, Journal of Physics: Condensed Matter, 20 (2008) 064208.

[33] A. Aviram, M.A. Ratner, Molecular rectifiers, Chemical physics letters, 29 (1974) 277-283.

[34] C. Lambert, Basic concepts of quantum interference and electron transport in single-molecule electronics, Chemical Society Reviews, 44 (2015) 875-888.

[35] N. Claughton, M. Leadbeater, C. Lambert, Theory of Andreev resonances in quantum dots, Journal of Physics: Condensed Matter, 7 (1995) 8757.

[36] C. Lambert, Quantum interference from superconducting islands in a mesoscopic solid, Journal of Physics: Condensed Matter, 5 (1993) 707.

[37] C. Lambert, R. Raimondi, V. Sweeney, A. Volkov, Boundary conditions for quasiclassical equations in the theory of superconductivity, Physical Review B, 55 (1997) 6015.

[38] V. García-Suárez, A.R. Rocha, S. Bailey, C. Lambert, S. Sanvito, J. Ferrer, Conductance oscillations in zigzag platinum chains, Physical review letters, 95 (2005) 256804.

[39] I. Grace, S. Bailey, C. Lambert, Electron transport in carbon nanotube shuttles and telescopes, Physical Review B—Condensed Matter and Materials Physics, 70 (2004) 153405.

[40] V.M. García-Suárez, J. Ferrer, C.J. Lambert, Tuning the electrical conductivity of nanotube-encapsulated metallocene wires, Physical review letters, 96 (2006) 106804.

[41] M.K. Al-Khaykanee, A.K. Ismael, I. Grace, C.J. Lambert, Oscillating Seebeck coefficients in π-stacked molecular junctions, RSC advances, 8 (2018) 24711-24715.

[42] M. El Abbassi, S. Sangtarash, X. Liu, M.L. Perrin, O. Braun, C. Lambert, H.S.J. van der Zant, S. Yitzchaik, S. Decurtins, S.-X. Liu, Robust graphene-based molecular devices, Nature nanotechnology, 14 (2019) 957-961.

[43] M. El Abbassi, M.L. Perrin, G.B. Barin, S. Sangtarash, J. Overbeck, O. Braun, C.J. Lambert, Q. Sun, T. Prechtl, A. Narita, Controlled quantum dot formation in atomically engineered graphene nanoribbon field-effect transistors, ACS nano, 14 (2020) 5754-5762.

[44] X. Zheng, G.R. Zhang, Z. Zeng, V.M. García-Suárez, C.J. Lambert, Effects of antidots on the transport properties of graphene nanoribbons, Physical Review B—Condensed Matter and Materials Physics, 80 (2009) 075413.

[45] L.A. Algharagholy, V.M. García-Suárez, H.A. Dhahi, Stable and robust discriminative sensing of illicit drug molecules utilizing a specific geometry of nanotubes, Nano-Structures & Nano-Objects, 39 (2024) 101281.

[46] L.A. Algharagholy, V.M. García-Suárez, S.S. Abaas, Selective Sensing of DNA Nucleobases with Angular Discrimination, ACS omega, 9 (2024) 3240-3249.

[47] L.A. Algharagholy, V.M. García-Suárez, K.H. Bardan, Robust nanotube-based nanosensor designed for the detection of explosive molecules, Nanoscale Advances, 6 (2024) 3553-3565.

[48] Z. Chen, I.M. Grace, S.L. Woltering, L. Chen, A. Gee, J. Baugh, G.A.D. Briggs, L. Bogani, J.A. Mol, C.J. Lambert, Quantum interference enhances the performance of single-molecule transistors, Nature Nanotechnology, (2024) 1-7.

[49] M. Famili, C. Jia, X. Liu, P. Wang, I.M. Grace, J. Guo, Y. Liu, Z. Feng, Y. Wang, Z. Zhao, Self-assembled molecular-electronic films controlled by room temperature quantum interference, Chem, 5 (2019) 474-484.

[50] X. Wang, T.L. Bennett, A. Ismael, L.A. Wilkinson, J. Hamill, A.J. White, I.M. Grace, O.V. Kolosov, T. Albrecht, B.J. Robinson, Scale-up of room-temperature constructive quantum interference from single molecules to self-assembled molecular-electronic films, Journal of the American Chemical Society, 142 (2020) 8555-8560.

[51] M. Frei, S.V. Aradhya, M.S. Hybertsen, L. Venkataraman, Linker dependent bond rupture force measurements in single-molecule junctions, Journal of the American Chemical Society, 134 (2012) 4003-4006.

[52] Y.S. Park, A.C. Whalley, M. Kamenetska, M.L. Steigerwald, M.S. Hybertsen, C. Nuckolls, L. Venkataraman, Contact chemistry and single-molecule conductance: a comparison of phosphines, methyl sulfides, and amines, Journal of the American Chemical Society, 129 (2007) 15768-15769.

[53] M. Kamenetska, S.Y. Quek, A. Whalley, M. Steigerwald, H. Choi, S.G. Louie, C. Nuckolls, M. Hybertsen, J. Neaton, L. Venkataraman, Conductance and geometry of pyridine-linked single-molecule junctions, Journal of the American Chemical Society, 132 (2010) 6817-6821.

[54] W. Haiss, C. Wang, R. Jitchati, I. Grace, S. Martín, A.S. Batsanov, S.J. Higgins, M.R. Bryce, C.J. Lambert, P.S. Jensen, Variable contact gap single-molecule conductance determination for a series of conjugated molecular bridges, Journal of Physics: Condensed Matter, 20 (2008) 374119.

[55] S.-X. Liu, A.K. Ismael, A. Al-Jobory, C.J. Lambert, Signatures of Room-Temperature Quantum Interference in Molecular Junctions, Accounts of Chemical Research, 56 (2023) 322-331.

[56] P. Bastante, R.J. Davidson, W. Al Malki, R.J. Salthouse, P. Cea, S. Martin, A.S. Batsanov, C.J. Lambert, M.R. Bryce, N. Agrait, The Conductance and Thermopower Behavior of Pendent Trans-Coordinated Palladium(II) Complexes in Single-Molecule Junctions, ACS Omega, 9 (2024) 38303-38312.

[57] M. Roemer, A. Gillespie, D. Jago, D. Costa-Milan, J. Alqahtani, J. Hurtado-Gallego, H. Sadeghi, C.J. Lambert, P.R. Spackman, A.N. Sobolev, B.W. Skelton, A. Grosjean, M. Walkey, S. Kampmann, A. Vezzoli, P.V. Simpson, M. Massi, I. Planje, G. Rubio-Bollinger, N. Agraït, S.J. Higgins, S. Sangtarash, M.J. Piggott, R.J. Nichols, G.A. Koutsantonis, 2,7- and 4,9-Dialkynyldihydropyrene Molecular Switches: Syntheses, Properties, and Charge Transport in Single-Molecule Junctions, J Am Chem Soc, 144 (2022) 12698-12714.

[58] A.K. Ismael, C.J. Lambert, Molecular-scale thermoelectricity: a worst-case scenario, Nanoscale Horizons, 5 (2020) 1073-1080.

[59] Q. Wu, S. Hou, H. Sadeghi, C.J. Lambert, A single-molecule porphyrin-based switch for graphene nano-gaps, Nanoscale, 10 (2018) 6524-6530.

[60] J.M. Hamill, A. Ismael, A. Al-Jobory, T.L. Bennett, M. Alshahrani, X. Wang, M. Akers-Douglas, L.A. Wilkinson, B.J. Robinson, N.J. Long, Quantum Interference and Contact Effects in the Thermoelectric Performance of Anthracene-Based Molecules, The Journal of Physical Chemistry C, 127 (2023) 7484-7491.

[61] A. Alanazy, E. Leary, T. Kobatake, S. Sangtarash, M.T. González, H.-W. Jiang, G.R. Bollinger, N. Agräit, H. Sadeghi, I. Grace, Cross-conjugation increases the conductance of meta-connected fluorenones, Nanoscale, 11 (2019) 13720-13724.

[62] A.A. Al-Jobory, A.K. Ismael, Controlling quantum interference in tetraphenyl-aza-BODIPYs, Current Applied Physics, 54 (2023) 1-4.

[63] A. Almeshal, A.A. Al-Jobory, Z.Y. Mijbil, Precise control of single-phenanthrene junction’s conductance, Journal of Computational Electronics, 21 (2022) 71-79.

[64] N.R. Rajamohan, S.R. Ramanathan, S.R. Francis, Resolving set for line graph of linear benzene and polyphenyl structures, in: AIP Conference Proceedings, AIP Publishing, 2024.

[65] I.M. Grace, G. Olsen, J. Hurtado-Gallego, L. Rincón-García, G. Rubio-Bollinger, M.R. Bryce, N. Agraït, C.J. Lambert, Connectivity dependent thermopower of bridged biphenyl molecules in single-molecule junctions, Nanoscale, 12 (2020) 14682-14688.

[66] Z.-Y. Cai, Z.-W. Ma, H. Jin, J.-Z. Wang, L.-K. Chen, T.-R. Wu, Z. Sajid, J.-Z. Zhou, D.-Y. Wu, Z.-Q. Tian, Bias switching in single-molecule junctions through destructive quantum interference, Electrochimica Acta, 507 (2024) 145136.

Chapter2

Density functional theory (DFT)

This chapter provides a concise overview of density functional theory DFT and its application through the SIESTA (Spanish initiative for electronic simulations with thousands of atoms) code. It outlines fundamental concepts and practical uses of SIESTA in analysing electronic structure properties across various systems. This theoretical approach serves as the primary method in our research, enabling the examination of isolated molecule Hamiltonians, wave functions, geometry optimisation, bond energies, and electron transport phenomena in nanoscale structures or single molecules linked to electrodes. To gain structural and electronic insights, I will extract the Hamiltonian from DFT calculations for the target system and utilise it to explore molecular junction transport properties, a topic delved into further in Chapter 3.

2.1 Introduction

Theoretical condensed matter physics aims to uncover the electronic behaviour of materials by studying how electrons interact with nuclei. This discipline is handling the difficulties affected by intricate interactions and computational challenges. Over the past five decades, approaches like molecular dynamics MD, density functional theory DFT, and tight binding theory TB have been developed, each offering different balances of accuracy and computational efficiency [1, 2]. Understanding electron behaviour in molecular wires provides insight into their electrical characteristics, serving as a key example in molecular electronics. DFT is an effective method for understanding structural and electronic properties, especially for nanoscale simulations [3]. Also, DFT is a powerful tool for predicting electronic configurations in atoms, molecules, and crystals, with broad applications in physics, chemistry, and materials science. Its methodology centres on electron density functionals, tracing its origins to the work of Thomas and Fermi in the 1920s, who linked total energy to density-derived functionals [3, 4].

Modern DFT is grounded in the Hohenberg-Kohn theorems (1964) and the Kohn-Sham method [4], which efficiently calculates the ground state energy of many-particle systems. Then, it explores the Born-Oppenheimer approximation concerning nuclei, followed by the Hohenberg-Kohn theorem, and further extends to the influential Kohn-Sham theorem, notable for its effectiveness in describing the ground state properties of quantum systems. These principles underlie tools like the SIESTA code, which I used extensively during my PhD research [5]. DFT allowed me to investigate molecular architectures, charge densities, and band structures both qualitatively and quantitatively, providing key insights into electronic properties.

2.2 The Schrödinger equation and variational principle

The Schrödinger equation used to describe non-relativistic multi-particle system by using the time-independent, non-relativistic Schrödinger equation, as stated in equation (2.1)

$$H\,\psi_i\left(\vec{r}_1, \vec{r}_2, \dots, \vec{r}_N, \vec{R}_1, \vec{R}_2, \dots\dots, \vec{R}_M\right) = E_i\psi_i\left(\vec{r}_1, \vec{r}_2, \dots, \vec{r}_N, \vec{R}_1, \vec{R}_2, \dots\dots, \vec{R}_M\right) \qquad (2.1)$$

Where ψ_i is the wave function of the state of the system, and E_i is the numerical value of the energy of the i$^{\text{th}}$ represented by ψ_i. H represents the Hamiltonian operator of a system consisting of N-electrons and M-nuclei that contain the interaction of particles with each other.

The position of the electrons and nuclei are denoted as $\vec{r}_i$ and $\vec{R}_n$respectively, and ∇^2 is the Laplacian operator, in Cartesian coordinates, is defined as,

$$\nabla^2 = \frac{\partial^2}{\partial x_i^2} + \frac{\partial^2}{\partial y_i^2} + \frac{\partial^2}{\partial z_i^2} \qquad (2.2)$$

However, solving the Schrödinger equation for many-body systems with many electrons is computationally challenging. To tackle this issue, various approximations, such as those introduced by Max Born and J. Robert Oppenheimer in 1927, are employed [6, 7].

2.3 Born- Oppenheimer approximation

The Born-Oppenheimer approximation is a method commonly used to simplify the Schrödinger equation (2.1), which becomes intractable for systems with more than a few electrons. Since the nuclei are much heavier than electrons, their motion is significantly slower, allowing us to neglect their kinetic energy and treat them as classical particles with fixed external potentials. Consequently, we consider the electrons as quantum particles influenced by this potential, if the nuclear wave function does not depend on electron positions [8-10]. We derive the electron behaviour from solving the Schrödinger equation under these conditions. Thus, the Hamiltonian for electrons can be expressed as:

$$H = T_e + V_e + \sum_i V_{ext}(r_i) \qquad (2.3)$$

Where $T_e = -\frac{\hbar^2}{2m_e}\sum_i \nabla_i^2$,which is the kinetic energy of all electrons, $V_e = \frac{1}{8\pi\varepsilon_o}\sum_{i\neq j}\frac{e^2}{|r_i - r_j|}$ which represents the interaction between electrons, and $\mathrm{V_{ext}}$ is the external potential arising from the interaction between nuclei and electrons, along with any additional external fields.

Then the Schrödinger equation can be written as:

$$H\,\psi_i(\vec{r}_1, \vec{r}_2, \dots, \vec{r}_i \dots) = E_i \psi_i(\vec{r}_1, \vec{r}_2, \dots, \vec{r}_i \dots) \qquad (2.4)$$

Despite the simplification achieved by this approximation, solving the Schrödinger equation remains challenging. DFT offers a solution by expressing physical properties in relation to the ground-state electron density, $\rho_o(\vec{r})$. The initial method to tackle this is the Hohenberg-Kohn theorem [11].

2.4 Density functional theory

Density functional theory DFT is an essential theoretical description of nanoscale simulations of electronic structure properties of atoms and molecules. It is a first-principles technique to predict a material's properties with as few approximations as appropriate. It can be applied to find highly accurate results on smaller systems [12].

The Hohenberg-Kohn theorem, established in 1964, is a fundamental principle within DFT because its ability to characterise properties of the ground-state of interacting electrons is a unique function of the electronic electron density $\rho(\vec{r})$ system [13]. In 1965 the Kohn and Sham method stand out as the most effective approach for investigating DFT [14]. It is a method to provide information related to the ground state with interacting particles to a non-interacting particle system through their charge density. These methods are described in the following two sections.

2.4.1 The Hohenberg- Kohn theorems

The Hohenberg-Kohn theorem HK is the cornerstone of DFT [13]. It applies to many-electron systems interacting with an external potential $V(r)$, defining a functional that minimises the total energy with the electron density as the ground state. The HK theorem validation is most effectively demonstrated through two compelling propositions.

1- In any interacting system subjected to an external potential $V_{ext}(\vec{\mathrm{r}})$, this potential is uniquely dictated given that $V_{ext}(\vec{\mathrm{r}})$ fixes the system's Hamiltonian, H, by the ground-state density ρ_r [13, 15].

2-The total energy of the system E_{HK} is minimised to attain the accurate ground-state energy, dependent on the electron density in its ground state ρ_r. Assume that the two external potentials provide the same ground-state density ρ_r. In essence, DFT offers a way to address quantum many-body problems by concentrating on the electron density ρ_r instead of dealing directly with the complex many-body wavefunction. These potentials correspond to two separate Hamiltonians designated by $\hat{H}_1$ and $\hat{H}_2$ and the ground-state wavefunctions, ψ_1 and ψ_2. Therefore, we have

$$\hat{H}_1\,\psi_1 = E_1\,\psi_1$$

$$\hat{H}_2\,\psi_2 = E_2\,\psi_2$$

Where ψ_2 is not the ground state wavefunction of $\hat{H}_1$

$$E_1 = \langle\psi_1|\hat{H}_1|\psi_1\rangle < \langle\psi_2|\hat{H}_1|\psi_2\rangle \tag{2.5}$$

and similarly:

$$E_2 = \langle\psi_2|\hat{H}_2|\psi_2\rangle < \langle\psi_1|\hat{H}_2|\psi_1\rangle \tag{2.6}$$

Assuming non-degenerate ground states, we can rewrite the equation (2.6)

$$\langle\psi_2|\hat{H}_1|\psi_2\rangle = \langle\psi_2|\hat{H}_2|\psi_2\rangle + \langle\psi_2|\hat{H}_1 - \hat{H}_2|\psi_2\rangle$$

$$= E_2 + \langle\psi_2|V_{ext(1)}(\vec{r}) - V_{ext(2)}(\vec{r})|\psi_2\rangle$$

$$= E_2 + \int dr\,[V_{ext(1)}(\vec{r}) - V_{ext(2)}(\vec{r})]\,\rho_o(r) \tag{2.7}$$

Additionally, assuming that $|\psi_1\rangle$ has the same density $\rho_o(r)$ as $|\psi_2\rangle$

$$\langle\psi_1|\hat{H}_2|\psi_1\rangle = E_1 + \int dr\,[V_{ext(2)}(\vec{r}) - V_{ext(1)}(\vec{r})]\,\rho_o(r) \tag{2.8}$$

Adding together the two equations (2.7) and (2.8) guide to a contradiction

$$E_1 + E_2 < E_1 + E_2 \tag{2.9}$$

Thus, it follows that the two differing external potentials cannot yield the same ground state density.

The second theorem is proved by minimisation of the ground state functional, which can be written as

$$E[\rho] = T[\rho] + E_{int}[\rho] + \int dr\,V_{ext}\,(r)\,\rho(r) \tag{2.10}$$

The kinetic term (T) and the internal electron-electron interaction (E_{int}) is the universal energy of the electron density.

2.4.2 The Kohn-Sham theorem

By acquiring the ground-state density, we can calculate the ground-state energy, and it is theoretically possible to compute the ground-state energy by from the ground-state density [16]. However, the kinetic energy term and the internal energy of the particles interacting with each other, as represented in equation (2.10), remain elusive and typically cannot be represented simply as a density function. Kohn and Sham investigated a solution method that achieves consistency by producing identical ground-state densities for any given system of interacting particles [17]. According to Kohn and Sham, the original Hamiltonian can be replaced with an effective Hamiltonian of non-interacting particles with a real external potential having the same ground-state density as the original system [18, 19].

The form of the energy functional of the Kohn-Sham is:

$$E_{KS}\ (\rho) = T_{KS}\,(\rho) + \int dr\, V_{ext}\,(r)\,\rho(r) + E_H\,(\rho) + E_{xc}\,(\rho) \qquad (2.11)$$

Here, $(T_{ks}\,)$ is the kinetic energy of the non-interacting system, while (T) in equation (2.10) is

the kinetic energy for the interacting system (E_H) represents the classical electrostatic

energy (Hartree energy), which describes the electron-electron interaction of the classical charge distribution, which has the following form using the Hartree-Fock method:

$$E_H\,[\rho(r)] = \frac{1}{2}\int \frac{\rho(r)\,\rho(\acute{r})}{|r-\acute{r}|}\,dr\,d\acute{r} \qquad (2.12)$$

Here, $(E_{xc})$is the exchange-correlation functional accounts for the disparities between the specific and approximate solutions of both the kinetic energy and electron-electron interaction term it's defined:

$$E_{xc}[\rho(r)] = (E_{int}(\rho) - E_H(\rho)) + (T(\rho) - T_{KS}(\rho)) \tag{2.13}$$

The single-particle Hamiltonian can be described using the effective potential for a single particle (V_{eff}) which is described by taking the functional derivatives of the last three terms of equation (2.11) as:

$$V_{eff}(r) = V_{ext}(r) + \frac{\partial}{\partial\rho}(E_H[\rho(r)] + E_{xc}[\rho(r)]) \tag{2.14}$$

Therefore, the Hamiltonian can be expressed as:

$$H_{KS} = T_{ks}[\rho] + V_{eff} \tag{2.15}$$

Next, the Kohn-Sham equation can be derived by utilising the single Hamiltonian, which is formulated as:

$$H_{KS}\ \psi^{KS} = E\ \psi^{KS} \tag{2.16}$$

That is, despite decades of investigation, there is no exact remedy. The next section discusses several excellent approximations that have been developed.

2.5 The exchange correlation functional

Various alterations to the exchange and correlation of energy have been documented in scientific literature. The local density approximation LDA achieved the initial effective formulation [17, 20]. The dependence simply on density characterises it as locally functional. Subsequently, the generalized gradient approximation GGA marked the subsequent advancement [21-24]. A more complex form that also includes the derivative of the semi-local density is known as the GGA [27-28].

The following sections will briefly discuss the LDA and the GGA.

2.5.1 Local density approximation

The local density approximation LDA stands as an early and basic approximation, relying on the local density. It is anticipated to yield favourable outcomes for systems exhibiting generally smooth local density distributions. Notably, it demonstrates accuracy in scenarios like graphene and carbon nanotubes, where electron density changes occur gradually. However, its efficacy is reduced in systems heavily influenced by electron-electron interactions. Despite its simplicity, LDA serves as an active function for numerous systems.

2.5.2 Generalized gradient approximation

As the electron density experiences rapid fluctuations within natural inhomogeneous systems, the LDA becomes unsuitable, particularly for heavier atoms. Therefore, there's a need to request an alternative approximation that accounts more accurately for the gradient of electron density, leading to the generalized gradient approximation GGA.

GGA extends beyond LDA by incorporating density derivatives into the functional expression of exchange and correlation energies [5, 22]. Although the GGA lacks a closed form for the exchange term of the functional, the exchange contribution, along with the correlation contribution, has been estimated using numerical methods. For the approximation of exchange-correlation energies in the DFT, LDA and GGA are two of the most widely utilised approximations. Several functionalities beyond LDA and GGA are also provided.

2.6 SIESTA

SIESTA is a computational tool rooted in density functional theory DFT. It facilitates electronic structure computations and molecular dynamics simulations for both molecules and solids [25, 26]. The DFT module within the SIESTA code, which was utilised to showcase the electronic properties of optimised structures, was employed for all computations presented in this thesis. Designed to handle efficient calculations on extensive systems comprised of thousands of atoms, it offers substantial computational capability.

2.6.1 The pseudopotential approximation

In the previous section, we discussed how the Kohn-Sham approach simplifies complex interactions among many particles into a large but non-interacting system. However, dealing with systems involving numerous atoms leads to intricate and computationally intensive calculations. To mitigate this challenge, Fermi introduced pseudopotentials in 1934 [27]. These pseudopotentials aim to reduce the number of core electrons in atoms, thereby streamlining the computational process. Over time, this method has evolved from initially creating somewhat unrealistic empirical pseudopotentials [28] these pseudopotentials have progressed to become more realistic ab-initio versions over time [29, 30]. This approximation assumes the presence of two distinct types of electrons in atoms: core electrons, staying in filled atomic shells, and valence electrons, occupying partially filled shells. When atoms come together, only valence electrons contribute to the formation of molecular orbitals. This is because core electrons are spatially localised around the nucleus, and their electronic states overlap. To simplify computations, pseudopotentials are employed by replacing the core electrons.

2.6.2 Basis sets

Basis sets are a key component utilised by SIESTA in its calculations. Diagonalising the Hamiltonian to determine wavefunctions involves handling a large matrix, and the computational time increases with the number of non-zero elements.

SIESTA employs a linear combination of atomic orbitals LCAOs basis set. These basis functions are confined to zero beyond a specified cut-off radius and are computed using the orbitals of the atoms involved. Basis sets are crucial because the Schrödinger equation cannot usually be solved exactly. They provide a practical way to approximate wavefunctions in a form that can be handled computationally [31, 32]. Consequently, as the overlap of basic functions diminishes, the Hamiltonian takes a sparse form. This allows even a minimal-sized basis set to closely approximate the properties of the systems being studied. The construction of basic functions involves utilising numerical radial and spherical harmonic components. Which is followed by:

$$\psi_{nlm}(r) = \phi_{nl}^{1}(r)\, Y_{lm}(\varphi, \vartheta) \tag{2.17}$$

In this context, $\phi_{nl}^{1}(r)$ represents the radial wavefunction and $Y_{lm}(\varphi, \vartheta)$ represents a spherical harmonic wavefunction. Here, (l) denotes the orbital angular momentum, (m) indicates the magnetic quantum number, and (n) suggests that multiple orbitals may share the same angular momentum numbers. The most basic form of an atomic basis set is the single- ζ set, where each electron orbital corresponds to one basis function. For higher accuracy, multiple- ζ sets are used, involving additional radial wavefunctions for each atomic orbital. Even greater precision is achieved with multiple- ζ polarised sets, which incorporate wavefunctions with different angular momenta corresponding to unoccupied orbitals in the atom.

2.6.3 Binding energy using the counterpoise method

As previously mentioned, the DFT approach is employed to compute the ground-state energy for various system configurations and to determine the binding energy between different components of a system. However, the accuracy of these calculations is compromised by the localised nature of the LCOA basis sets, which are centred on the nuclei. When atoms come into proximity, their basis functions overlap, leading to what is known as the basis set superposition error BSSE. This error escalates as atoms orient themselves closer together, resulting in an effectively changing basis set with varying interatomic distances [33]. If we designate two molecular systems as (A) and (B), the energy of their interaction can be formulated as:

$$\Delta E(AB) = E^{AB} - (E^{A} + E^{B}) \tag{2.18}$$

where (E^{AB}) is the total energy for the dimer systems (A) and (B), (E^{A}) and (E^{B}) are the energies of the isolated systems (A) and (B). It is important to note that in SIESTA, the counterpoise correction involves employing ghost states, which represent regions devoid of nuclei and electrons but contain empty basis set functions centred on them. These ghost states are utilised to compute the total energy of isolated systems (A) or (B) in the dimer basis, while maintaining identical basis sets for all three energy evaluations [34, 35].

$$\Delta E(AB) = E_{AB}^{AB} - (E_{A}^{AB} + E_{B}^{AB}) \qquad (2.19)$$

The notation (E_A^{AB}) and (E_B^{AB}) represent the energies of systems (A) and (B) evaluated in the basis of the dimer, where the superscript (AB) indicates the utilisation of the entire basis set, and the subscripts denote the respective geometries. This method is crucial for eliminating the basis set superposition error BSSE and ensuring the reliability and realism of results across various systems [36].

2.7 Conclusion

This chapter has illustrated the fundamental principles of density functional theory DFT, starting with the Schrödinger equation and progressing through the Hohenberg-Kohn theorems and the Kohn-Sham formalism. Furthermore, it has explored the functional expressions of exchange and correlation energies within both the local density approximation LDA and the generalized gradient approximation GGA, along with their integration into the SIESTA framework, which was introduced, along with some fine details of the calculations, such as the use of pseudopotentials and binding energy.

2.8 Bibliography

[1] G.-H. Kim, L. Shao, K. Zhang, K.P. Pipe, Engineered doping of organic semiconductors for enhanced thermoelectric efficiency, Nature materials, 12 (2013) 719-723.

[2] P.W. Atkins, R.S. Friedman, Molecular quantum mechanics, Oxford University Press, USA, 2011.

[3] N. Argaman, G. Makov, Density functional theory: An introduction, American Journal of Physics, 68 (2000) 69-79.

[4] V.S. Lisitsa, Atoms in plasmas, Springer Science & Business Media, 2012.

[5] J.M. Soler, E. Artacho, J.D. Gale, A. García, J. Junquera, P. Ordejón, D. Sánchez-Portal, The SIESTA method for ab initio order-N materials simulation, Journal of Physics: Condensed Matter, 14 (2002) 2745.

[6] G.A. Hagedorn, A time dependent Born-Oppenheimer approximation, Communications in Mathematical Physics, 77 (1980) 1-19.

[7] T.D. Lee, C.N. Yang, Many-body problem in quantum statistical mechanics. I. General formulation, Physical Review, 113 (1959) 1165.

[8] A. Komainda, B. Ostojic, H. Köppel, Ab initio quantum study of nonadiabatic S1–S2 photodynamics of s-trans-butadiene, The Journal of Physical Chemistry A, 117 (2013) 8782-8793.

[9] Y. Luo, J. Byggmästar, M.R. Daymond, L.K. Béland, Interatomic force fields for zirconium based on the embedded atom method and the tabulated Gaussian Approximation Potential, Computational Materials Science, 233 (2024) 112730.

[10] G. Kolesov, E. Kaxiras, E. Manousakis, Density functional theory beyond the Born-Oppenheimer approximation: Accurate treatment of the ionic zero-point motion, Physical Review B, 98 (2018) 195112.

[11] M. Slamet, V. Sahni, Quantal density functional theory of excited states: Application to an exactly solvable model, International Journal of Quantum Chemistry, 85 (2001) 436-448.

[12] J.F. Stanton, A Chemist's Guide to Density Functional Theory By Wolfram Koch (German Chemical Society, Frankfurt am Main) and Max C. Holthausen (Humbolt University Berlin). Wiley-VCH: Weinheim. 2000. xiv+ 294 pp. $79.95. ISBN 3-527-29918-1, in, ACS Publications, 2001.

[13] P. Hohenberg, W. Kohn, Inhomogeneous electron gas, Physical review, 136 (1964) B864.

[14] W. Kohn, L.J. Sham, Self-consistent equations including exchange and correlation effects, Physical review, 140 (1965) A1133.

[15] W. Kohn, Nobel Lecture: Electronic structure of matter—wave functions and density functionals, Reviews of Modern Physics, 71 (1999) 1253.

[16] F. Brockherde, L. Vogt, L. Li, M.E. Tuckerman, K. Burke, K.-R. Müller, Bypassing the Kohn-Sham equations with machine learning, Nature communications, 8 (2017) 872.

[17] D.M. Ceperley, B.J. Alder, Ground state of the electron gas by a stochastic method, Physical review letters, 45 (1980) 566.

[18] M. Levy, Electron densities in search of Hamiltonians, Physical Review A, 26 (1982) 1200.

[19] E.H. Lieb, Thomas-Fermi and related theories of atoms and molecules, Reviews of Modern Physics, 53 (1981) 603.

[20] D.C. Langreth, J.P. Perdew, Exchange-correlation energy of a metallic surface: Wave-vector analysis, Physical Review B, 15 (1977) 2884.

[21] M. Glasser, N. March, L. Nieto, Exchange energy density in density-functional theory via the Dirac density matrix for a nonrelativistic 10-electron atomic ion compared with Becke's proposal for a gradient-corrected local-density-approximation result, Physical Review A—Atomic, Molecular, and Optical Physics, 79 (2009) 042506.

[22] B. Hammer, L.B. Hansen, J.K. Nørskov, Improved adsorption energetics within density-functional theory using revised Perdew-Burke-Ernzerhof functionals, Physical review B, 59 (1999) 7413.

[23] J.P. Perdew, K. Burke, M. Ernzerhof, Generalized gradient approximation made simple, Physical review letters, 77 (1996) 3865.

[24] J.P. Perdew, Y. Wang, Accurate and simple analytic representation of the electron-gas correlation energy, Physical review B, 45 (1992) 13244.

[25] R.R. Wilson, The Collected Papers of Enrico Fermi, Volume 1, Italy 1921–1938, Nuclear Science and Engineering, 16 (1963) 143-144.

[26] J. Ferrer, C.J. Lambert, V.M. García-Suárez, D.Z. Manrique, D. Visontai, L. Oroszlány, R. Rodríguez-Ferradás, I. Grace, S. Bailey, K. Gillemot, GOLLUM: a next-generation simulation tool for electron, thermal and spin transport, New Journal of Physics, 16 (2014) 093029.

[27] A. Animalu, V. Heine, The screened model potential for 25 elements, Philosophical Magazine, 12 (1965) 1249-1270.

[28] P. Rong-Gang, C. Hong, P. Rong-Xiang, Investigation of Dilaton–Gluon Coupling Potential in Charmonium Family, Chinese Physics Letters, 23 (2006) 48.

[29] A. Zunger, M.L. Cohen, First-principles nonlocal-pseudopotential approach in the density-functional formalism: Development and application to atoms, Physical Review B, 18 (1978) 5449.

[30] G.B. Bachelet, M. Schlüter, Relativistic norm-conserving pseudopotentials, Physical Review B, 25 (1982) 2103.

[31] J.P. Perdew, A. Zunger, Self-interaction correction to density-functional approximations for many-electron systems, Physical review B, 23 (1981) 5048.

[32] L. Fernández-Seivane, M.A. Oliveira, S. Sanvito, J. Ferrer, On-site approximation for spin–orbit coupling in linear combination of atomic orbitals density functional methods, Journal of Physics: Condensed Matter, 18 (2006) 7999.

[33] P. Haynes, C.-K. Skylaris, A. Mostofi, M. Payne, Elimination of basis set superposition error in linear-scaling density-functional calculations with local orbitals optimised in situ, Chemical physics letters, 422 (2006) 345-349.

[34] G. Alagona, C. Ghio, Z. Latajka, J. Tomasi, Basis set superposition errors and counterpoise corrections for some basis sets evaluated for a few X-. cntdot.. cntdot.. cntdot. M dimers, Journal of Physical Chemistry, 94 (1990) 2267-2273.

[35] M.C. Daza, J. Dobado, J.M. Molina, P. Salvador, M. Duran, J.L. Villaveces, Basis set superposition error-counterpoise corrected potential energy surfaces. Application to hydrogen peroxide··· X (X= F−, Cl−, Br−, Li+, Na+) complexes, The Journal of chemical physics, 110 (1999) 11806-11813.

[36] F.B. Van Duijneveldt, J.G. van Duijneveldt-van de Rijdt, J.H. van Lenthe, State of the art in counterpoise theory, Chemical Reviews, 94 (1994) 1873-1885.

Chapter 3

Theory of single electron transport

In Chapter 2, we explored density functional theory DFT, which is a technique used to determine the electronic structure of an isolated molecule, is known as a close system. The subsequent step involves connecting this isolated molecule to semi-infinite leads and calculating the transmission coefficient across the system. My approach utilises Green's function scattering formalism, which is discussed in this chapter and applied throughout the thesis.

By integrating scattering theory with Green's functions, we can describe the electrical and thermoelectric properties of nanoscale systems placed between multiple macroscopic electrodes.

3.1 Introduction

Molecular electronics aims to explore the electrical behavior of molecular junctions where a molecule or similarly small structure is connected to bulk electrodes, enabling ballistic transport through its energy levels. This setup, where a nanoscale device is created by placing a molecule or another phase-coherent structure between electrodes to conduct current in or out of the device, is known as an open system [1-3].

The coupling strength between the leads and the molecule is generally weaker than the bond strengths within the electrodes or the molecule. This leads to scattering events as electrons move between the electrodes and the molecule. Therefore, a comprehensive approach is necessary to comprehend and compute these scattering processes effectively.

The transport theory for single-molecule junctions relies on scattering theory and the Landauer formula. Although there are multiple ways to examine the electronic properties of these junctions, this thesis focuses mainly on the Green's function formalism. Both analytical and numerical techniques are employed to explore the electronic transport properties of single molecules.

The first goal of this chapter is to begin with a brief overview of the tight-binding model TBM for the description of quantum systems. TBM is a mathematical approach used to describe the movement of electrons in an organic molecular as well in my study, to introduce theoretical approaches for addressing problems in various structured systems. These solutions illustrate fundamental concepts like the Schrödinger wave equation and its common use in calculating the eigenfunctions and eigenvalues of the Hamiltonian matrix, applied to different types of one-dimensional crystalline chains, such as infinite linear chains, finite linear chains. The second goal is to provide an overview of scattering theory and its relation to transport properties and Green's function, exploring different transport regimes and the intriguing features based on the Landauer formalism for estimating the electrical conductance properties of materials.

3.2 Tight-binding model

One of the simplest approaches for quantum transport modelling in small systems uses tight-binding models TBMs, which describe the wave function as a linear combination of atomic orbitals LCAO of localised states. The TBM investigates electronic transport properties by using a Hamiltonian belonging to a finite set of atomic orbitals. This approach assumes that tightly bound electrons within a molecule primarily interact with the nearest neighboring atoms. Solving the Schrödinger wave equation exactly for eigenstates and eigenvalues becomes feasible for systems with a small number of electrons, such as the hydrogen atom. TBMs are valuable in developing essential concepts of quantum transport that are also applicable to more material-specific models based on density functional theory DFT [4, 5]. The time-dependent Schrödinger equation is expressed as follows:

$$H(x)\,\Psi(x,t) = i\hbar \frac{\partial}{\partial t}\,\psi\,(x,t) \tag{3. 2}$$

where Ψ represents the wave function of the quantum system, ħ is the reduced Planck constant $\hbar = \frac{h}{2\,\pi}$, and H is the Hamiltonian, which is given by:

$$H(x) = \frac{-\,\hbar^2}{2\,m}\,\nabla^2 + V(x) \tag{3. 3}$$

We assume that the eigenstate of energy E can be expressed as a product of spatial and time-dependent components.

$$\Psi(x,t) = \Psi(x)\,\theta(t) \tag{3. 4}$$

The Schrödinger equation is subsequently transformed into two ordinary differential equations.

$$\frac{1}{\theta(t)}\frac{d}{dt}\,\theta(t) = \frac{-i\,E}{\hbar} \tag{3. 5}$$

and

$$H\,\Psi(x) = E\,\Psi(x) \tag{3. 6}$$

The solution to equation (3.1) is

$$\Psi(x,t) = \Psi(x)\, e^{\frac{-iEt}{\hbar}} \qquad (3.\,7)$$

This solution can be written as a linear combination of basic functions in the form:

$$\Psi(x,t) = \sum_j \psi_j\, \emptyset_j(x)\, e^{\frac{-iEt}{\hbar}} \qquad (3.\,8)$$

The wave function $\Psi(x)$ can be written as a linear superposition of the form:

$$\Psi(x) = \sum_j \psi_j(t)\, \emptyset_j(x) \qquad (3.\,9)$$

In a TBM, $\emptyset_j\,(x)$ represents a localised basis function on a probability site j and $\psi_j(t)$ is the time-dependent amplitude of the wavefunction on site j. In a TBM, for convenience, the overlap between the basis functions is ignored, and the probability of finding an electron on site j is $\left|\psi_j(t)\right|^2$.

The Hamiltonian matrix elements can be expressed as:

$$H_{i\,j} = \left\langle \emptyset_i(x)\middle|H\middle|\emptyset_j(x)\right\rangle = \int dx\, \emptyset_i^*(x) H\, \emptyset_j(x) \qquad (3.\,10)$$

The following section describes the model of chains, with a single orbital on each atom. Since the electrons interact with their nearest neighbour sites, all terms$\left\langle \emptyset_i\middle|H\middle|\emptyset_j\right\rangle$ with $|i-j|>1$ are small, and therefore neglected.

Picking a particular atom on site j, the time- dependent Schrodinger equation is then given by:

$$i\hbar\frac{\partial\psi_j(t)}{\partial t} = \varepsilon_j\,\psi_j - \gamma_j\,\psi_{j+1}(t) - \gamma_j^*\,\psi_{j-1}(t) \qquad (3.\,11)$$

where $\varepsilon_j = H_{jj}$ is the on-site energy of atomic orbital $j, H_{j,j+1} = -\gamma_j$ is the coupling between sites j and $j+1$, and $H_{j,j-1} = -\gamma_j^*$ is the coupling between sites j and $j-1$. To move from time-dependent to time-independent, you typically assume a separable solution of the form: For the latter $\psi_j(t) = \psi_j\, e^{\frac{-iEt}{\hbar}}$, where ψ_j is independent of time.

$$i\hbar \frac{\partial}{\partial t} \psi_j\, e^{\frac{-iEt}{\hbar}} = \varepsilon_j\, \psi_j\, e^{\frac{-iEt}{\hbar}} - \gamma_j\, \psi_{j+1}\, e^{\frac{-iEt}{\hbar}} - \gamma_j^*\, \psi_{j-1}\, e^{\frac{-iEt}{\hbar}}$$

Now cancel out the common exponential factor $e^{\frac{-iEt}{\hbar}}$ on both sides:

$$E\, \psi_j = \varepsilon_j\, \psi_j - \gamma_j\, \psi_{j+1} - \gamma_j^*\, \psi_{j-1}$$

3.3 The Landauer formula

To describe transport phenomena of non-interacting electrons using the Landauer formula as a theoretical standard model [6-9]. It links the electron's transmission coefficient $T(E)$ to the electronic conductance through one-dimensional structures with two terminals.

To clarify this, consider a mesoscopic scatterer connected to two ideal ballistic leads functioning as electron reservoirs, as illustrated in **Figure 3. 1**. The system consists of a scattering region linked to two leads, each of which is connected to an electron reservoir. These left L and right R reservoirs are assigned chemical potentials μ_L and μ_R, temperatures T_L and T_R.

Figure 3. 1: A generic scattering region is connected to two ballistic leads with the chemical potentials μ_L, and μ_R, respectively, where r is the amplitude of the reflected wave due to an incoming wave from the left and t is the amplitude of the transmitted wave.

The electron current (I) and can be described as follows:

$$I = {}^{2e}/_{h} \int_{-\infty}^{\infty} dE\, T(E)[f_L(E) - f_R(E)] \qquad (3.\ 12)$$

where: $T(E)$ represents the transmission probability of an electron travelling from the left lead to the right lead through the molecule, e denotes the electron charge, and $f_{\mathrm{L}}(\mathrm{E})$, $f_R(\mathrm{E})$ are the Fermi-Dirac distribution functions for the left and right reservoirs, respectively, defined as:

$$f_{left}\,(E) = \left[e^{\frac{\left(E - E_F^L\right)}{K_B T}} + 1 \right]^{-1}, \qquad f_{right}\,(E) = \left[e^{\frac{\left(E - E_F^R\right)}{K_B T}} + 1 \right]^{-1} \qquad (3.\ 13)$$

Here, T denotes the temperature, k_B is the Boltzmann constant, and [$\mathrm{E}_{\mathrm{f}}^{\mathrm{L}} = \mu_L, \mathrm{E}_{\mathrm{f}}^{\mathrm{R}} = \mu_R$] are the Fermi energies of the left and right reservoirs, respectively. The electrical conductance can be determined at zero voltage and a finite temperature by averaging $T(E)$ over an energy window of width eV centred around the Fermi energy [10]. The electrical conductance, represented as $G = {}^{I}/_{V}$, at zero voltage and finite temperature, is expressed as

$$G = G_0 \int_{-\infty}^{\infty} dE\, T(E) \left(-{}^{df(E)}/_{dE} \right) \qquad (3.\ 14)$$

where G_0 is the quantum of conductance is equal to ${}^{2\,e^2}/_{h} = 77.4 \times 10^{-6} s = 77\ \mu s$

$\left(-{}^{df(E)}/_{dE} \right)$ is the probability distribution with a width of approximately $k_B T$.

The electrical conductance is proportional to the transmission coefficient in the limit of zero voltage and zero temperature, the Landauer formula is as follows:

$$G = G_o T(E_F) \qquad (3.14)$$

3.4 Green’s functions

Green's functions are useful for calculating the transmission and reflection coefficients of various nanoscale structures. This section will thoroughly explain the methods used, starting with Green's functions for different nanoscale systems. First, the form of Green's function of a doubly infinite chain will be discussed. Then, the form of Green's function of a semi-infinite linear chain will be studied. Finally, the form of Green’s function of a finite one-dimensional chain will be discussed. Overall, Green's functions of the systems are essential for bridging theoretical predictions with experimental observations in systems involving wires, leads, etc.

3.4.1 Green’s functions of a doubly infinite chain

Consider a doubly infinite chain as depicted in **Figure 3. 2**. It consists of infinite atoms, each with a single orbital of energy (ε_0). Additionally, there is a site (j) between two atoms that facilitates 'hopping energies' couplings with the nearest neighbour, denoted by (γ) and(k) is the wave vector [11, 12].

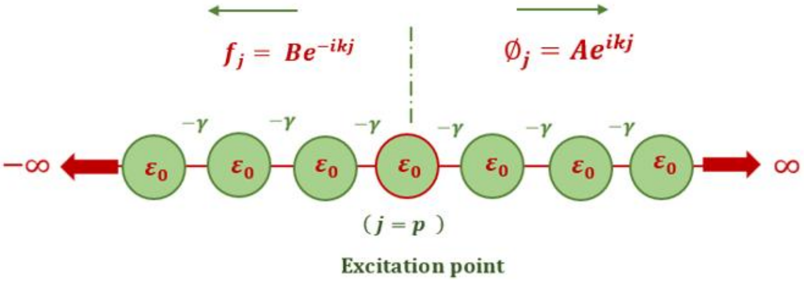

Figure 3. 2: Representation of tight binding model of one-dimensional infinite chain with on-site energies ε_0 and couplings $-\gamma$.

For an eigenstate of energy E, the wavefunction amplitudes are of the form $\psi_j(t) = \psi_j\, e^{\frac{-iEt}{\hbar}}$, where ψ_j is independent of time and the time-independent Schrödinger equation takes the form

$$\begin{pmatrix} -\infty & . & . & . & . & . & . & . & . \\ . & . & . & . & . & . & . & . & . \\ . & . & \varepsilon_\circ & -\gamma & 0 & 0 & 0 & . & . \\ . & . & -\gamma & \varepsilon_\circ & -\gamma & 0 & 0 & . & . \\ . & . & 0 & -\gamma & \varepsilon_\circ & -\gamma & 0 & . & . \\ . & . & 0 & 0 & -\gamma & \varepsilon_\circ & -\gamma & . & . \\ . & . & 0 & 0 & 0 & -\gamma & \varepsilon_\circ & . & . \\ . & . & . & . & . & . & . & . & . \\ . & . & . & . & . & . & . & . & +\infty \end{pmatrix} \begin{pmatrix} . \\ . \\ . \\ \psi_{j-1} \\ \psi_j \\ \psi_{j+1} \\ . \\ . \\ . \end{pmatrix} = E \begin{pmatrix} . \\ . \\ . \\ \psi_{j-1} \\ \psi_j \\ \psi_{j+1} \\ . \\ . \\ . \end{pmatrix}$$

More compactly, this can be written

$$(E - H)|\psi\rangle = 0 \qquad \rightarrow \quad H\psi = E\psi \qquad (3.\ 15)$$

The Green's function $G(E)$, which is described by the Hamiltonian H, is defined to satisfy:

$$(E - H)G(E) = I \qquad (3.\ 16)$$

Here I is the identity matrix.

Where G_{jp} can be chosen as the retarded Green's function [1], which describes the system's response at point j to a source at point p. To clarify the relationship between Green's functions and the wavefunctions generated by a source, it is helpful to use the following notation.

$$G_{jp} = \psi_j^{(p)} \qquad (3.\ 17)$$

where G_{jp} is the element of Green's matrix located in the p^{th} column and j^{th} row, and $\psi_j^{(p)}$ is the amplitude of the column vector $\psi^{(p)}$ at site j.

In general, equation (3.16) can be expressed as follows:

$$\sum\nolimits_p^{\infty} (E - H)\ G_{jp}(E) = \delta_{jp} \qquad (3.\ 18)$$

or equivalently

$$\sum_{p=-\infty}^{\infty} HG_{jp}(E) = EG_{jp}(E) - \delta_{jp} \tag{3. 19}$$

Here, δ_{jp} is the Kronecker delta, which satisfies.

$$\delta_{jp} = \begin{cases} 1 & if \quad j = p \\ 0 & if \quad j \neq p \end{cases}$$

Now, we can substitute the equation (3.17) into equation (3.19) we obtain

$$\sum_{p=-\infty}^{\infty} H_{jp} \; \psi_j^{(p)} = E\psi_j^{(p)} - \delta_{jp} \tag{3. 20}$$

This is quite similar to the Schrödinger equation, except for the Kronecker delta on the right side. Thus, we can substitute the Hamiltonian equation into equation (3.20):

$$\varepsilon_o \, \psi_j^{(p)} - \gamma \, \psi_{j-1}^{(p)} - \gamma \, \psi_{j+1}^{(p)} = E \, \psi_j^{(p)} - \delta_{jp} \tag{3. 21}$$

The solution to equation (3.21) can be represented as:

$$\psi_j^{(p)} = \emptyset_j = A \, e^{ikj} for \qquad j > p \tag{3. 22}$$

$$\psi_j^{(p)} = f_j = B \, e^{-ikj} \, for \qquad j < p \tag{3. 23}$$

- For $j = p + 1$, equations (3.21) and (3.22) result in:

$$\varepsilon_o \, \phi_{p+1} - \gamma \, \psi_p^{(p)} - \gamma \, \phi_{p+2} = E \, \phi_{p+1} \tag{3. 24}$$

Since ϕ_j satisfies equation (3.20) for all values of j, we can derive:

$$\varepsilon_o \, \phi_{p+1} - \gamma \, \phi_p - \gamma \, \phi_{p+2} = E \, \phi_{p+1} \tag{3. 25}$$

By comparing equations (3.24) and (3.25), we obtain

$$\psi_p^{(p)} = \phi_p \tag{3. 26}$$

- For $j = p - 1$, the identical process is applied, leading to:

$$\psi_p^{(p)} = f_p \tag{3. 27}$$

Therefore, equations (3.26) and (3.27) give rise to the following:

$$\psi_p^{(p)} = \phi_p = f_p \tag{3. 28}$$

$A\ e^{ikp} = B\ e^{-ikp}$ where $A\ = C\ e^{-ikp}$ and $B = C\ e^{ikp}$, hence

$$\rightarrow \emptyset_j = A\ e^{ikj} \qquad \therefore \emptyset_j = C\ e^{-ikp}\ e^{ikj} \tag{3. 29}$$

$$\phi_j = Ce^{ik(j-p)} \text{ and } f_j = Ce^{-ik(j-p)} \tag{3. 30}$$

where C is a constant. By incorporating these equations with equations (3.22) and (3.23) we obtain:

$$\psi_j^{(p)} = Ce^{ik|j-p|} \tag{3. 31}$$

where

$$C = \frac{1}{2i\gamma\ sin\ k} = \frac{1}{i\hbar v(E)} \tag{3. 32}$$

Here $v(E)$ is the group velocity. Thus, the Green's function for an infinitely long chain in both directions is:

$$G_{jp}(E) = \psi_j^{(p)} = \frac{e^{ik|j-p|}}{i\hbar v(E)}$$

Hence, the most general solution is:

$$G_{jp}(E) = \psi_j^{(p)} = \frac{e^{ik|j-p|}}{i\hbar v(E)} + Ae^{ikj} + Be^{-ikj} \tag{3. 33}$$

By selecting arbitrary constants A and B as $A = -\frac{e^{ik(j-p)}}{i\hbar v}$ and $B = -\frac{e^{-ik(j-p)}}{i\hbar v}$, the Green's function is derived, known as the advanced Green's function (the complex conjugate of the retarded Green's function).

$$G_{jp}(E) = \psi_j^{(p)} = -\frac{e^{-ik(E)|j-p|}}{i\hbar v(E)} \tag{3. 34}$$

3.4.2 Green’s functions of a semi-infinite linear chain

Here, this system resembles the previous one, with the exception that one lead extends infinitely in one direction and is finite in the opposite direction, as depicted in **Figure 3. 3**.[11, 13, 14].

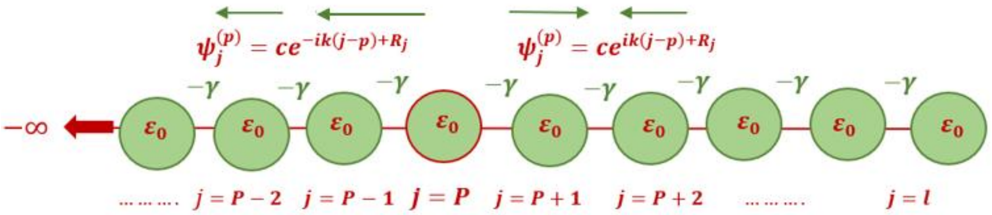

Figure 3. 3: Representation of tight binding model of semi-infinite linear chain with site energies ε_0 and hopping elements $-\gamma$, which terminates at site $j = l$.

Considering the semi-infinite chain depicted in **Figure 3. 3**, with site energies ε_0 and hopping elements $-\gamma$, where the chain ends at site $j = l$, where $l \geq p$, however, the site $j = l + 1$ is missing results in the following boundary condition.

$$\psi^{p}_{l+1} = 0 \tag{3. 35}$$

As depicted in **Figure 3. 3**, when the incoming plane wave e^{ikj} strikes the end of the chain, a reflected plane wave e^{-ikj} is generated, a reflected wave $R_j = Be^{-ikj}$. Consequently, this reflected wave is incorporated into the retarded Green's function.

$G_{jp}(E) = e^{ik(j-p)} + B\ e^{-ikj}$ if we choose the site $j = l + 1$, from (3.35).

$G_{jp}(E) = e^{ik(l+1-p)} + B\ e^{-ik(l+1)} = 0 \quad \rightarrow \quad B\ e^{-ik(l+1)} = -e^{ik(l+1-p)}$

$$B = -e^{ik(l+1-p)}.e^{ik(l+1)} \qquad \rightarrow \qquad B = -e^{ik(2l+2-p)} \tag{3. 36}$$

From equation (3.36) into the retarded Green's function of a semi-infinite linear chain is

$$G_{jp}(E) = \psi^{(p)}_{j} = \frac{e^{ik(E)|j-p|} + B\ e^{-ik(E)|j|}}{i\hbar v(E)}$$

$$G_{jp}(E) = \psi^{(p)}_{j} = \frac{e^{ik(E)|j-p|} - e^{-ik(E)|j|}e^{ik(E)|2l+2-p|}}{i\hbar v(E)}$$

$$G_{jp}(E) = \psi^{(p)}_{j} = \frac{e^{ik(E)|j-p|} - e^{-ik(E)(j+p-2l-2)}}{i\hbar v(E)} \tag{3. 37}$$

This satisfies, $\psi^{p}_{l+1} = \psi^{l+1}_{j} = 0$. Likewise, if the chain terminates at site $l \le p$, the first missing site is $j = l - 1$ and the boundary condition becomes $\psi^{p}_{l-1} = 0$. This leads to Green's function:

$$G_{jp}(E) = \psi^{(p)}_{j} = \frac{e^{ik(E)|j-p|} - e^{ik(E)(j+p-2l+2)}}{i\hbar v(E)} \tag{3. 38}$$

Consider that in both cases, Green's function on the terminal site $j = p = l$ is

$$G_{ll}(E) = -\frac{e^{ik(E)}}{\gamma} \tag{3. 39}$$

This is referred to as the surface Green's function.

3.4.3 Green’s function of a finite one-dimensional chain

To derive the Green's function for a finite one-dimensional chain, consider a linear chain consisting of N tight-binding sites with free-end boundary conditions, as depicted in **Figure 3. 4**. Consequently, the Green's function should be zero at site $j = 0 \; and \; j = N + 1$. [11, 15]

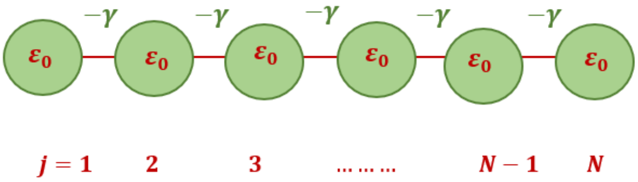

Figure 3. 4: A finite one-dimensional chain with on-site energies ε_0 and hopping elements $-\gamma$.

To achieve this, Green’s function should be expressed as follows:

$$G_{jp}(E) = \begin{cases} A \sin kj \,, & j \leq p \\ B \sin k[j - (N+1)], & j \geq p \end{cases} \qquad (3.\,40)$$

This ensures that the boundary conditions are met, and that continuity is maintained at $j = p$ yields.

$$A \sin kp = B \sin k[p - (N+1)]$$

The constants A and B must be selected as:

$$A = C \sin k[p - (N+1)] \; and \; B = C \sin kp \qquad (3.\,41)$$

Here C is a constant.

Hence, equation (3.40) can be rewritten as:

$$G_{jp}(E) = \begin{cases} C\, sin\, k[p - (N+1)]\, sin\, kj, & j \leq p \\ C\, sin\, (p)\, sin\, k[j - (N+1), & j \geq p \end{cases} \tag{3. 42}$$

Then C can be determined as:

$$C = {}^{1}/_{\gamma\, sin\, k\, sin\, k(N+1)} \tag{3. 43}$$

From equation (3.42), it is evident that Green's function diverges when $\sin k(E)(N+1) = 0$, meaning $k(E) = {}^{n\,\pi}/_{(N\,+\,1)}$, where n is an integer. At the gap center $E = 0$, where $k = {}^{\pi}/_{2}$, C diverges when N is odd. For even N (i.e., $N = 2n$), the magic number table can be represented as:

$$M_{jp} = \frac{G_{jp}(0)}{C}$$

$$\therefore\ M_{jp} = \begin{cases} (-1)^{n+1}\, sin\frac{\pi\, j}{2}\, cos\frac{\pi\, p}{2}, & j \leq p \\ (-1)^{n+1}\, sin\frac{\pi\, p}{2}\, cos\frac{\pi\, j}{2}, & j \geq p \end{cases} \tag{3. 44}$$

This implies that $M_{jp} = 0$ if both j and p are either odd or even. Additionally, for $j \leq p$, $M_{jp} = 0$ if j is even or p is odd, and for $j \geq p$, $M_{jp} = 0$ if p is even or j is odd. Otherwise, $|M_{jp}| = 1$.

3.5 Scattering matrix

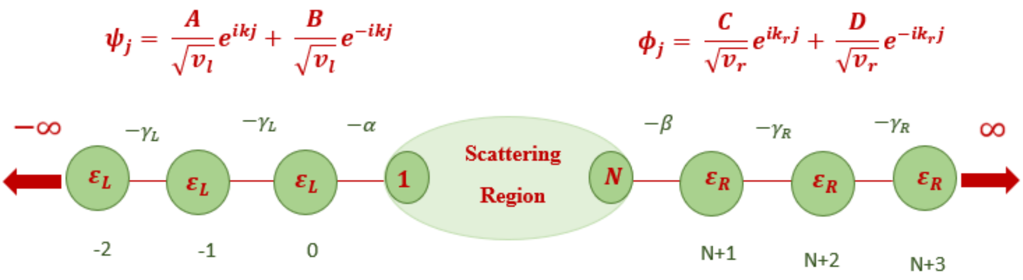

Figure 3. 5: Illustrates a system comprising a scattering region leads attached to two distinct semi-infinite.

Figure 3. 5 shows the system encompasses a scattering region with N sites $(j = 1,2, \dots .N)$, connected to one-dimensional leads from both left and right sides through matrix elements $(-\alpha, -\beta)$. The right lead includes sites $(N + 1, N + 2, \dots . . \infty)$, while the left lead includes sites $(-1, -2, \dots . -\infty)$. Here, $-\gamma_R \ and - \gamma_L$represents the nearest coupling on the right and left sides, respectively. Understanding the transmission coefficient described in the equations mentioned above requires the computation of the scattering matrix. This matrix characterises the connection between incoming and outgoing waves and their dependence on the electron's energy E. To derive this, we examine the solution of the time-independent Schrödinger equation for an electron within the left and right electrodes in one dimension [11, 16]. The eigenstate of the electron within the left electrode can be expressed as:

$$\psi_j = \frac{A}{\sqrt{v_l}}e^{ikj} + \frac{B}{\sqrt{v_l}}e^{-ikj} \tag{3. 45}$$

In this context, v_l presents the group velocity within the left electrode, and A and B denote the amplitudes of the incoming and outgoing waves traveling from the left to the right. The current per unit energy of the eigenstate is given by:

$$I_{left} = |A^2| - |B^2| \tag{3. 46}$$

Similarly, for the right electrode, the eigenstate of the electron can be expressed as:

$$\phi_j = \frac{C}{\sqrt{v_r}} e^{ik_r j} + \frac{D}{\sqrt{v_r}} e^{-ik_r j} \tag{3. 47}$$

The current per unit energy is determined as follows:

$$I_{right} = |C^2| - |D^2| \tag{3. 48}$$

where C and D represent the amplitudes of the two incoming and outgoing waves traveling to the right and left, respectively. Given that the currents adhere to the relationship

$$I_{left} = I_{right}$$

$$|A| - |B| = |C| - |D| \tag{3. 49}$$

Hence,

$$|A^2| + |B^2| = |C^2| + |D^2| \tag{3. 50}$$

Because the incoming current equals the outgoing current, the wave functions for both electrodes are correspondingly interconnected.

$$\psi_j = Ae^{ikj} + Be^{-ikj} \tag{3. 51}$$
$$\phi_j = Ce^{ikj} + De^{-ikj} \tag{3. 52}$$

Since the scattering matrix represents the connection between incoming waves and outgoing coefficients, and it conforms to:

$$\begin{pmatrix} B \\ C \end{pmatrix} = \begin{pmatrix} S_{11} & S_{12} \\ S_{21} & S_{22} \end{pmatrix} \begin{pmatrix} A \\ D \end{pmatrix} \tag{3. 53}$$

$$B = S_{11} A + S_{12} D \tag{3. 54}$$

$$C = S_{21} A + S_{22} D \tag{3. 55}$$

In this context, B and C represent the amplitudes of incoming plane waves carrying the electrons through the scatterer, while A and D represent the amplitudes of outgoing waves. To understand the components of the scattering matrix, two scenarios are examined. In the first case, where $A = 1$ and $D = 0$, $B = r$ and $C = t$, where r is the amplitude of the reflected wave resulting from an incoming wave from the left, and t is the amplitude of the transmitted wave.

$$\begin{pmatrix} B \\ C \end{pmatrix} = \begin{pmatrix} S_{11} \\ S_{21} \end{pmatrix} \tag{3. 56}$$

In this case, S_{11} and S_{21}represent the reflection (r) and the transmission (t) respectively, related to an incident wave from the left. In the second scenario, where $A = 0$ and $D = 1$, then:

$$\begin{pmatrix} B \\ C \end{pmatrix} = \begin{pmatrix} S_{12} \\ S_{22} \end{pmatrix} \tag{3. 57}$$

$S_{12}$and S_{22}denote the reflection (r) and transmission (t) coefficients, respectively, corresponding to an incident wave from the right. In summary, the transmission and reflection coefficients are expressed as elements of the scattering matrix, which is given by:

$$S = \begin{pmatrix} r & t' \\ t & r' \end{pmatrix} \tag{3. 58}$$

It is important to note that the matrix S is a unitary matrix, meeting the condition:

$$ss^{-1} = ss^{\dagger} = 1 \tag{3. 59}$$

This implies that the current conveyed by incoming waves equals the current conveyed by outgoing waves. Consequently, the sum of transmission and reflection probabilities amounts to unity.

$$|t|^2 + |r|^2 = 1$$

$$T(E) + R(E) = 1 \tag{3. 60}$$

Here, t represents the amplitude of transmitted wave functions, r denotes the amplitude of reflected waves, $T(E)$ stands for the transmission coefficient, and $R(E)$ signifies the reflection coefficient.

3.6 Transmission coefficient of an arbitrary scattering region

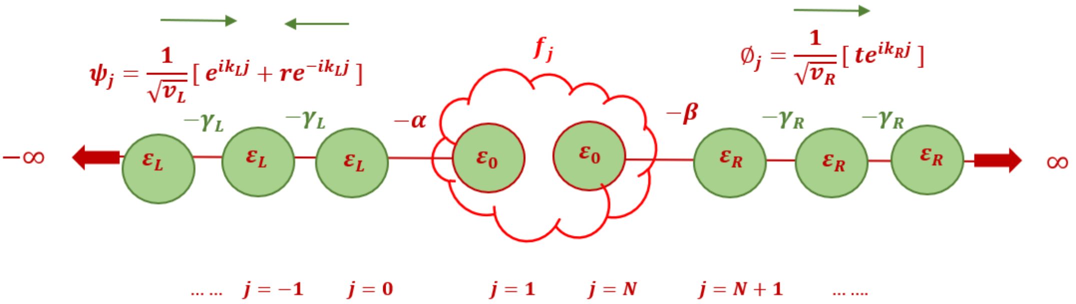

Figure 3. 6: Illustrates a system comprising a scattering region leads attached to two distinct semi-infinite.

To derive a general formula for the transmission coefficient within any arbitrary scattering region, we examine the configuration illustrated in **Figure 3. 6**. This setup comprises two semi-infinite chains, where the site energies and hopping elements in the left (right) lead are denoted as $\varepsilon_L(\varepsilon_R)$ and $-\gamma_L(-\gamma_R)$ respectively. These leads are linked to the scattering region at sites 1 and N by couplings $-\alpha$ and $-\beta$, respectively [11, 17, 18].

Our objective is to find a solution to the Schrödinger equation.

$$\sum_{l=-\infty}^{\infty} H_{jl}\psi_l = E\psi_j$$

The amplitudes of the eigenvectors ψ_j for the left lead, ϕ_j for the right lead, and f_j for the scattering region are considered, where the plane waves are normalised to unit current.

$$\psi_j = \frac{1}{\sqrt{v_L}}\left[e^{ik_L j} + re^{-ik_L j}\right] \tag{3. 61}$$

$$\phi_j = \frac{1}{\sqrt{v_R}}\left[te^{ik_R j}\right] \tag{3. 62}$$

The Schrödinger equation is expressed as follows:

$$\varepsilon_L\psi_j - \gamma_L\psi_{j-1} - \gamma_L\psi_{j+1} = E\psi_j \qquad for \quad j < 0 \tag{3. 63}$$

$$\varepsilon_L\psi_o - \gamma_L\psi_{-1} - \alpha f_1 = E\psi_o \qquad for\ j = 0 \tag{3. 64}$$

$$\textstyle\sum_{l=1}^{N} H_{jl}f_l - \alpha\psi_o\delta_{j1} - \beta\phi_{N+1}\delta_{jN} = E\,f_j \qquad for \quad 1 \le j \le N \tag{3. 65}$$

$$\varepsilon_R\phi_{N+1} - \gamma_R\phi_{N+2} - \beta f_N = E\phi_{N+1} \qquad for \quad j = N+1 \tag{3. 66}$$

$$\varepsilon_R\phi_j - \gamma_R\phi_{j+1} - \gamma_R\phi_{j-1} = E\phi_j \qquad for \quad j > N+1 \tag{3. 67}$$

Equation (3.65) could be rewritten as:

$$|f\rangle = g|s\rangle \tag{3. 68}$$

where,

$$g = (EI - H)^{-1}$$

g: represents the Green's function of an isolated scatterer. $|s\rangle$ denotes the source, which is a zero vector with non-zero elements only at the connection points (at site $j = 1$ and $j = N$).

$$|f\rangle = \begin{pmatrix} f_1 \\ f_2 \\ . \\ . \\ f_N \end{pmatrix} \qquad |s\rangle = \begin{pmatrix} -\alpha\psi_o \\ o \\ o \\ o \\ -\beta\phi_{N+1} \end{pmatrix}$$

For the junction depicted in Figure (3.5), the state $|f\rangle$ is characterised by only two non-zero elements because of the source. Consequently, equation (3.68) can be expressed as follows:

$$\begin{pmatrix} f_1 \\ f_N \end{pmatrix} = \begin{pmatrix} g_{11} & g_{1N} \\ g_{N1} & g_{NN} \end{pmatrix} \begin{pmatrix} -\alpha\psi_o \\ -\beta\phi_{N+1} \end{pmatrix} \tag{3. 69}$$

$$\tilde{g}^{-1} \begin{pmatrix} f_1 \\ f_N \end{pmatrix} = \begin{pmatrix} -\alpha\psi_o \\ -\beta\phi_{N+1} \end{pmatrix} \tag{3. 70}$$

$\tilde{g}^{-1}$ represents the inverse of the 2×2 submatrix of the Green's function. By applying the recurrence relation, we derive the following:

$$\gamma_L\psi_1 = \alpha f_1$$

$$\gamma_R\phi_N = \beta f_N$$

Based on equations (3.61) and (3.62), we obtain:

$$\phi_{N+1} = \phi_N e^{ik_R} \tag{3. 71}$$

$$\psi_1 = \frac{1}{\sqrt{v_L}}[2i \sin k_L] + \psi_o e^{-ik_L} \tag{3. 72}$$

Hence,

$$\begin{pmatrix} -\alpha\psi_o \\ -\beta\phi_{N+1} \end{pmatrix} = \Sigma \begin{pmatrix} f_1 \\ f_N \end{pmatrix} + \begin{pmatrix} \frac{\alpha\, e^{ik_L}}{\sqrt{v_L}}\,[2i\, sin\, k_L] \\ 0 \end{pmatrix} \tag{3. 73}$$

where

$$\Sigma = \begin{pmatrix} \Sigma_L & O \\ O & \Sigma_R \end{pmatrix}$$

$\Sigma_L = \frac{-\alpha^2 e^{ik_L}}{\gamma_L}$, $\Sigma_R = \frac{-\beta^2 e^{ik_R}}{\gamma_R}$. These are the self-energies corresponding to the left and right leads, respectively. By substituting equation (3.73) into equation (3.70), we get:

$$((\tilde{g})^{-1} - \Sigma\,)\begin{pmatrix} f_1 \\ f_N \end{pmatrix} = \begin{pmatrix} \frac{\alpha\, e^{ik_L}}{\sqrt{v_L}}\,[2i\, sin\, k_L] \\ 0 \end{pmatrix} \tag{3. 74}$$

Thus,

$$\begin{pmatrix} f_1 \\ f_N \end{pmatrix} = G \begin{pmatrix} \frac{\alpha\, e^{ik_L}}{\sqrt{v_L}}\,[2i \sin k_L] \\ 0 \end{pmatrix} \tag{3. 75}$$

where

$$G = ((\tilde{g})^{-1} - \Sigma\,)^{-1} = \begin{pmatrix} G_{11} & G_{12} \\ G_{N1} & G_{NN} \end{pmatrix} \tag{3. 76}$$

From equation (3.75),

$$f_N = G_{N1}\,\frac{\alpha e^{ik_L}}{\sqrt{v_L}}\,[2i\, sin\, k_L] = \frac{\gamma_R}{\beta}\,\phi_N \tag{3. 77}$$

Since $\emptyset_N = \frac{1}{\sqrt{v_R}}\left[t e^{ik_R N}\right]$, $\hbar v_R = 2\gamma_R \sin k_R$ and $\hbar v_L = 2\gamma_L \sin k_L$, we obtain the following:

$$t = iG_{N1}\alpha\,\beta e^{ik_L}\sqrt{\frac{2\, sin\, k_L}{\gamma_L}}\;\sqrt{\frac{2\, sin\, k_R}{\gamma_R}}\quad e^{-ik_R N} \tag{3. 78}$$

$$T(E) = |\, t \,|^2 = 4 \left[\frac{\alpha^2 \, sin \, k_L}{\gamma_L}\right] \left[\frac{\beta^2 \, sin \, k_R}{\gamma_R}\right] \; |G_{N1}|^2 \tag{3. 79}$$

Since $|G_{N1}|^2 \; = \left|\frac{g_{N1}}{\Delta}\right|^2$

where $\Delta = 1 - g_{11}\, \Sigma_L - \; g_{NN}\, \Sigma_R + \Sigma_L \, \Sigma_R [g_{11} \; g_{NN} - g_{1N} \, g_{N1}]$

Therefore, the most general formula used to calculate the transmission probability of any scattering region connected to various one-dimensional leads [1] is as follows:

$$T(E) = |\, t \,|^2 = 4 \left[\frac{\alpha^2 \, sin \, k_L}{\gamma_L}\right] \left[\frac{\beta^2 \, sin \, k_R}{\gamma_R}\right] \; \left|\frac{g_{N1}}{\Delta}\right|^2 \tag{3. 80}$$

3.7 Thermoelectricity

In the 19th century, Seebeck, Peltier, and Thompson discovered the relationships between heat, current, temperature, and voltage [1]. The Seebeck coefficient $S(E_F)$ is defined as the voltage difference $\Delta V = V_1 - V_2$ generated by a temperature difference $\Delta T = T_1 - T_2$ between two electrodes connected to hot and cold reservoirs, respectively [7, 19]. In the following discussion, the sign of the Seebeck coefficient is analysed based on whether the transmission is dominated by the HOMO or LUMO peak.

3.7.1 The sign of Seebeck coefficient $S(E_F)$

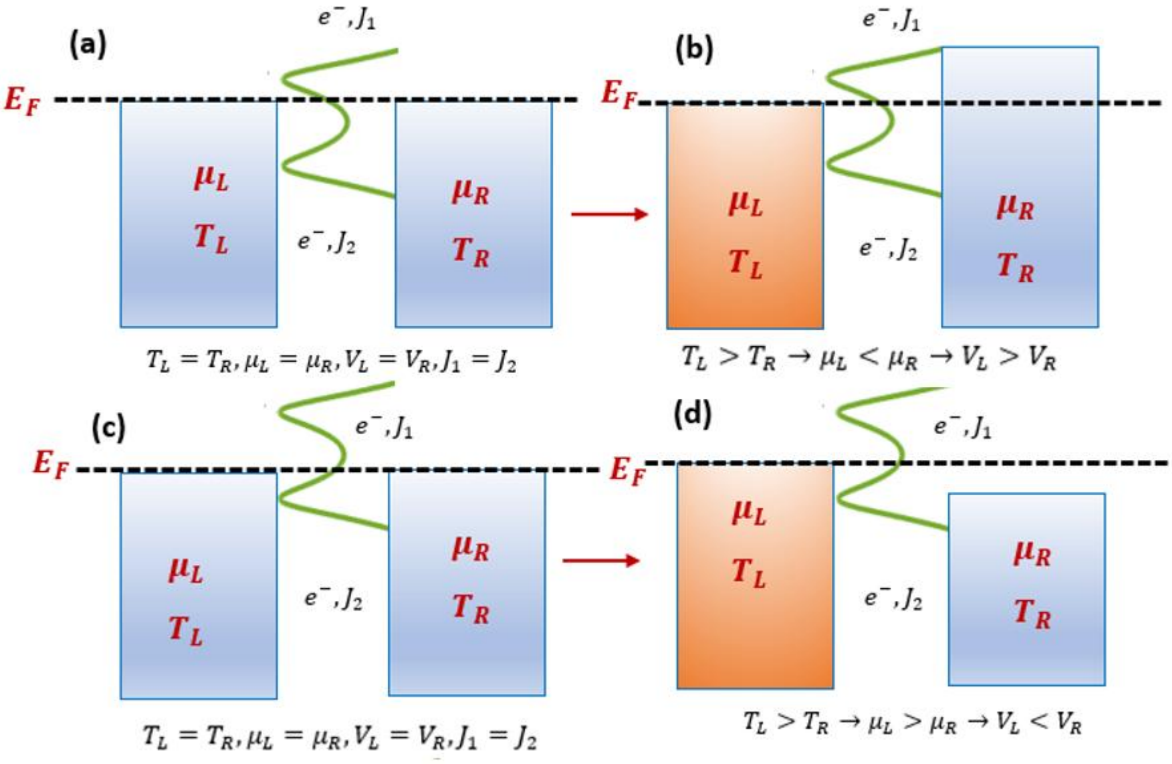

Figure 3. 7: The Seebeck coefficient displays different signs depending on whether the system is dominated by the LUMO (**a, b**) and HOMO-dominated (**c, d**) transport. Transport dominated by the LUMO results in a negative Seebeck coefficient, whereas HOMO-dominated transport produces a positive Seebeck coefficient.

Figure 3. 7 illustrates the energy level alignment in molecular devices consisting of two electrodes connected to reservoirs labelled L and R, along with a single molecule. The reservoirs are characterised by voltages and temperatures denoted as V_L, T_L and V_R, T_R, respectively. Let the voltage difference be $\Delta V = V_L - V_R$ and the temperature difference be $\Delta T = T_L - T_R$. The chemical potentials are defined as $\mu_L = E_F + eV_L$ and $\mu_R = E_F + eV_R$, where $e = -|e|$, and their difference is $\Delta\mu = \mu_L - \mu_R = e\,\Delta V$.

The steady-state particle current J_1 represents the rate at which electrons move from reservoir L to reservoir R through the scattering region. In contrast, J_2 represents the reverse flow from R to L. The net particle current, J, is given by $J = J_1 - J_2$, and the corresponding electrical current is $I = e\,J$, with $e = -|e|$.

In **Figure 3. 7b** and **Figure 3. 7d**), the Seebeck coefficient, $S(E_F)$, is defined as $S = -\frac{\Delta V}{\Delta T}\Big|_{I=0}$ where $\Delta V = V_L - V_R$ is the open-circuit voltage generated by a temperature difference $\Delta T = T_L - T_R$.To determine the sign of the Seebeck coefficient $S(E_F)$, begin with the equilibrium condition where $\varDelta V = 0$ and $\varDelta T = 0$ **Figure 3. 7a**. Now consider what happens when the temperature T_L of the left reservoir is raised, increasing the proportion of higher-energy electrons in reservoir L compared to reservoir R. If these higher-energy electrons are more likely to pass from reservoir L to R than lower-energy electrons, J_1 will increase, as shown in **Figure 3. 7b** for LUMO-dominated transport.

To maintain steady-state conditions $J = 0$, the chemical potential μ_R must rise, increasing J_2. This shows that when $T_L > T_R$, $\mu_L < \mu_R$. Therefore, if $\Delta T > 0$, $\Delta\mu < 0$, $\Delta V > 0$, and $S < 0$. This behaviour occurs when the Fermi energy is within the HOMO-LUMO gap of a single molecule and closer to the LUMO, where the electron transmission coefficient increases with energy. A similar situation arises when the Fermi energy is within the band gap of a semiconductor and closer to the conduction band.

Conversely, when the Fermi energy is closer to the HOMO or the valence band **Figure 3. 7c**, higher-energy electrons have more difficulty passing from reservoir L to R than lower-energy electrons. In this case, increasing T_L relative to T_R reduces J_1, leading to $S > 0$, as illustrated in **Figure 3. 7d** [20].

3.8 Conclusion

In summary, I discussed a theory of single particle transport, which is the primary numerical tool for studying charge transport through molecules. I explained the theoretical basis for calculating electronic transport and provided a simple derivation of the Landauer formula. Additionally, the transport was described, including Green’s function methods for obtaining the transmission coefficient of semi-infinite leads connected to a scattering region. Therefore, the transmission coefficient has been computed using Green's functions and transport through an arbitrary scattering region. Finally, the sign of the Seebeck coefficient $S(E_F)$, was explained.

3.9 Bibliography

[1] M. Sharma, Quantum transport in nanostructures and molecules: an introduction to molecular electronics: by Colin John Lambert, Bristol, IOP Publishing, 2021, 445 pp., 190(hardback), 159 (e-book), ISBN: 9780750336390. Scope: review. Level: researcher, in, Taylor & Francis, 2022.

[2] E. Scheer, J.C. Cuevas, Molecular electronics: an introduction to theory and experiment, World Scientific, 2017.

[3] S. Sek, K. Swiatek, A. Misicka, Electrical behavior of molecular junctions incorporating α-helical peptide, The Journal of Physical Chemistry B, 109 (2005) 23121-23124.

[4] K. Burke, Perspective on density functional theory, The Journal of chemical physics, 136 (2012).

[5] F. Spiegelman, N. Tarrat, J. Cuny, L. Dontot, E. Posenitskiy, C. Martí, A. Simon, M. Rapacioli, Density-functional tight-binding: basic concepts and applications to molecules and clusters, Advances in physics: X, 5 (2020) 1710252.

[6] R. Landauer, Spatial variation of currents and fields due to localized scatterers in metallic conduction, IBM Journal of research and development, 1 (1957) 223-231.

[7] M. Büttiker, Y. Imry, R. Landauer, S. Pinhas, Generalized many-channel conductance formula with application to small rings, Physical Review B, 31 (1985) 6207.

[8] E. Papp, D.P. Jelenfi, M.T. Veszeli, G. Vattay, A Landauer Formula for Bioelectronic Applications, Biomolecules, 9 (2019) 599.

[9] H. Ness, L. Dash, R. Godby, Generalization and applicability of the Landauer formula for nonequilibrium current in the presence of interactions, Physical Review B—Condensed Matter and Materials Physics, 82 (2010) 085426.

[10] G. Lesovik, Electronic Transport in Meso-and Nano-Scale Conductors, (2008).

[11] C.J. Lambert, Quantum transport in nanostructures and molecules: an introduction to molecular electronics, IoP Publishing, 2021.

[12] D.A. Ryndyk, Theory of quantum transport at nanoscale, Springer Series in Solid-State Sciences, 184 (2016) 9.

[13] Y. Hadad, B.Z. Steinberg, Green's function theory for infinite and semi-infinite particle chains, Physical Review B—Condensed Matter and Materials Physics, 84 (2011) 125402.

[14] M.I. Molina, Nonlinear surface impurity in a semi-infinite two-dimensional square lattice: Green function approach, Physical Review B—Condensed Matter and Materials Physics, 74 (2006) 045412.

[15] S. Cojocaru, Green's function of a finite chain and the discrete Fourier transform, International Journal of Modern Physics B, 20 (2006) 593-605.

[16] P. Sautet, C. Joachim, Electronic transmission coefficient for the single-impurity problem in the scattering-matrix approach, Physical Review B, 38 (1988) 12238.

[17] F. Martelli, F. Tommasi, A. Sassaroli, L. Fini, S. Cavalieri, Verification method of Monte Carlo codes for transport processes with arbitrary accuracy, Scientific reports, 11 (2021) 19486.

[18] K. Xia, M. Zwierzycki, M. Talanana, P. Kelly, G. Bauer, First-principles scattering matrices for spin transport, Physical Review B—Condensed Matter and Materials Physics, 73 (2006) 064420.

[19] N. Claughton, M. Leadbeater, C. Lambert, Theory of Andreev resonances in quantum dots, Journal of Physics: Condensed Matter, 7 (1995) 8757.

[20] Q. Wu, Theory of Molecular-scale Transport in Graphene Nanojunctions, Lancaster University (United Kingdom), 2018.

Chapter 4

Tunnelling quantum interference through molecular junctions formed from cross-linked OPE3 dimers

4.1 Introduction

This research was conducted in collaboration with Prof. Nicholas Long's group (Department of Chemistry, Imperial College London), who suggested the studied molecules used in this work. I performed the theoretical analysis at Lancaster. The study was published under the title:

"Tuning quantum interference through molecular junctions formed from cross-linked OPE3 dimers."

Authored by Bashayr Alanazi, Asma Alajmi, Alaa Aljobory, Colin J. Lambert, and Ali Ismael.

This chapter aims to investigate the impact of quantum interference (QI), in multipath molecules more precisely cross-linked (C-L), using gold as the top and bottom electrodes to introduce symmetry in a single-molecule junction. The structures consist of dimers formed by cross-linking molecular wires, such as oligo phenylene-ethylene (OPE)-based dimers, which feature varying contacts between the molecules and electrodes. OPE derivatives are composed of phenyl rings linked by triple bonds. I demonstrate that the appearance of destructive or constructive quantum interference (DQI and CQI respectively), in cross-linked OPE-based dimers is independent of the nature of the molecular cross-link. Instead, the type of interference is controlled by the connectivity to external electrodes and is determined by the presence or otherwise of meta-connected phenyl rings in the transport path. This opens the way to a novel strategy for memristive switching.

4.2 Motivation

Numerous studies have investigated the phenomenon of quantum interference (QI), employing a variety of approaches to explore its effects. These approaches include investigations based on π-stacked systems [1], analyses of para- and meta-connectivities considered individually[2], studies combining multiple connectivities within a single molecule [3], examinations of fused molecular structures with multiple connectivities [4], and methodologies involving electrochemical oxidation [5]. Despite the diversity of these methodologies, a common focus across all studies has been the evaluation of on-off ratios, which consistently fall within a range of approximately three orders of magnitude. The design of molecular materials studied in this chapter contains oligo phenylene-ethylene OPE3, alkane chain, and phenylene ethynylene chains. Achieving a fundamental understanding of electronic transport through metal-molecule-metal junctions is one of the essential challenges in the molecular electronics field. To increase this understanding, my aim is to understand the molecule deeply, especially the base of molecule OPE3, the bridge including alkane chain, phenylene ethynylene chain, and the role of its anchor group (i.e., thiol) in binding to metal electrode, as pointed out in **Figure 4. 1**. OPEs are structurally unique building blocks in terms of molecular shape versatility, which contain organic molecules composed of repeating units of oligo (phenylene ethynylene) chain. In this study, three benzene rings (phenylene) connected by ethynylene (-C≡C-) linkages [6-11]. The triple bonds in OPEs allow the formation of shape-persistent chromophores by imparting rigidity to the molecules, avoiding the rotational freedom resulting from π-conjugated analogues.

Moreover, the extended π-system of OPEs allows charge transport, which is essential in molecular electronics [6, 12-14]. In contrast, alkanes, also called "Cycloalkanes" with a single ring, follow the general formula C_nH_{2n}, in contrast to the formula for acyclic alkanes, C_nH_{2n+2}. Cycloalkanes have two fewer hydrogen atoms than acyclic alkanes because an additional carbon–carbon bond is required to form the ring structure. The smallest cycloalkane consists of two carbon atoms; the other formula is C_2H_4. However, this study chose alkane, which has four carbon atoms, C_4H_8, this indicates a single pathway for electron flow. This compound is called butene by chemists [15-19]. While in a benzene ring, there are two pathways for electron flow.

In this chapter, the calculations focus on studying the conductance of cross-linked molecules with different bridges. Each molecule possesses four thiol terminal end-groups (*SH*), as shown in **Figure 4. 3**, and is formed from one or more of the building blocks shown in **Figure 4. 1**.

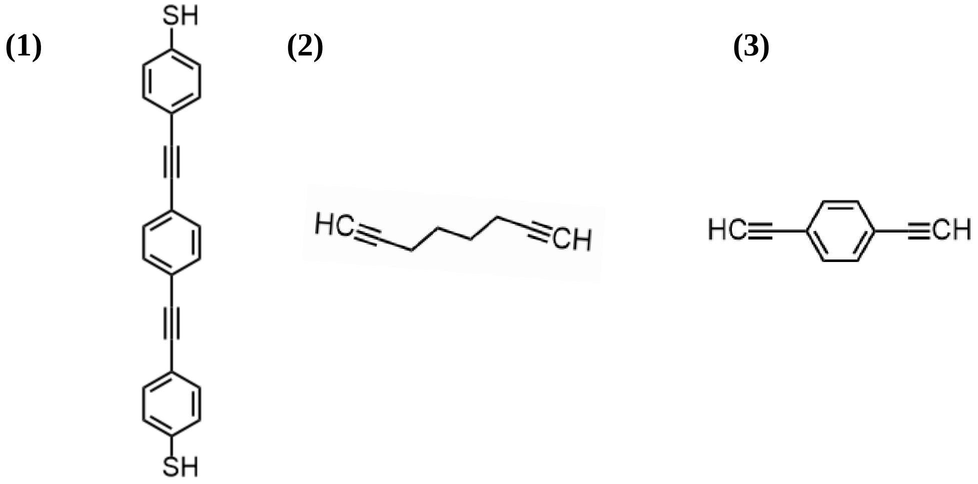

Figure 4. 1: Chemical structures of building blocks used to create OPE3 dimers. **(1)** OPE3, **(2)** alkane, and **(3)** phenylene ethynylene chain.

4.3 Optimised DFT structures of isolated molecules

In this chapter, I will investigate two different cross-linked molecules, which differ according to their bridges. To form a cross-linked dimer, I started with the OPE3 molecular; then I linked two OPE3s together by bridges formed from either an alkane chain to create **1** or a benzene ring to make **2**, for both OPE3 molecules cross-linked the same anchor groups, which involves thiol terminal end-groups (*SH*) [14, 20].

To accurately determine the molecular electronic properties of the molecular junction. I shall start with the theoretical simulations using the density functional DFT code SIESTA. As discussed in Chapter 2, density functional theory DFT calculations played a crucial role in gathering information on these properties, particularly regarding ground-state electron density. The optimal geometries (i.e., ground-state Hamiltonian) of the isolated molecules were obtained by relaxing the molecular structures, these were calculated self-consistently using the DFT code SIESTA [21-23], which applies Troullier-Martins pseudopotentials to account for core electrons and uses a local atomic-orbital basis set to construct the valence states [24, 25]. The optimised geometries of isolated cross-linked dimers were obtained by relaxing the cross-link dimers until the forces on all atoms were reduced to less than 0.01 eV/Å [23], as illustrated in **Figure 4. 2**. I used a double-zeta plus polarization (DZP) orbital basis set, which provides an improved description of the electronic wave functions compared to minimal basis sets. In this approach, each atomic orbital is represented by two basis functions (zeta functions) rather than one, allowing for greater flexibility in capturing the shape and variation of orbitals during bonding., norm-conserving pseudopotentials, the local density approximation (LDA) exchange-correlation functional, and a 250 Rydberg energy cut-off to define the real space grid were employed. Additionally, I also computed results using the generalised gradient approximation (GGA) with Perdew-Burke-Ernzerhof (PBE) parameterisation and found that the resulting electronic properties were comparable with those derived from LDA [26, 27]. The electronic properties of the cross-linked (C-L) dimers were modelled using a combination of DFT and quantum transport theory.

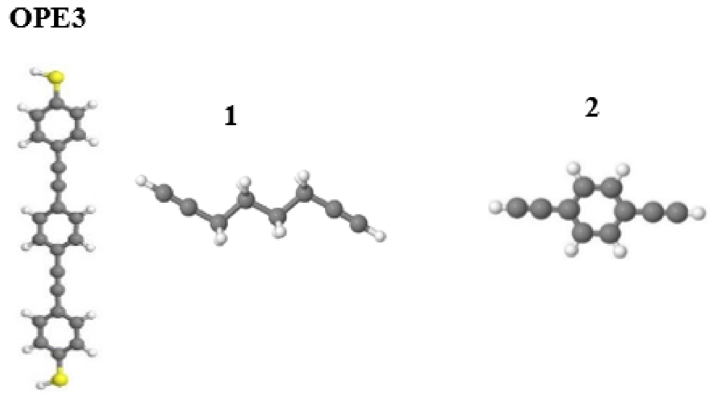

Figure 4. 2: Fully relaxed isolated molecules of three single components, OPE3 and **1-2** components.

The following two molecular structures were the two OPE3s linked together by bridges formed from either an alkane chain to create C-L**1** or a highly conjugated phenylene ethynylene chain to create C-L**2**, and then allowing the system to become fully relaxed to form cross-linked dimers as shown in **Figure 4. 3**.

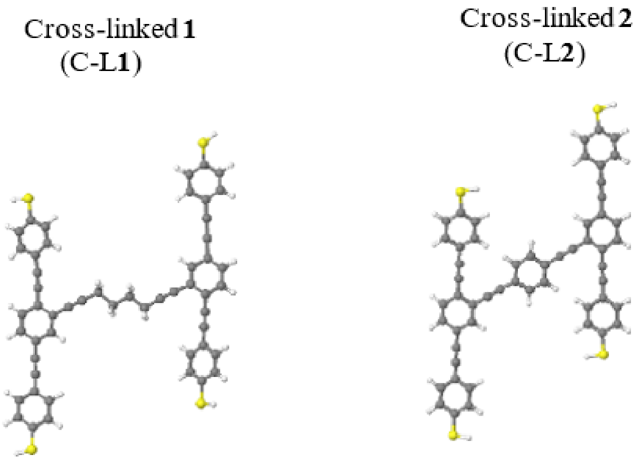

Figure 4. 3: Schematic illustrations of two OPE3 molecules bridged by **1** and **2** components (see Figure 4. 2), to form cross-linked dimers: (C-L**1**) and (C-L**2**).

4.4 Frontier orbitals for the studied molecules

To better understand the electronic properties of the studied molecular structures shown in **Figure 4. 3**, the methods introduced in Chapter 2 have been employed. Initially, the frontier orbitals of all the gas-phase molecules were examined. Plots of the frontier orbitals for the OPE molecule and cross-linked dimers are given in **Figure 4. 4** and **Figure 4. 5**, which show the highest occupied molecular orbitals (HOMO) and lowest unoccupied orbitals (LUMO), (HOMO-1), and (LUMO+1), (HOMO-2), and (LUMO+2) along with their energies. The blue and red colours represent regions of positive and negative orbital amplitudes. In the C-L**1** and C-L**2**, each degenerate pair is weakly coupled, and the degeneracy is slightly lifted. Consequently, as shown in **Figure 4. 4** and **Figure 4. 5**, the LUMO and LUMO+1 of each dimer is almost degenerate, and similarly, the HOMO and HOMO-1 are almost degenerate. It should be noted that both C-L**1** and C-L**2** have degeneracies in their HOMO and LUMO levels.

4.4.1 Cross-linked molecule C-L1

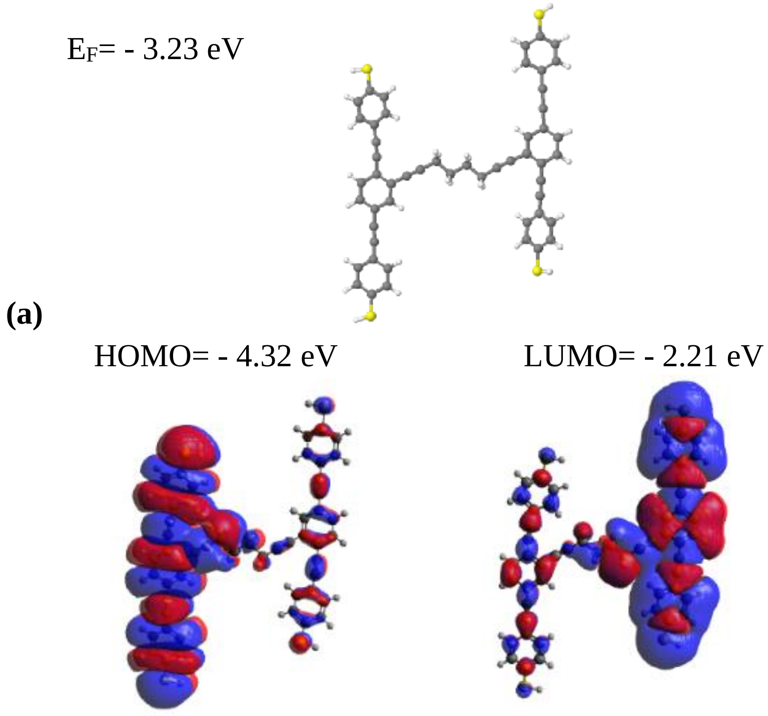

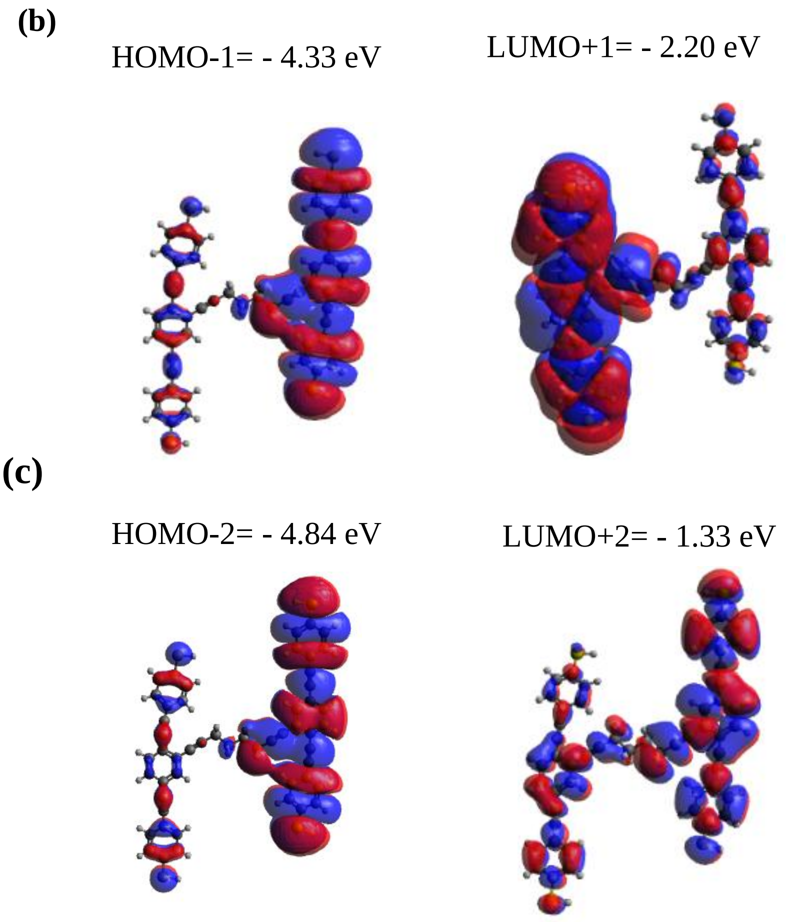

Figure 4. 4: Wave function for cross-linked C-L**1**. **Top panel**: fully optimised geometry of C-L**1**. **Lower panel**: HOMO, LUMO, HOMO-1, LUMO+1, HOMO-2, LUMO+2 of cross-linked **1**, along with their energies.

4.4.2 Cross-linked molecule C-L2

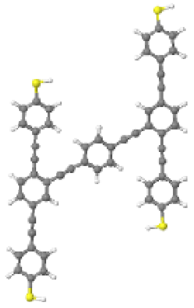

E_F= - 3.58 eV

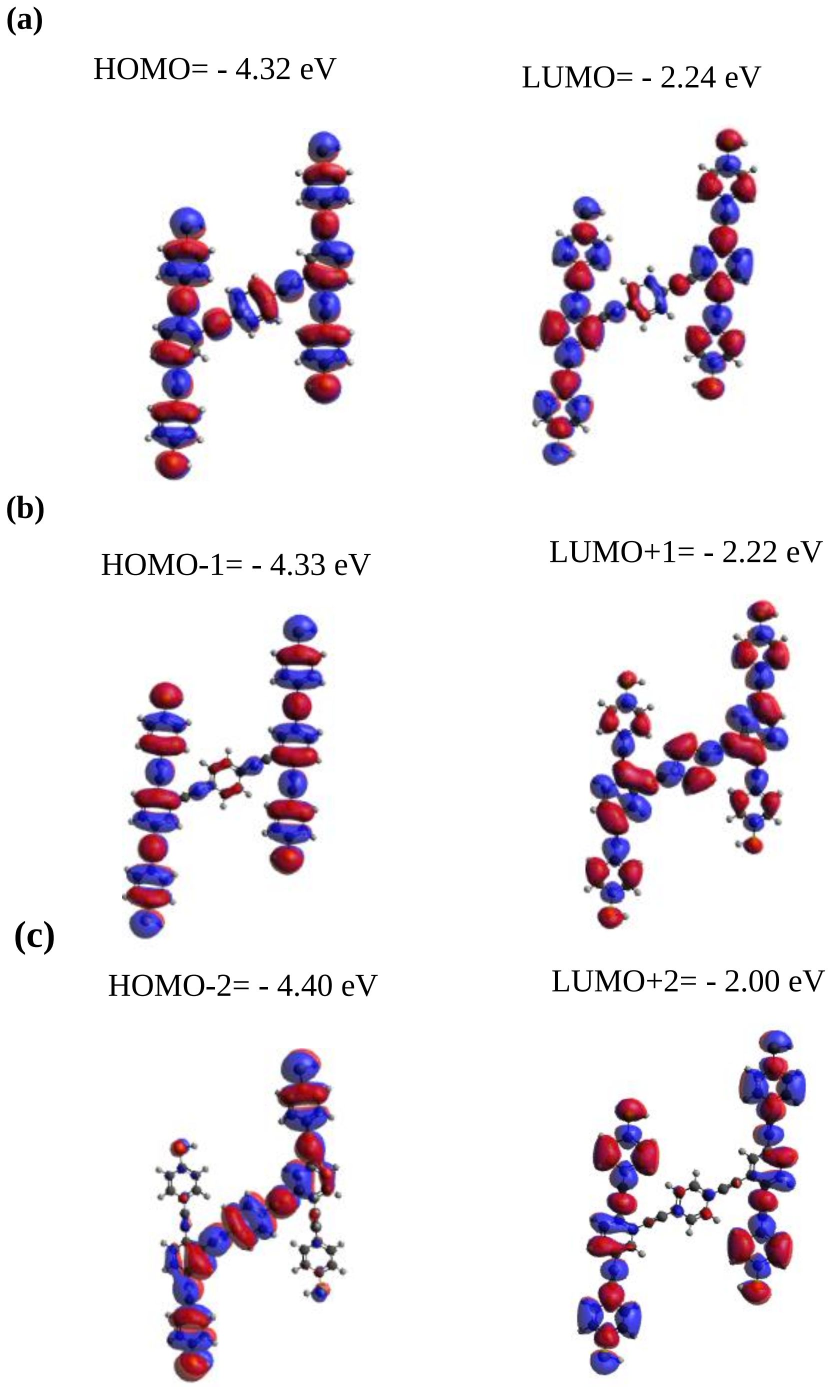

Figure 4. 5: Wave function for cross-linked C-L**2**. **Top panel**: fully optimised geometry of C-L**2**. **Lower panel**: HOMO, LUMO, HOMO-1, LUMO+1, HOMO-2, LUMO+2 of cross-linked C-L**2**, along with their energies.

4.5 Orbital product rule (OPR)

The orbital product rule OPR is a concept used to predict quantum interference effects in molecular systems, particularly in molecular electronics. A deeper understanding of the relationship between molecular orbitals and electron transport through a molecule can be obtained by evaluating whether the orbitals' phases contribute to constructive CQI or destructive DQI quantum interference [28, 29]. It is worth mentioning that the studied molecules possess four potential contacting points (**1, 2, 3** and **4**), as shown in **Figure 4. 6** below.

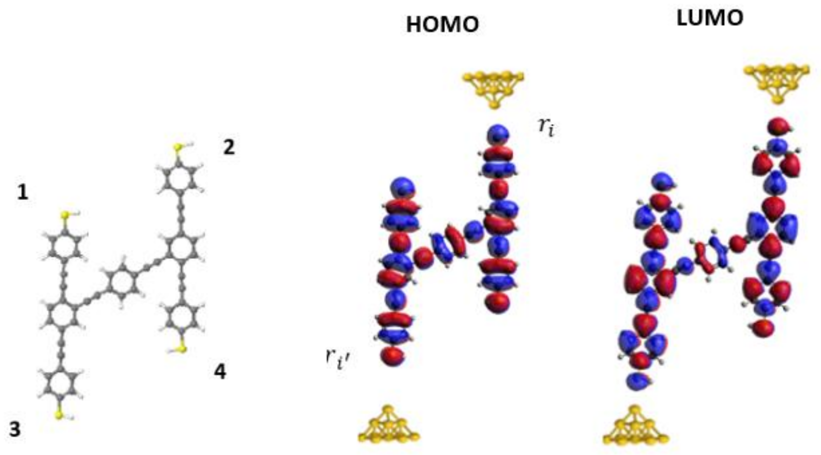

Figure 4. 6: A C-L**2** representation and frontier molecular orbitals of C-L**2** (Note: Au electrodes added here just to show the contacting points).

To understand the relationship between molecular orbitals (MOs) and electrical conductance, we need to understand the electronic structure of a molecule. Electrical conductance depends on the availability of orbitals that electrons can occupy and move through and how easily electrons can transition between these states. We can estimate the electrical conductance ($\sigma_{ii'}$)

as shown in the equation (4.1), if the current enters at the point (r_i) and exits at the point $(r_{i'})$, as shown in **Figure 4. 6** above.

$$\sigma_{ii'} \propto (\psi^H_{(r_i)}\psi^H_{(r_{i'})})^2 \tag{4. 1}$$

$\psi^H_{(r_i)}, \psi^H_{(r_{i'})}$: are the amplitude of the MO at both the entry and exit points, respectively.

For a single-orbital molecule, (e.g., containing a HOMO only) the electrical conductance $(\sigma_{ii'})$ is proportional to $(g_{ii'})^2$, where:

$$g_{ii'} = C_H\psi^H_{(r_i)}\psi^H_{(r_{i'})} \tag{4. 2}$$

C_H: is a constant of proportionality and the quantity $g_{ii'}$ is a Green's function of our fictitious single-orbital molecule. Quantum interference QI between molecular orbitals becomes important when a molecule containing two or more orbitals (e.g., a HOMO and a LUMO) is positioned in a junction, allowing electrons to pass through it from one connection point to another (i.e., r_i and $r_{i'}$). If the molecules possess only a HOMO and a LUMO, then

$$g_{ii'} = C_H\psi^H_{(r_i)}\psi^H_{(r_{i'})} + C_L\psi^L_{(r_i)}\psi^L_{(r_{i'})} \tag{4. 3}$$

In this case, if the HOMO product $\psi^H_{(r_i)}\psi^H_{(r_{i'})}$is negative, whereas the LUMO product $\psi^L_{(r_i)}\psi^L_{(r_{i'})}$ is positive, this connectivity corresponds to constructive inter-orbital QI and the conductance $\sigma_{ii'}$ will be high. However, if the HOMO product $\psi^H_{(r_i)}\psi^H_{(r_{i'})}$ is negative and the LUMO product $\psi^L_{(r_i)}\psi^L_{(r_{i'})}$is also negative. Hence, this connectivity corresponds to destructive inter-orbital QI and $(\sigma_{ii'})$ will be low. For example, as shown in **Figure 4. 6**. The HOMO product $\psi^{H}_{(2)}\psi^{H}_{(3)}$is negative, whereas the LUMO product $\psi^{L}_{(2)}\psi^{L}_{(3)}$ is negative, so this connectivity corresponds to destructive inter-orbital QI. In other words, the conductance is predicted to be low.

In this study, after calculating wavefunction plots for the two cross-linked dimers, as shown in **Figure 4. 4** and **Figure 4. 5**. In this section, I will apply the orbital product rule on them. To use the OPR rule, two contact points are needed, however, in our case there are many pairs and as follows: **1-3**, **2-4**, **1-2**, **3-4**, **1-4**, and **2-3**. These six pairs of contacting points are shown in **Figure 4. 7**.

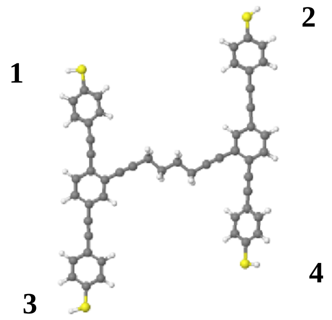

Figure 4. 7: Schematic illustration of a cross-linked (C-L), wire with four possible contact points (**1-4**). The Four contact points lead to 6 pair of contacting points **1-3**, **2-4**, **1-2**, **3-4**, **1-4**, and **2-3**.

Table 4. 1 illustrates the orbital product rule predictions for the two studied molecules: cross-linked **1** and cross-linked **2** (C-L**1** and C-L**2**). The product rule applies to the six contact points to determine whether the quantum interference is constructive CQI or distractive DQI. The OPR predicts a constructive quantum interference CQI for the contact points **1-3**, **2-4**, **1-2** and **3-4**. On the other hand, it predicts destructive quantum interference DQI for the contact points

1-4, and **2-3**. These predictions for the cross-linked **1** and the cross-linked **2** are presented in the second and third rows of **Table 4. 1**.

Table 4. 1: Orbital Product rule predictions of six contact points **1-3**, **2-4**, **1-2**, **3-4**, **1-4**, and **2-3**, for cross-linked dimers C-L**1** and C-L**2** (Note: C for constructive and D for destructive QI).

Cross-linked	Contact points	OPR prediction	wavefunction plot Figure
C-L**1**	**1-3, 2-4** **1-2, 3-4** **1-4, 2-3**	C, C C, C D, D	Figure 4. 4(a) Figure 4. 4(a) Figure 4. 4(a)
C-L**2**	**1-3, 2-4** **1-2, 3-4** **1-4, 2-3**	C, C C, C D, D	Figure 4. 5(a) Figure 4. 5(a) Figure 4. 5(a)

4.6 Renormalisation method

The renormalisation method is introduced and explained to analyse the electron's behaviour within the ring. In 1872, Kekulé proposed the first structure for benzene molecule, which was made up of a six-membered ring where single and double bonds alternate between the carbon atoms, with each carbon atom bonded to one hydrogen. When two substituents that indicate when the part of a molecule that we change is a specific atom or molecular fragment [9, 30, 31] are present on a benzene ring, as shown in **Figure 4. 8**, three possible constitutional isomers can form. The positions of the substituents can be identified either by numbering the carbon atoms in the ring or by using the terms "*ortho*, *meta*, and *para*". These substituent effects refer to the changes in a reaction or property of the unchanged part of a molecule that occurs due to variations in the substituent. The 1,2-positions correspond to *ortho*, 1,3-positions to *meta*, and

1,4-positions to *para*. These substituents can be utilised to control chemical reactions and properties predictably.

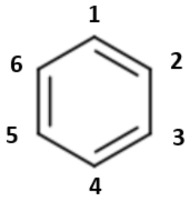

Figure 4. 8: Structural diagram illustrating the benzene ring.

4.6.1 *Ortho*-connected

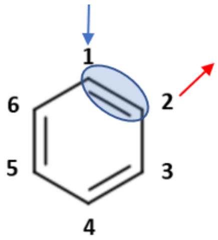

Figure 4. 9: Schematic of the structure of the benzene ring with *ortho* connectivity.

Figure 4. 9 shows the *ortho* connectivity is defined by injecting electrons at atom number 1 and collecting electrons at atom number 2. The two substituents are attached to adjacent carbon atoms. This means they are right next to each other on the ring. *Ortho* substituents can donate electron density, as these positions experience enhanced electron density through resonance [31-34]. In *ortho*-connected molecules, the anticipated quantum interference QI is predicted to be constructive quantum interference CQI.

4.6.2 *Meta*-connected

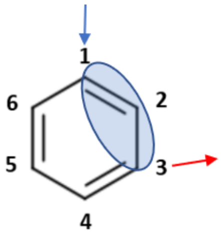

Figure 4. 10: Schematic of the structure of the benzene ring with *meta* connectivity.

Figure 4. 10 shows that the *meta* connectivity occurs when electrons are injected into atom number 1 and collected in atom number 3. The substituents are separated by one carbon atom (i.e., atom number 2). In this arrangement, they are one carbon apart on the ring. *Meta* positions are usually preferred when the substituent is an electron-withdrawing group, as they are less influenced by electron-donating resonance effects [9, 32-34]. In *meta*-connected molecules, the type of quantum interference QI that will occur can be predicted to be destructive quantum interference DQI.

4.6.3 *Para*-connected

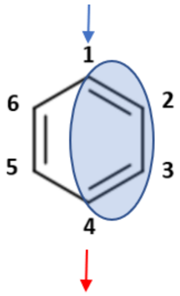

Figure 4. 11: Schematic of the structure of benzene ring with *para* connectivity.

Figure 4. 11 shows that parity is defined by injecting electrons at atom number 1 and collecting them at atom number 4. The substituents are located on opposite sides of the ring,

directly across from each other, with two carbon atoms in between (i.e., 2 and 3). *Para* positions are often more reactive when the substituent can donate electrons [9, 32-34]. The expected quantum interference QI can be predicted for *para*-connected molecules as constructive quantum interference CQI.

4.7 Binding energies

In order to examine the OPR predictions, we need to attach the isolated cross-linked dimers to two metal electrodes to calculate the conductance and compare it against the OPR predictions. First, I need to determine the distance between the isolated molecule and the electrodes. To calculate the distance between two objects, I need to find the binding energy, defined as the optimum distance between two objects. The binding energy is calculated using the DFT method, which is required to calculate the ground state energy of the total system. Using DFT code more precisely SIESTA, these types of calculations are subject to errors [35-37]. A major problem with this kind of simulations is that the interaction energies in closing atoms due to the overlap of their basic functions, which affects the system's total energy. These errors can be eliminated by applying the counterpoise (CP) correction. A possible explanation is calculating the energy in the same total basis set ($\boldsymbol{AB}$) by removing the numerical errors using the “ghost” states (basis set functions with no electrons or protons) in SIESTA [23]. Thus, the following equation can express the total energy of the systems ($\boldsymbol{A}$) and ($\boldsymbol{B}$) on the dimer basis.

$$\text{Binding Energy} = \mathrm{E}_{\mathrm{AB}}^{\mathrm{AB}} - \mathrm{E}_{\mathrm{A}}^{\mathrm{AB}} - \mathrm{E}_{\mathrm{B}}^{\mathrm{AB}} \qquad (4.\ 4)$$

The optimised geometries of the isolated molecules were obtained in the earlier study to model the electrode configuration. These molecules were then attached to a gold electrode at the anchor groups. Considering the nature of the binding, which depends on the structure of the gold surface, the binding to an Au on the surface has been determined, with the anchor atom binding at a "top" site, and subsequently varied the binding distance ($\boldsymbol{d}$). This section calculates the binding energies to determine the optimal distance between the Au electrode and the anchor groups (*S*) for each configuration (refer to **Figure 4. 12**). For more details about calculating the binding energy please see section (2.6.3) in chapter 2.

4.7.1 Au-S

In this section, **Figure 4. 12**, $B.E$ represents the binding energy between the thiol anchor group (*SH*) and the gold lead; d is 2.4 Å, at approximately $-0.94\ eV$. This result is in agreement with the literature review; it should be noted that the *SH* group cleaves when this group is brought close to the Au metal to form the *S-Au* bond [38, 39].

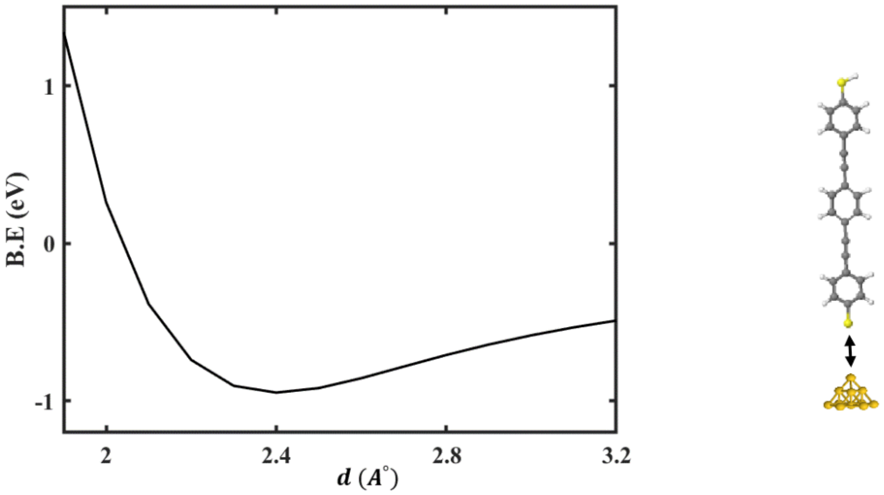

Figure 4. 12: Right panel: represents OPE3 molecule binding to a gold atom. **Left panel:** Binding energy as a function of the optimum binding distance d, where d is found to be approximately 2.4 Å, and binding energy $B.E =\ 0.94\ eV$.

4.8 Cross-linked dimers in Au-Au junction

Using the optimised structures and geometries for the compounds obtained as described above, I employed the SIESTA code to calculate self-consistent optimised geometries, ground state Hamiltonians and overlap matrix elements for the studied molecules. This study aims to compute the electrical conductance of these OPE3 dimers (**1-2**) when only two of the four thiols are connected to two metal electrodes as shown in **Figure 4. 14** and **Figure 4. 15** allowing the current to flow from one electrode to the other through the dimer. In this section, I have selected the C-L**2** as an example to illustrate the pathways of electron transport leading to quantum interference, as shown in **Figure 4. 13**, the C-L**2** with six different possible options for thiol pair including **1-3**, **2-4**, **1-2**, **3-4**, **1-4**, and **2-3** and labelled (**a-f**). To anticipate the role of quantum interference, I note that the triple bond labelled '**a**' is *para*-connected to triple bond '**b**', and following the discussion in section 4.6, since *para* connectivity corresponds to constructive quantum inference CQI, electrons travelling from thiol **1** to thiol **3** are expected to experience CQI and the corresponding electrical conductance is expected to be high (please see Renormalisation section). Similarly, since triple bond '**e**' is *para*-connected to triple bond '**f**', electrons travelling from thiol **2** to thiol **4** (or from thiol **1** to thiol **3),** are expected to experience CQI, resulting in high electrical conductance. On the other hand, triple bond '**a**' is *ortho*-connected to triple bond '**c**', and triple bond '**e**' is *meta*-connected to triple bond '**d**'. Since *meta*-connectivity corresponds to destructive quantum interference DQI, electrons travelling from thiol **1** to thiol **2**, (or from thiol **3** to thiol **4**) are expected to experience DQI, leading to a low electrical conductance. It should be noted that electrons travelling from thiol **1** to thiol **2** pass through the *ortho* path '**a**'- '**c**' and the *meta* path '**d**'- '**e**'. Similarly, from thiol **3** to thiol **4**, there is '**a**' *meta* path '**b**'- '**c**' and an *ortho* path '**d**'- '**f**'. Since the *meta* paths lead to DQI, the conductance of molecules connected to electrodes via the thiol pairs **1-2** or **3-4** is expected to be low up to this point. Four thiol pairs are explored: **1-3**, **2-4**, **1-2**, **3-4**, and the predicted trend is either CQI (**1-3** and **2-4**) or DQI (**1-2** and **3-4**). Next, I consider the electrical conductance when electrodes are connected to thiols **1** and **4** or **2** and **3**. Since the **1-4** path includes *ortho* '**a**'- '**c**' and *ortho* '**d**'- '**f**', we expect it to exhibit CQI and high electrical conductance. In contrast, the **2-3** connectivity to electrodes involves the *meta*-connected paths '**e**'- **d**' and '**c**'- '**d**', leading to DQI and therefore, low electrical conductance is anticipated. For more information about *para, meta* and *ortho* behaviour in terms high or low conductance please see section (4.6).

Also, in this section, the studied systems are sandwiched between two gold electrodes for molecules C-L**1** and C-L**2** with six different options for thiol pair including **1-3**, **2-4**, **1-2**, **3-4**, **1-4**, and **2-3** and labelled (**a-f**) as shown in **Figure 4. 14** and **Figure 4. 15**, for the two cross-linked dimers (**1** and **2**).

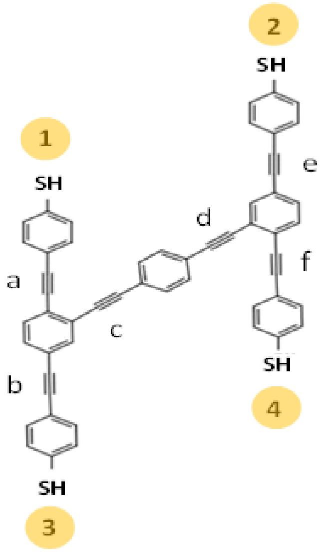

Figure 4. 13: Schematic illustration of the six different contact points: (**1-3**), (**2-4**), (**1-2**), (**3-4**), (**1-4**), and (**2-3**).

4.8.1 Cross-linked (1) possible contact points

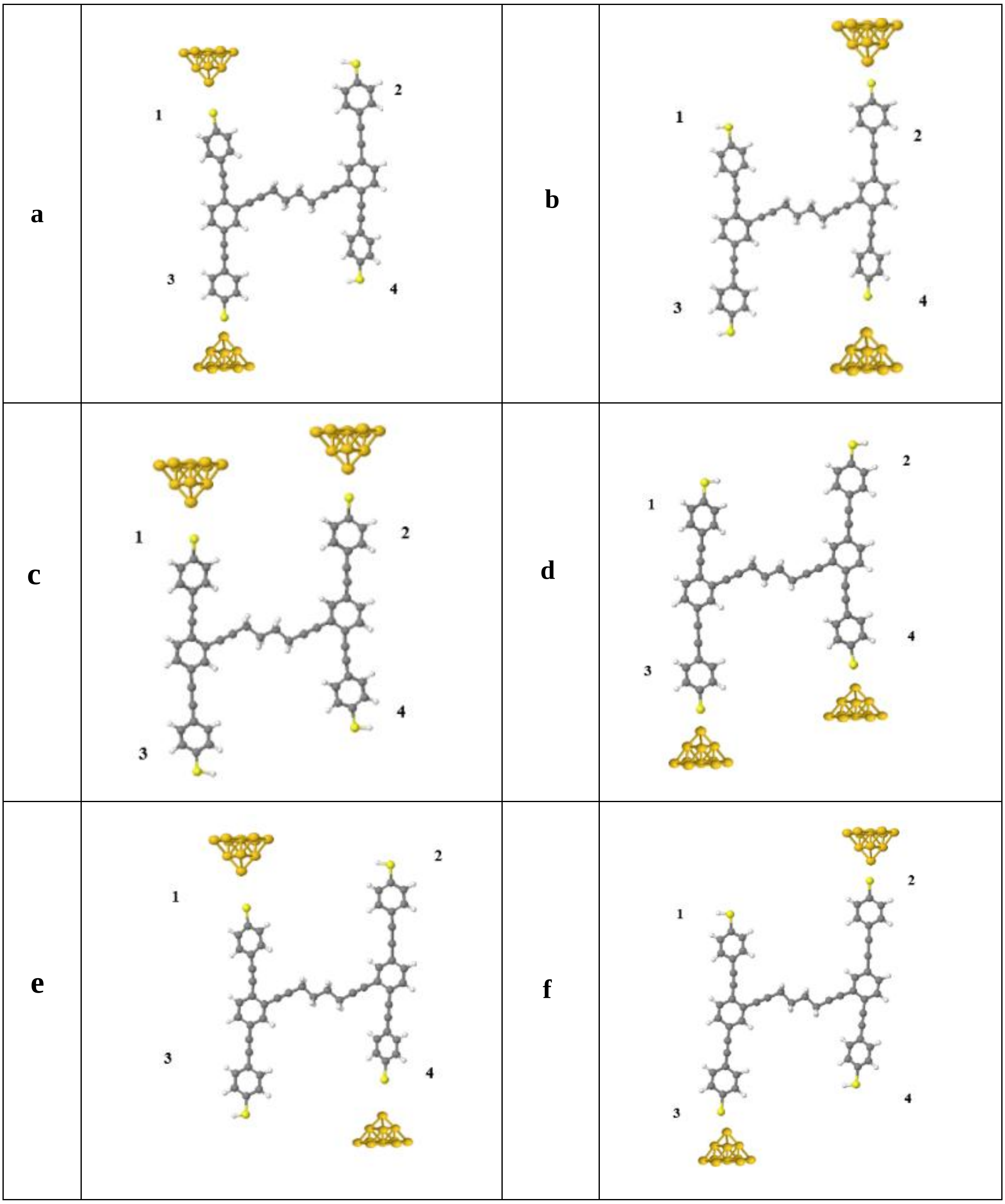

Figure 4. 14: Schematic illustration of the Au/C-L**1**/Au junctions in six different contact points: a (**1-3**), b (**2-4**), c (**1-2**), d (**3-4**), e (**1-4**), and f (**2-3**).

4.8.2 Cross-linked (2) possible contact points

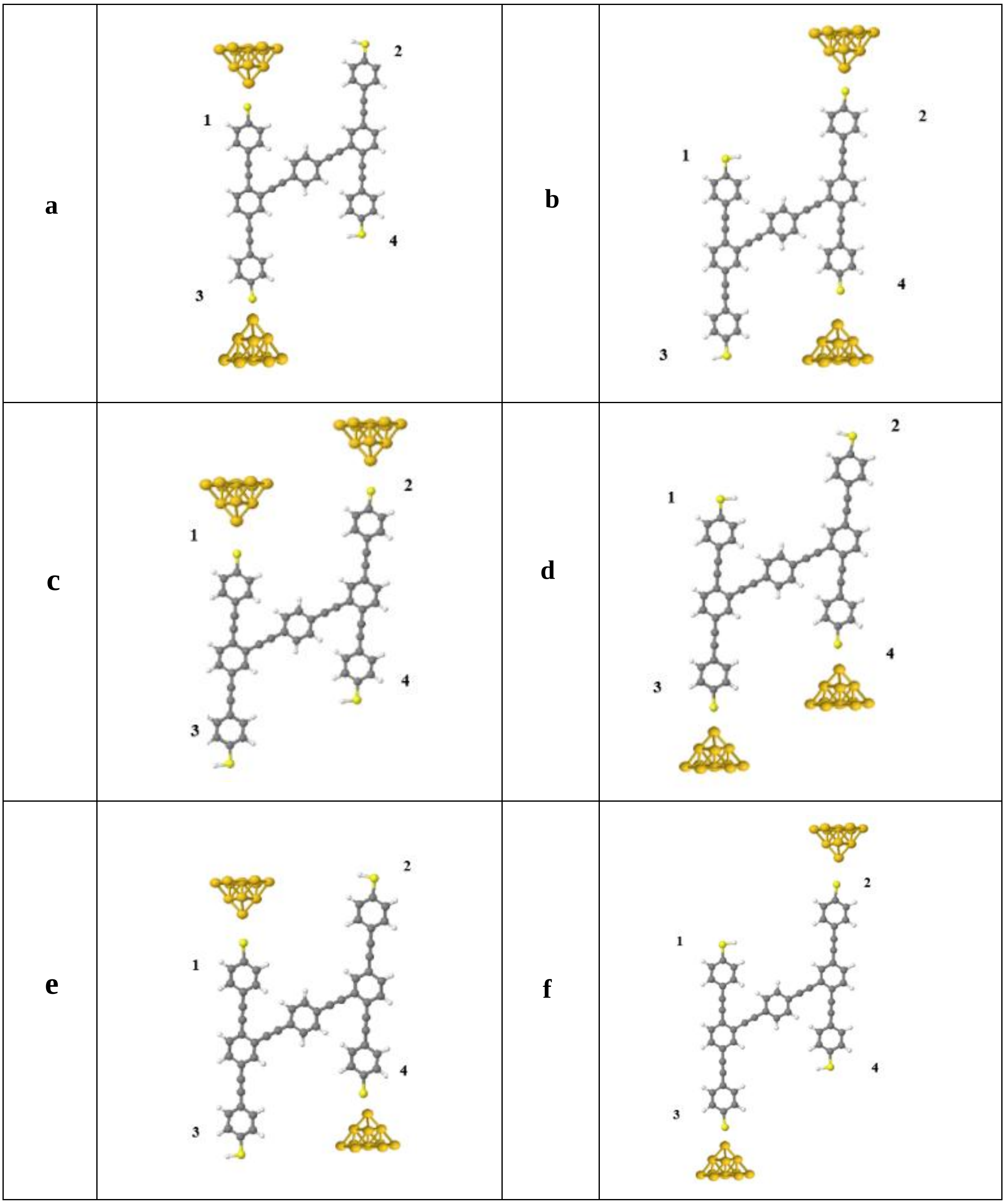

Figure 4. 15: Schematic illustration of the Au/C-L**2**/Au junctions in six different contact points: a (**1-3**), b (**2-4**), c (**1-2**), d (**3-4**), e (**1-4**), and f (**2-3**).

Now, after presenting the possible contact points for both cross-linked molecules, I shall examine the orbital product rule OPR, first by a tight binding model TBM, then by DFT simulations.

4.9 Tight binding model (TBM)

Here, I construct a Huckel (i.e., tight binding, TB) Hamiltonian [40-49], which characterises the two-contact points dependence of the conductance for the two cross-linked dimers on their connectivity to metal electrodes as shown in **Figure 4. 14** and **Figure 4. 15** (Note: In the tight-binding model TBM, the electrodes are represented by carbon chains, whereas in the DFT calculations, the electrodes are modeled as gold (Au)). The Hamiltonian matrix comprises of diagonal elements $H_{jj} = \varepsilon_j$, which describe the energy ε_j of an electron on-site j and nearest neighbour off-diagonal elements H_{ij}, which include hopping integrals between neighbouring sites l and j. All other matrix elements are set to zero. If all the sites were identical, the simplest model would be obtained by setting all $\varepsilon_j = 0$ (which defines the zero of energy) and all nearest neighbour coupling equal to -1, which sets the energy scale. Such a Hamiltonian is a simple connectivity table whose entries H_{ij} are equal to -1 when two atoms i and j are connected and are zero otherwise.

Figure 4. 16 to **Figure 4. 21** represents the transmission coefficient $T(E)$, for cross-linked C-L**1**, obtained using the TBM. Similarly, **Figure 4. 23** to **Figure 4. 28**, show the $T(E)$ for cross-linked C-L**2**. The **Figure 4. 22** and **Figure 4. 29** illustrate similar behaviours, with three junctions resulting in CQI; on the other hand, the remaining junctions result in DQI (the other 3 junctions).

When semi-infinite one-dimensional crystalline leads are linked to sites **1** and **3** (or **2** and **4)**, the $T(E)$ is shown as the red-solid/-dotted curves in **Figure 4. 22** and **Figure 4. 29**, which clearly demonstrates a constructive quantum interference CQI. On the other hand, when crystalline leads are coupled to sites **1** and **2**, the green-solid curve is produced. It possesses a DQI signature (i.e., dip) [43, 45, 50-54]. Similarly, coupled to sites **3** and **4** exhibit DQI as indicated by the green-dotted curve. Moving to sites **1** and **4**, the purple-sold curve is produced and possesses no DQI signature (i.e., CQI), whereas, in sites **2** and **3**, the light, green-sold curve is produced and possesses a DQI dip. These results for the alkane chain bridged (i.e., dimer **1)**. Tight binding transmission coefficients of cross-linked dimers **1** and **2** demonstrate that the bridging linker does not influence the transmission curve behaviour, as the two dimers exhibit roughly the same curves at the six different pairs of contacts.

4.9.1 TBM transport simulation for cross-linked (1)

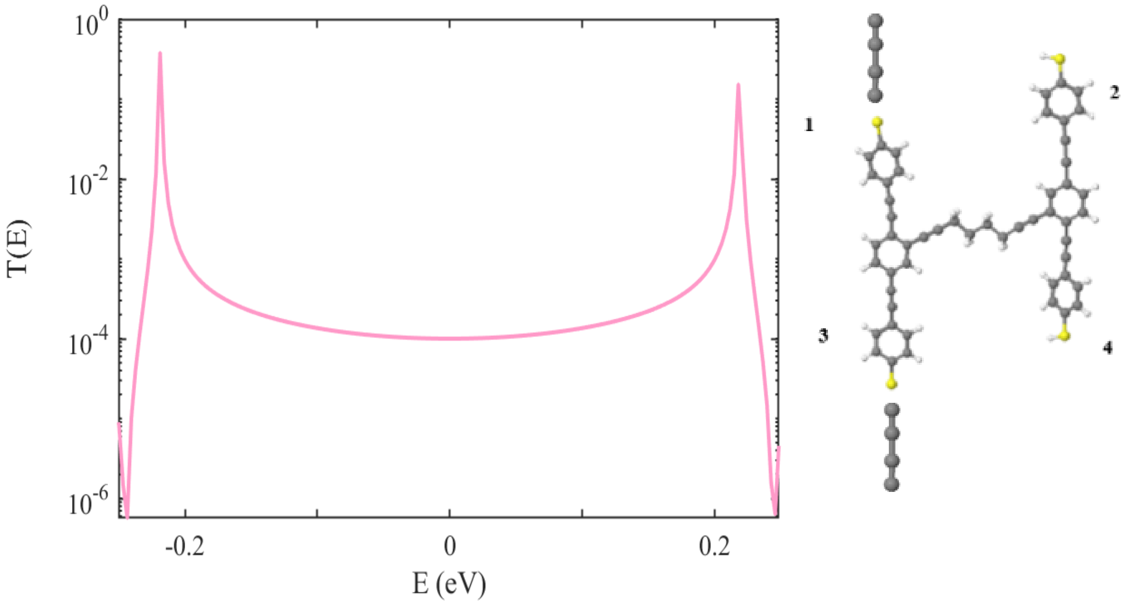

Figure 4. 16: Right panel: Schematic illustration of the 1D lead/C-**1**/1D lead junctions in (**1-3**) contact points. **Left panel:** Tight binding transmission coefficient $T(E)$ of 1D lead/C-**1**/1D lead junctions against electron energy E.

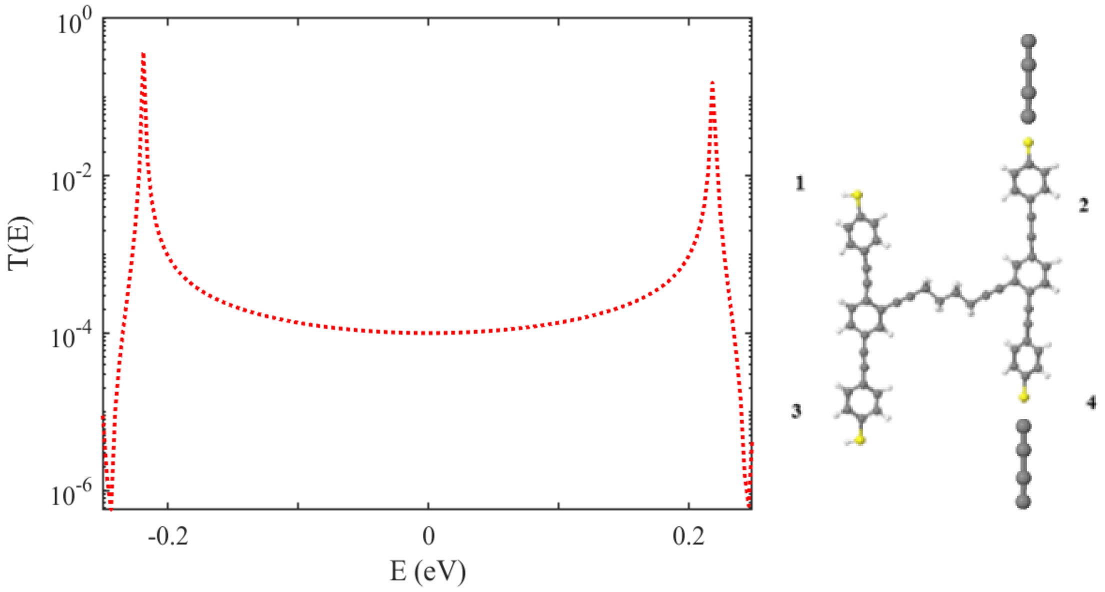

Figure 4. 17: Right panel: Schematic illustration of the 1D lead/C-**1**/1D lead junctions in (**2-4**) contact points. **Left panel:** Tight binding transmission coefficient $T(E)$ of 1D lead/C-**1**/1D lead junctions against electron energy E.

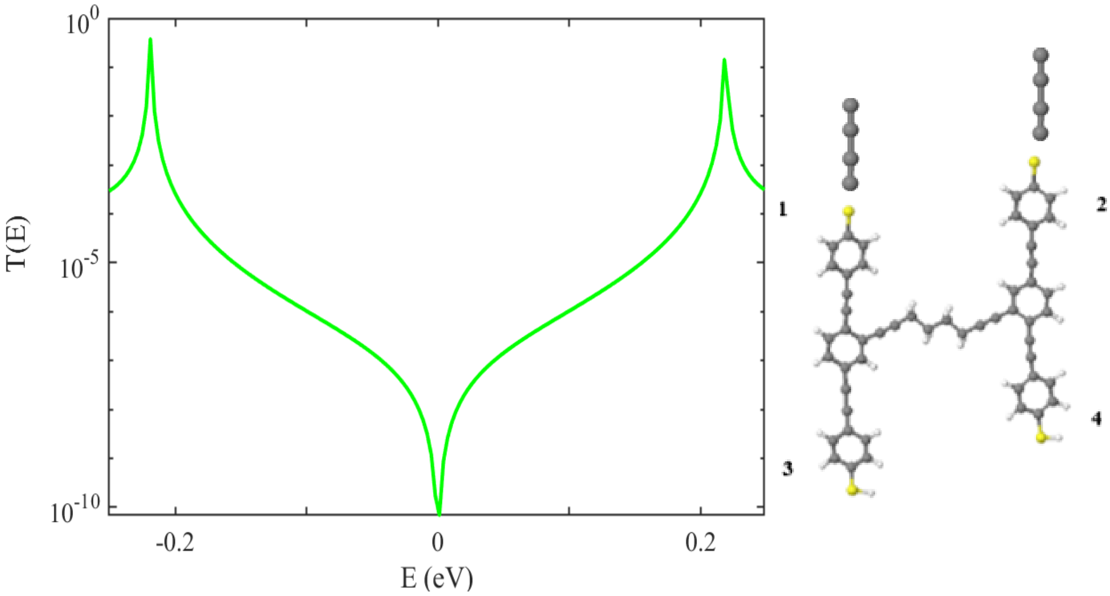

Figure 4. 18: Right panel: Schematic illustration of the 1D lead/C-**1**/1D lead junctions in (**1-2**) contact points. **Left panel:** Tight binding transmission coefficient $T(E)$ of 1D lead/C-**1**/1D lead junctions against electron energy E.

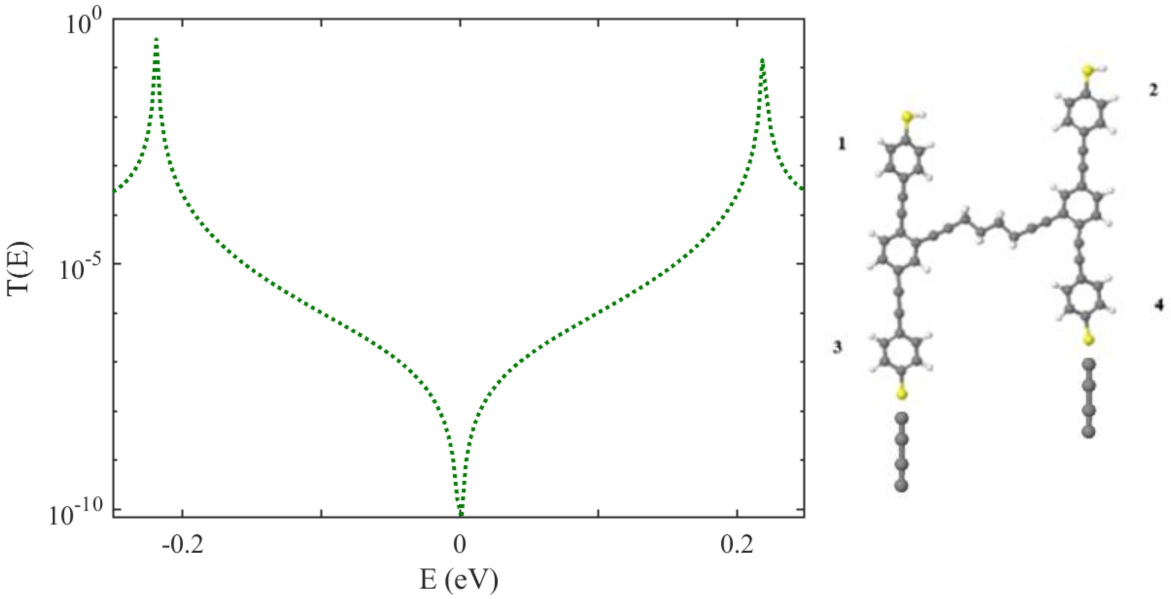

Figure 4. 19: Right panel: Schematic illustration of the 1D lead/C-**1**/1D lead junctions in (**3-4**) contact points. **Left panel:** Tight binding transmission coefficient $T(E)$ of 1D lead/C-**1**/1D lead junctions against electron energy E.

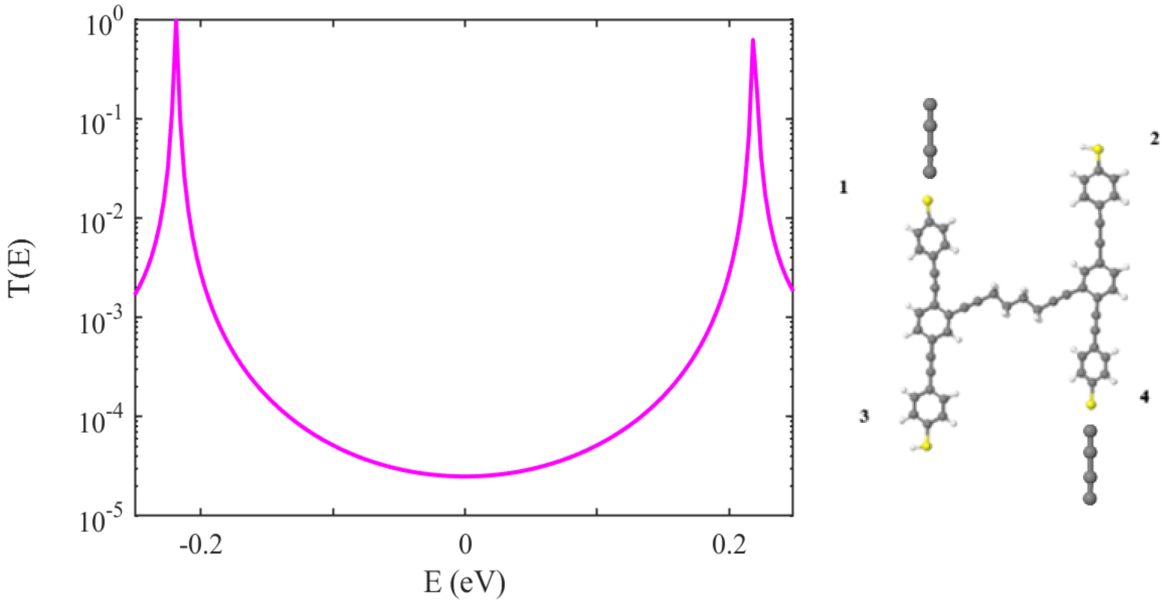

Figure 4. 20: Right panel: Schematic illustration of the 1D lead/C-**1**/1D lead junctions in (**1-4**) contact points. **Left panel:** Tight binding transmission coefficient $T(E)$of 1D lead/C-**1**/1D lead junctions against electron energy E.

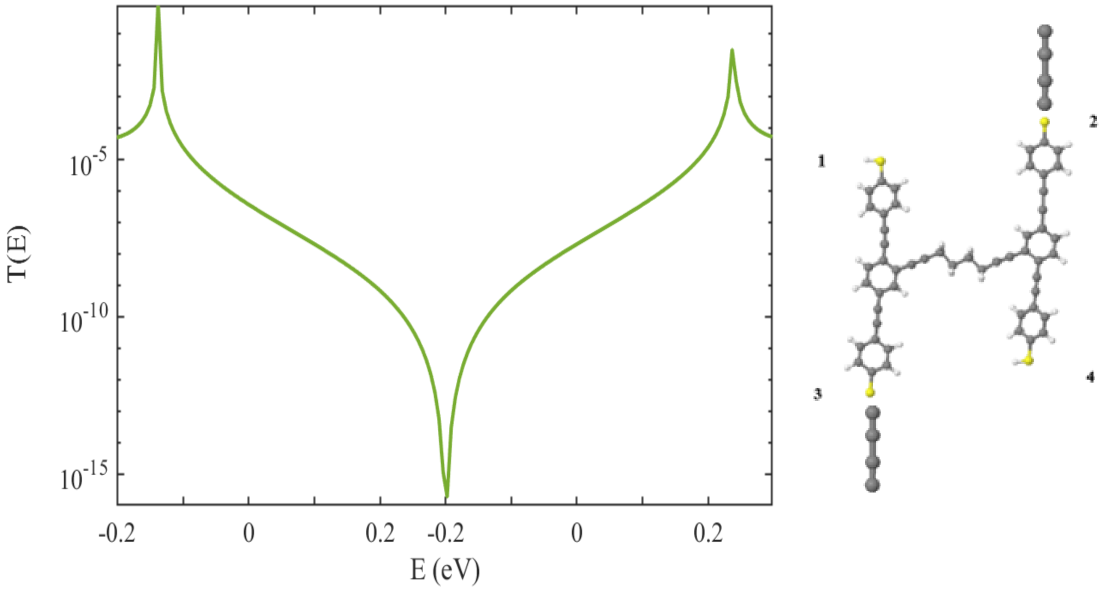

Figure 4. 21: Right panel: Schematic illustration of the 1D lead/C-**1**/1D lead junctions in (**2-3**) contact points. **Left panel:** Tight binding transmission coefficient $T(E)$ of 1D lead/C-**1**/1D lead junctions against electron energy E.

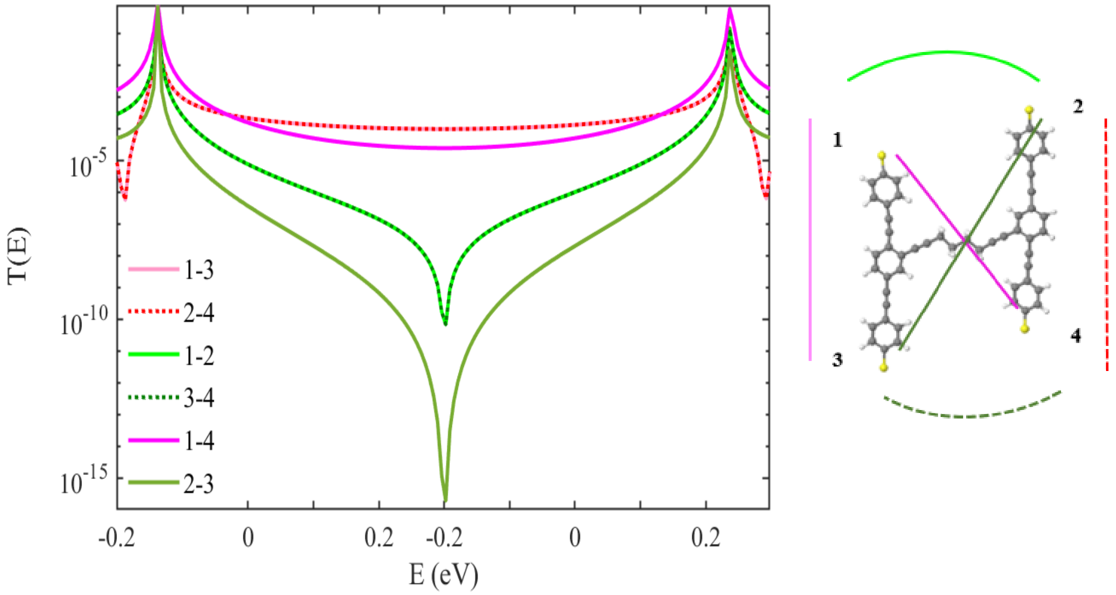

Figure 4. 22: Right panel: Schematic illustration of the 1D lead/C-**1**/1D lead junctions in six contact points: (**1-3**), (**2-4**), (**1-2**), (**3-4**), (**1-4**), and (**2-3**). **Left panel:** Tight binding transmission coefficient $T(E)$ of 1D lead/C-**1**/1D lead junctions against electron energy E.

4.9.2 TBM transport simulation for cross-linked (2)

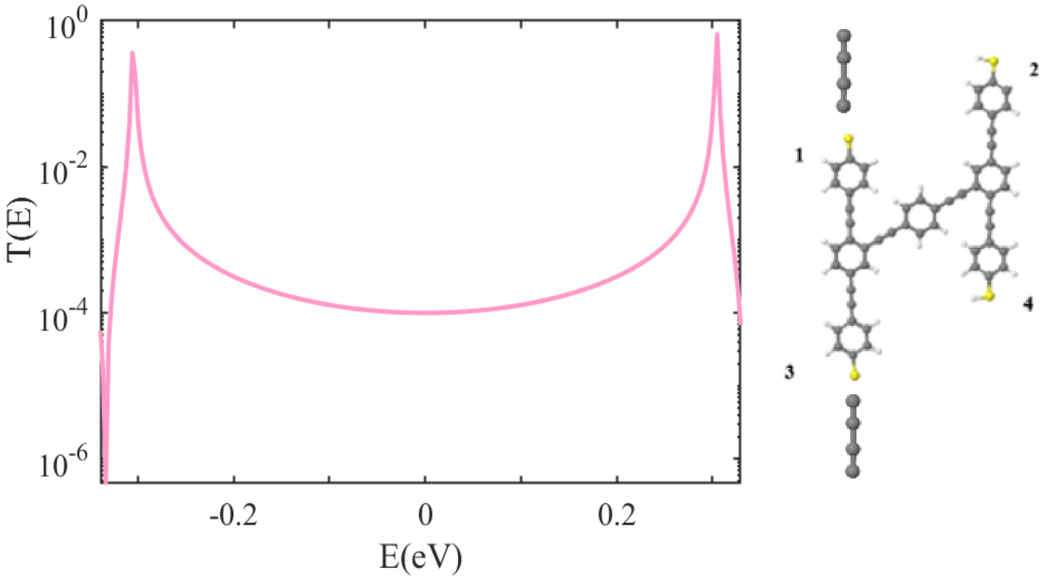

Figure 4. 23: Right panel: Schematic illustration of the 1D lead/C-**2**/1D lead junctions in (**1-3**) contact points. **Left panel:** Tight binding transmission coefficient $T(E)$ of 1D lead/C-**2**/1D lead junctions against electron energy E.

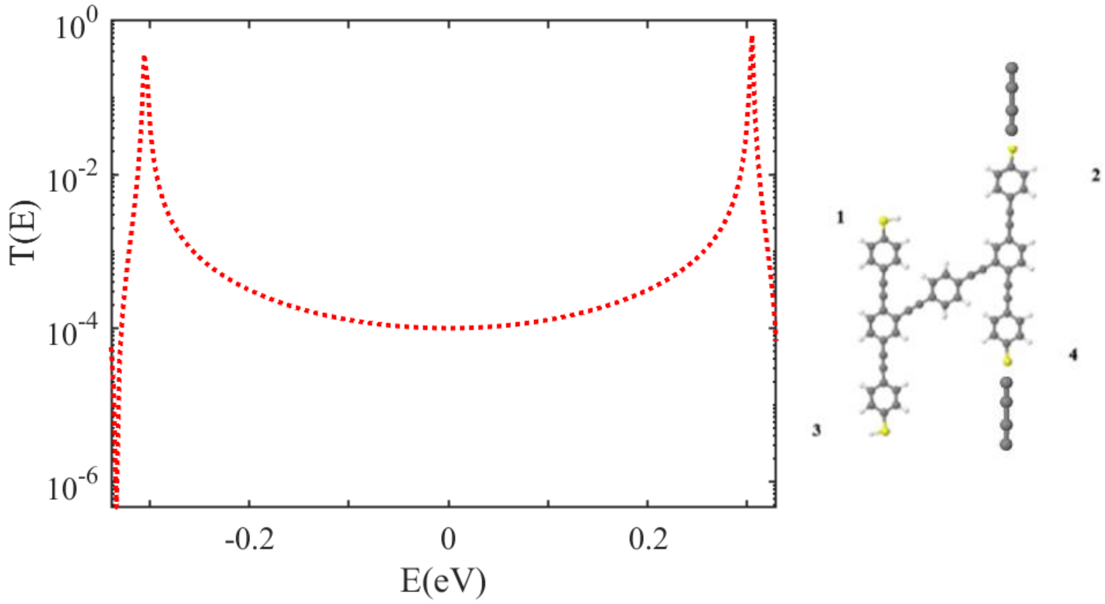

Figure 4. 24: Right panel: Schematic illustration of the 1D lead/C-**2**/1D lead junctions in (**2-4**) contact points. **Left panel:** Tight binding transmission coefficient $T(E)$of 1D lead/C-**2**/1D lead junctions against electron energy E.

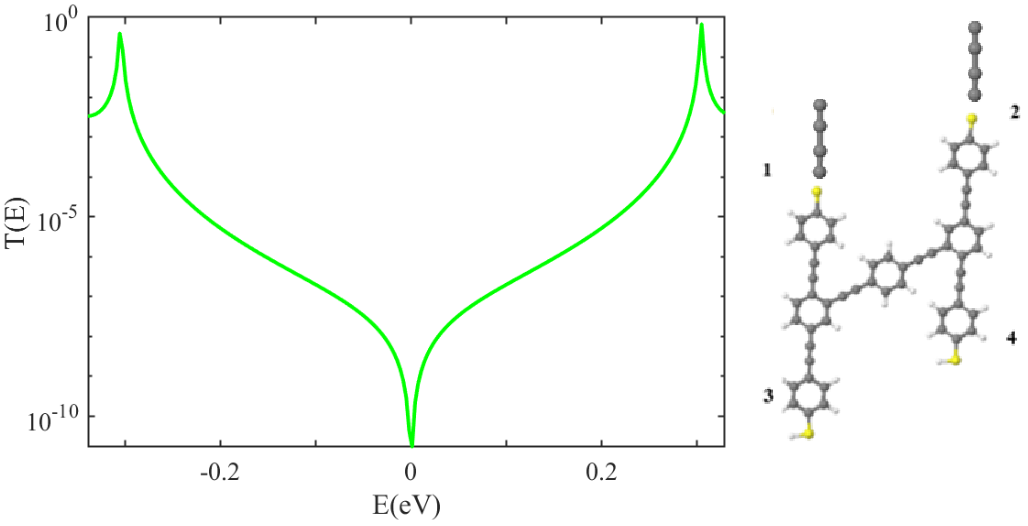

Figure 4. 25: Right panel: Schematic illustration of the 1D lead/C-**2**/1D lead junctions in (**1-2**) contact points. **Left panel:** Tight binding transmission coefficient $T(E)$ of 1D lead/C-**2**/1D lead junctions against electron energy E.

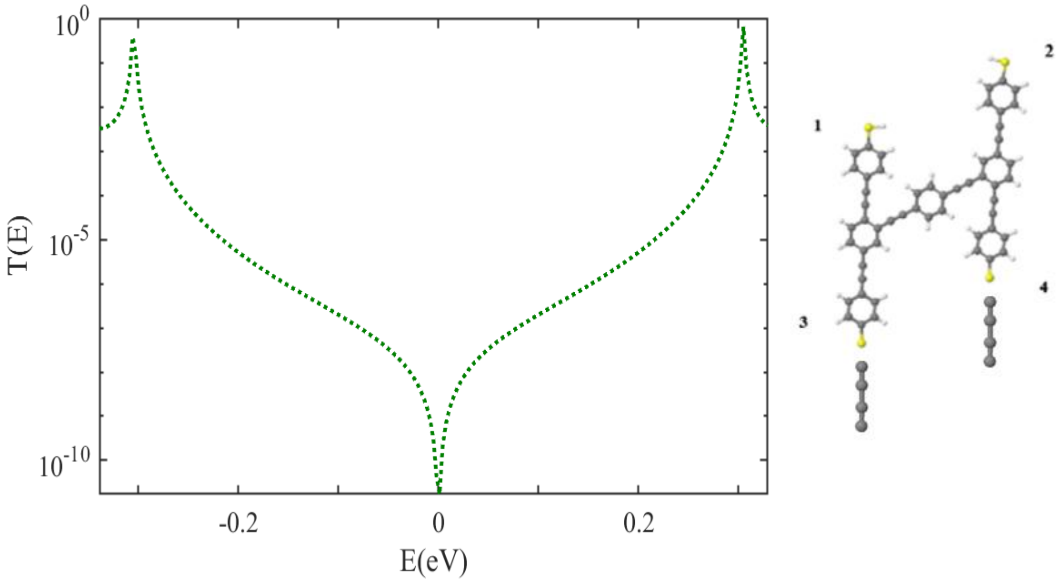

Figure 4. 26: Right panel: Schematic illustration of the 1D lead/C-**2**/1D lead junctions in (**3-4**) contact points. **Left panel:** Tight binding transmission coefficient $T(E)$ of 1D lead/C-**2**/1D lead junctions against electron energy E.

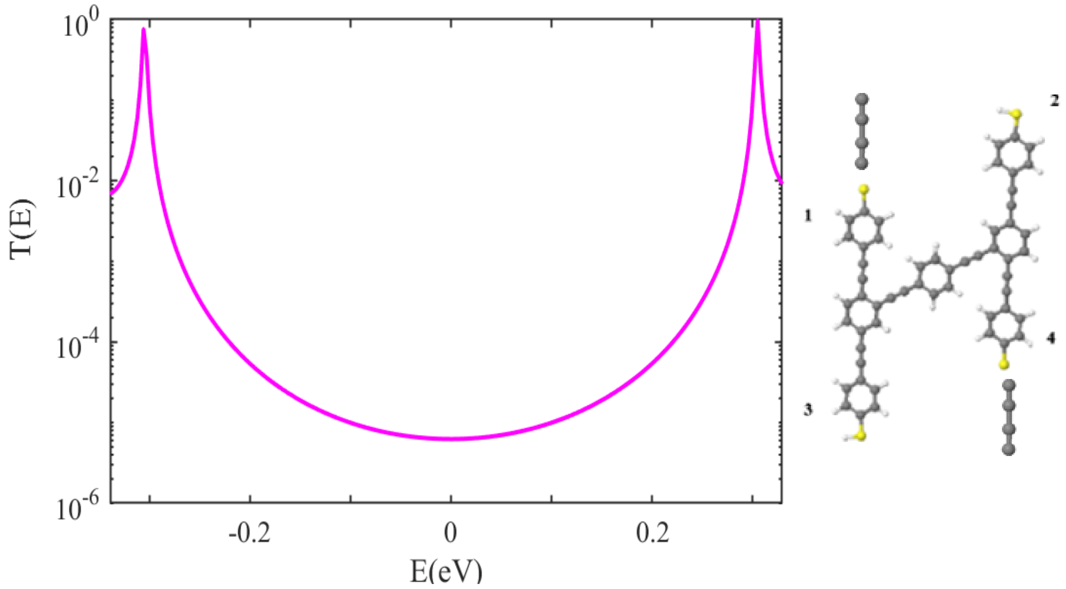

Figure 4. 27: Right panel: Schematic illustration of the 1D lead/C-**2**/1D lead junctions in (**1-4**) contact points. **Left panel:** Tight binding transmission coefficient $T(E)$ of 1D lead/C-**2**/1D lead junctions against electron energy E.

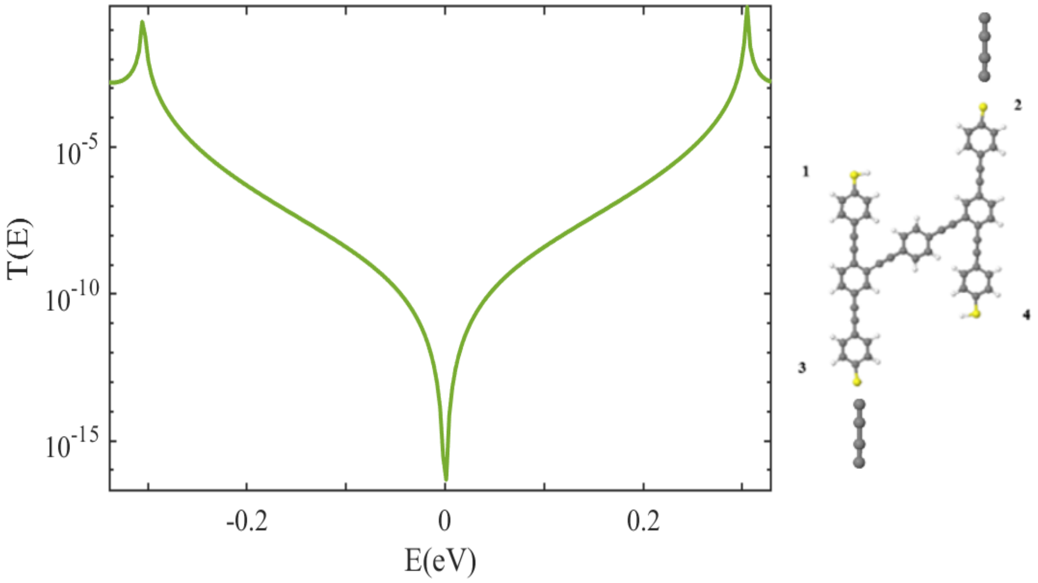

Figure 4. 28: Right panel: Schematic illustration of the 1D lead/C-**2**/1D lead junctions in (**2-3**) contact points. **Left panel:** Tight binding transmission coefficient $T(E)$ of 1D lead/C-**2**/1D lead junctions against electron energy E.

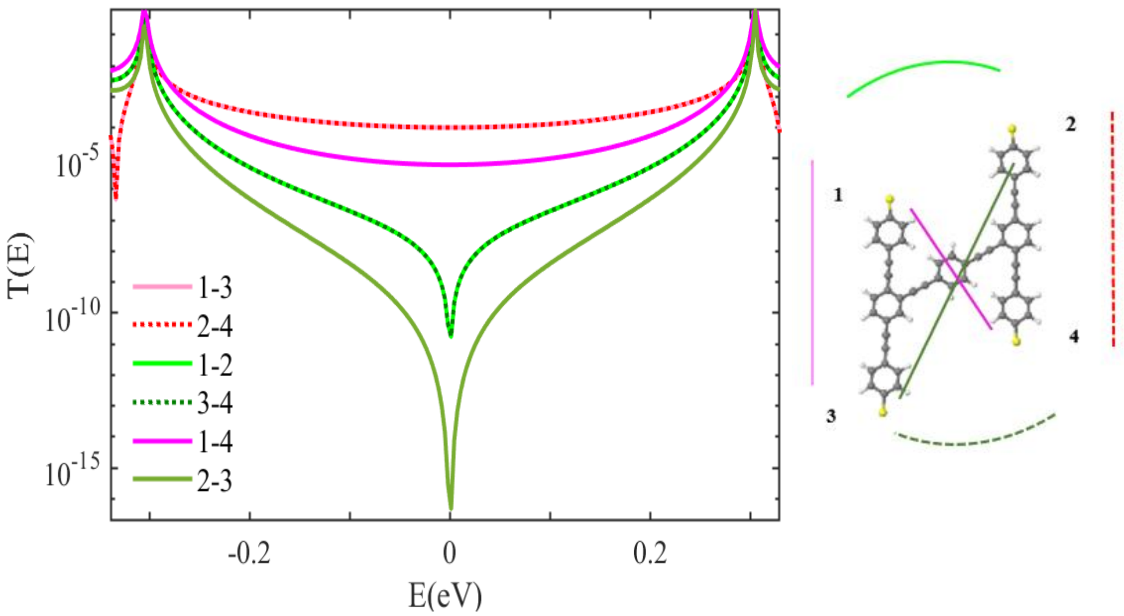

Figure 4. 29: Right panel: Schematic illustration of the 1D lead/C-**2**/1D lead junctions in six contact points: (**1**-**3**), (**2**-**4**), (**1**-**2**), (**3**-**4**), (**1**-**4**), and (**2**-**3**). contact points. **Left panel:** Tight binding transmission coefficient $T(E)$ of 1D lead/C-**2**/1D lead junctions against electron energy E.

Table 4. 2 demonstrates the transmission functions for the studied molecules, which are cross-linked **1** and **2** (C-L**1** and C-L**2**), using TBM. The calculations were performed at the one-dimensional lead (1D), contact connected to the anchor across six points to determine whether the quantum interference is constructive CQI or distractive DQI.

Table 4. 2: TBM results for cross-linked **1** and **2**, in six different contact points (Note: C for constructive and D for destructive QI).

Cross-linked	Contact point	TBM results	Transmission Figures
C-L**1**	**1-3, 2-4** **1-2, 3-4** **1-4, 2-3**	C, C D, D C, D	Figure 4. 16-Figure 4. 17 Figure 4. 18-Figure 4. 19 Figure 4. 20-Figure 4. 21
C-L**2**	**1-3, 2-4** **1-2, 3-4** **1-4, 2-3**	C, C D, D C, D	Figure 4. 23-Figure 4. 24 Figure 4. 25-Figure 4. 26 Figure 4. 27-Figure 4. 28

4.10 DFT transport simulation in Au-Au junction

In the following transport calculations, the transmission coefficient curves $T(E)$ will be obtained using the Gollum transport code [41], which utilises the ground state Hamiltonian and the optimised geometry of each compound was obtained using the density functional theory DFT code, that to compute transport properties of a wide variety of nanostructures by employing theoretical models described in chapter 3[8]. The transmission coefficient $T(E)$ is computed, and I can calculate the zero-bias electrical conductance G using the Landauer formula (Chapter 3). The transmission coefficients $T(E)$ were calculated for the studied structures of C-L**1** and C-L**2** shown in **Figure 4. 14** and **Figure 4. 15**. The Fermi level is chosen to be $(E - E_F^{DFT} = 0eV)$ of the electrode for these twelve junctions. The transmission coefficients $T(E)$ for cross-linked **1** are shown in **Figure 4. 30** to **Figure 4. 35**. While **Figure 4. 37** to **Figure 4. 42** are showing the transmission coefficients $T(E)$ for cross-linked **2**.

Changing the path of electrons between source to drain leads to a change in the transmission coefficient $T(E)$ from a constrictive to a destructive curve, as in the present study. **Figure 4. 36** and **Figure 4. 43** show zero bias transmission coefficient $T(E)$, obtained from density functional theory, for six different electrode connectivities to dimers C-L**1** and C-L**2**. These figures display six transmission coefficients; three of them show CQI. On the other hand, the other three show DQI. In this section, I shall calculate the transport in gold junctions as follows:

4.10.1 Transport simulation in Au-Au junction for cross-linked (1)

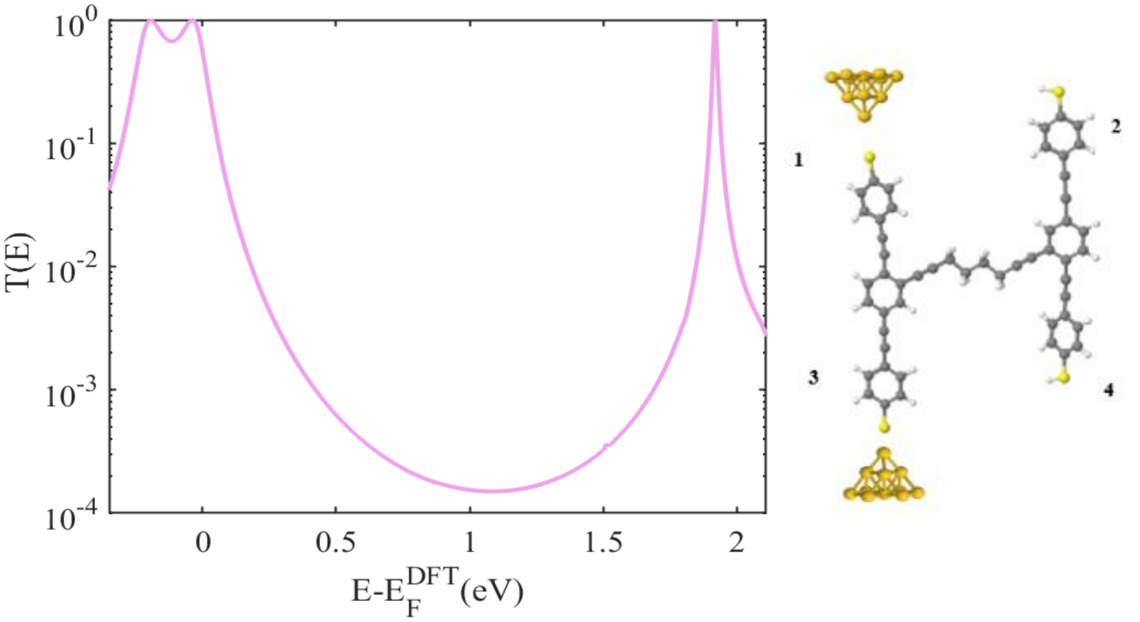

Figure 4. 30: Right panel: Schematic illustration of the Au/C-L**1**/Au junctions in (**1-3**) contact points. **Left panel:** Transmission coefficient $T(E)$ of Au/C-L**1**/Au junctions against electron energy E.

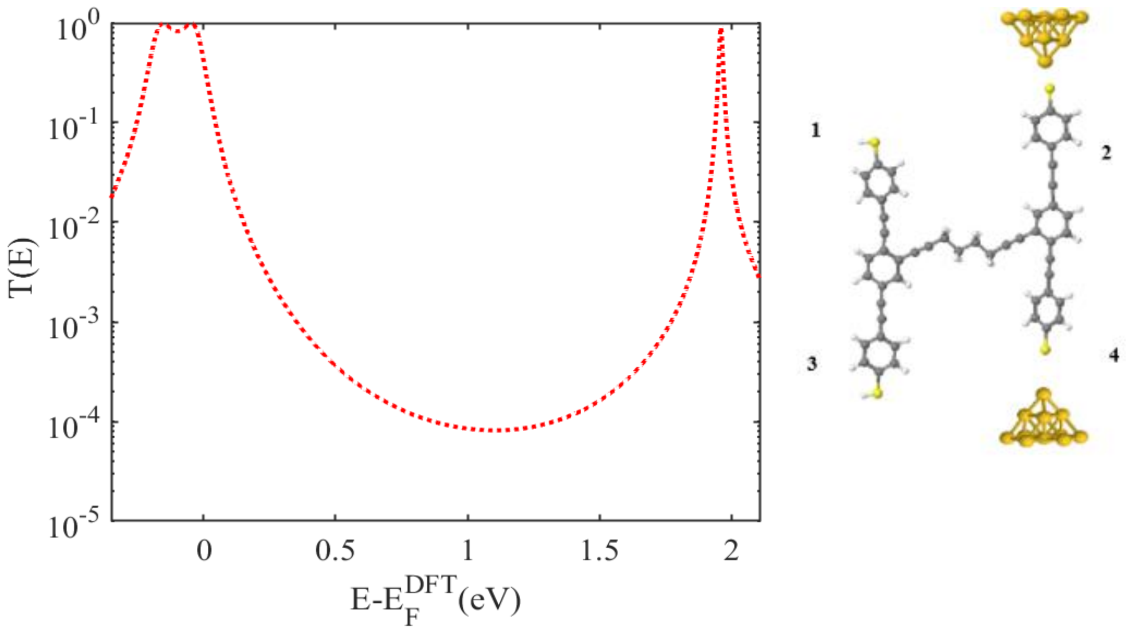

Figure 4. 31: Right panel: Schematic illustration of the Au/C-L**1**/Au junctions in (**2-4**) contact points. **Left panel:** Transmission coefficient $T(E)$ of Au/C-L**1**/Au junctions against electron energy E.

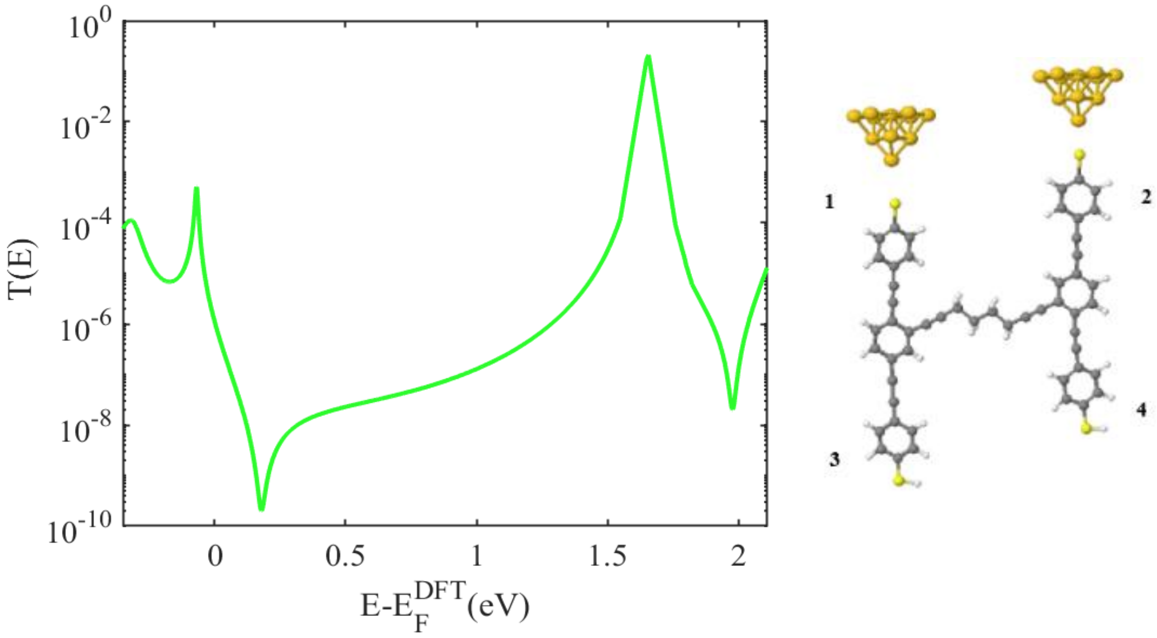

Figure 4. 32: Right panel: Schematic illustration of the Au/C-L**1**/Au junctions in (**1-2**) contact points. **Left panel:** Transmission coefficient $T(E)$ of Au/C-L1/Au junctions against electron energy E.

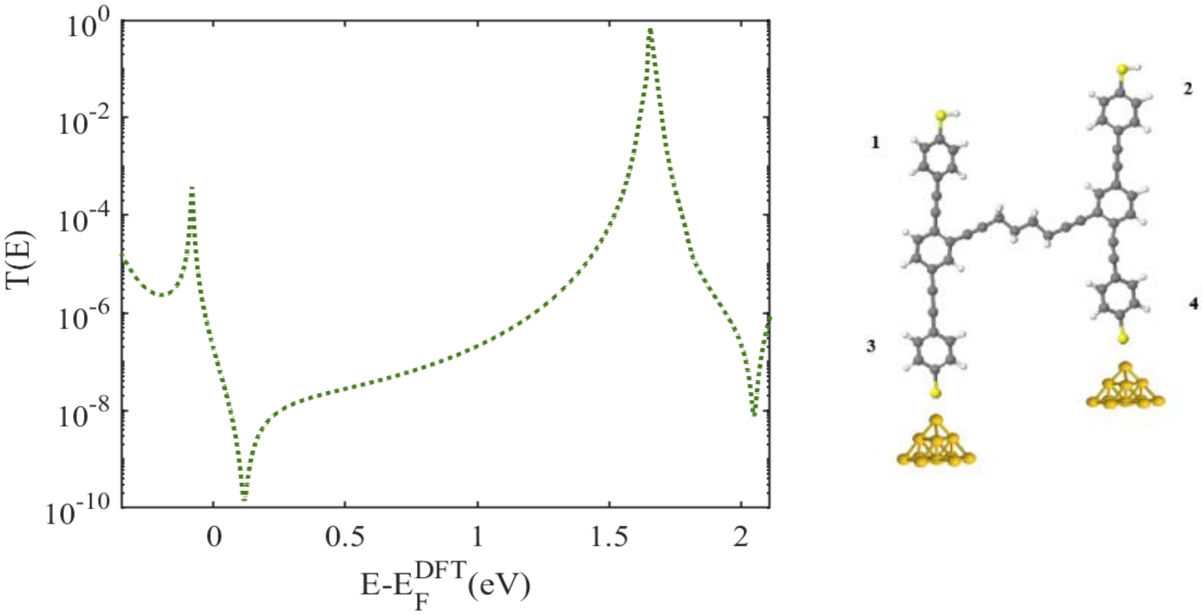

Figure 4. 33: Right panel: Schematic illustration of the Au/C-L**1**/Au junctions in (**3-4**) contact points. **Left panel:** Transmission coefficient $T(E)$ of Au/C-L**1**/Au junctions against electron energy E.

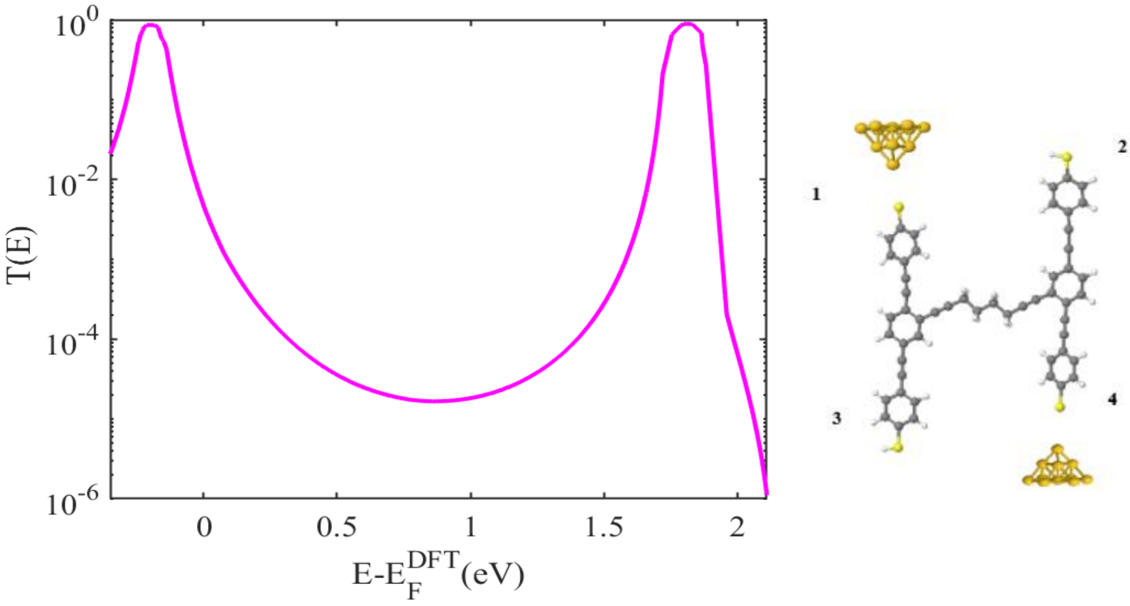

Figure 4. 34: Right panel: Schematic illustration of the Au/C-L**1**/Au junctions in (**1-4**) contact points. **Left panel:** Transmission coefficient $T(E)$ of Au/C-L**1**/Au junctions against electron energy E.

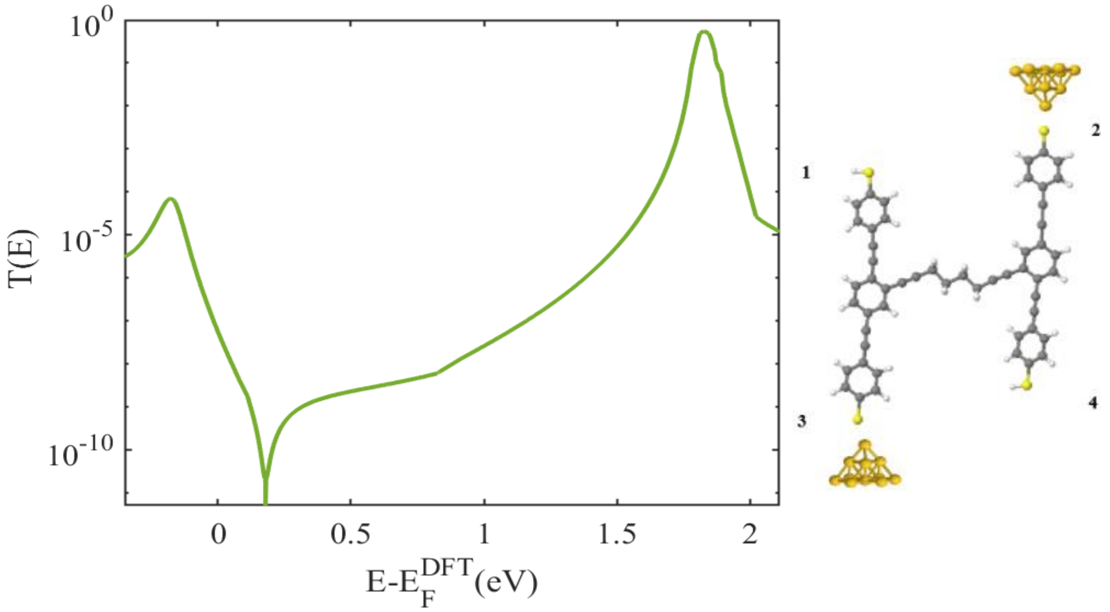

Figure 4. 35: Right panel: Schematic illustration of the Au/C-L**1**/Au junctions in (**2-3**) contact points. **Left panel:** Transmission coefficient $T(E)$ of Au/C-L**1**/Au junctions against electron energy E.

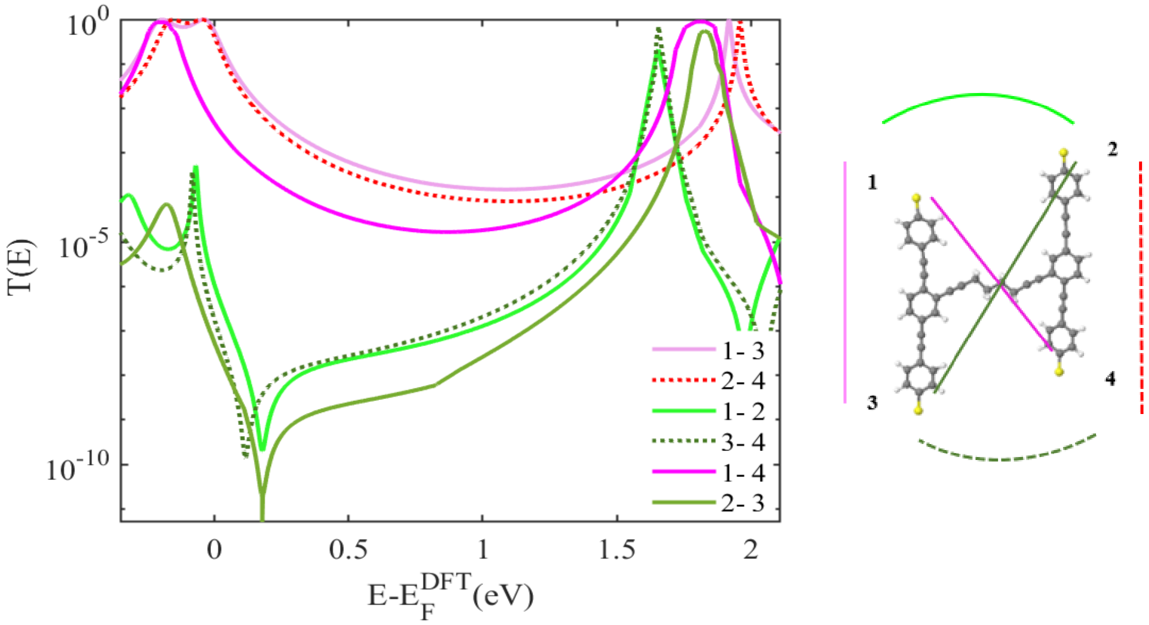

Figure 4. 36: Right panel: Schematic illustration of the Au/C-L**1**/Au junctions in in six contact points: (**1-3**), (**2-4**), (**1-2**), (**3-4**), (**1-4**), and (**2-3**). **Left panel:** Transmission coefficients $T(E)$ of Au/C-L**1**/Au junctions against electron energy E.

4.10.2 DFT transport simulation in Au-Au junction for cross-linked (2)

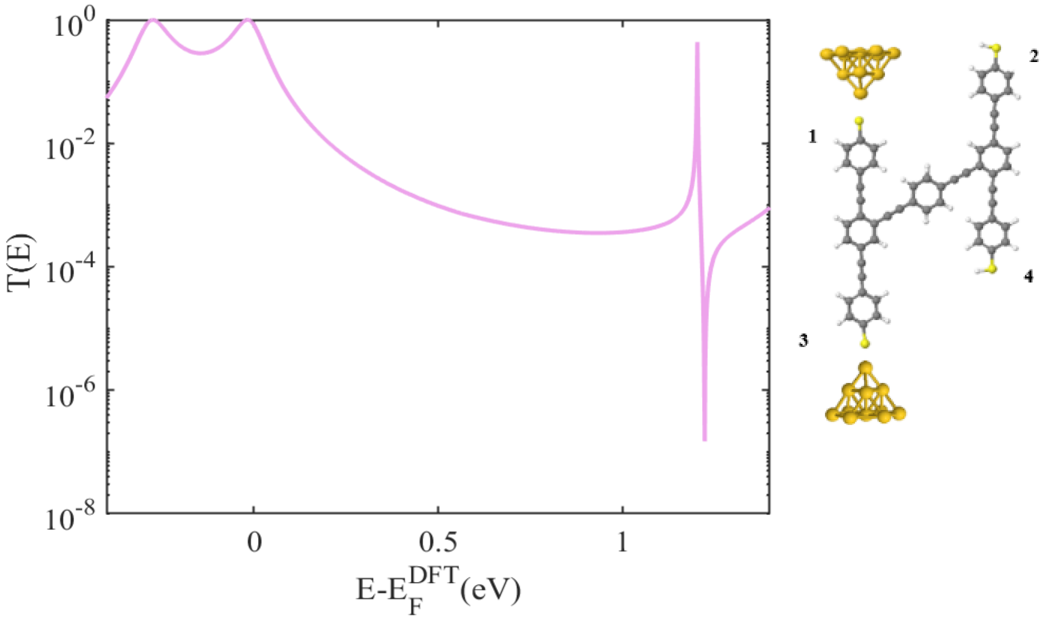

Figure 4. 37: Right panel: Schematic illustration of the Au/C-L**2**/Au junctions in (**1**-**3**) contact points. **Left panel:** Transmission coefficient $T(E)$ of Au/C-L**2**/Au junctions against electron energy E.

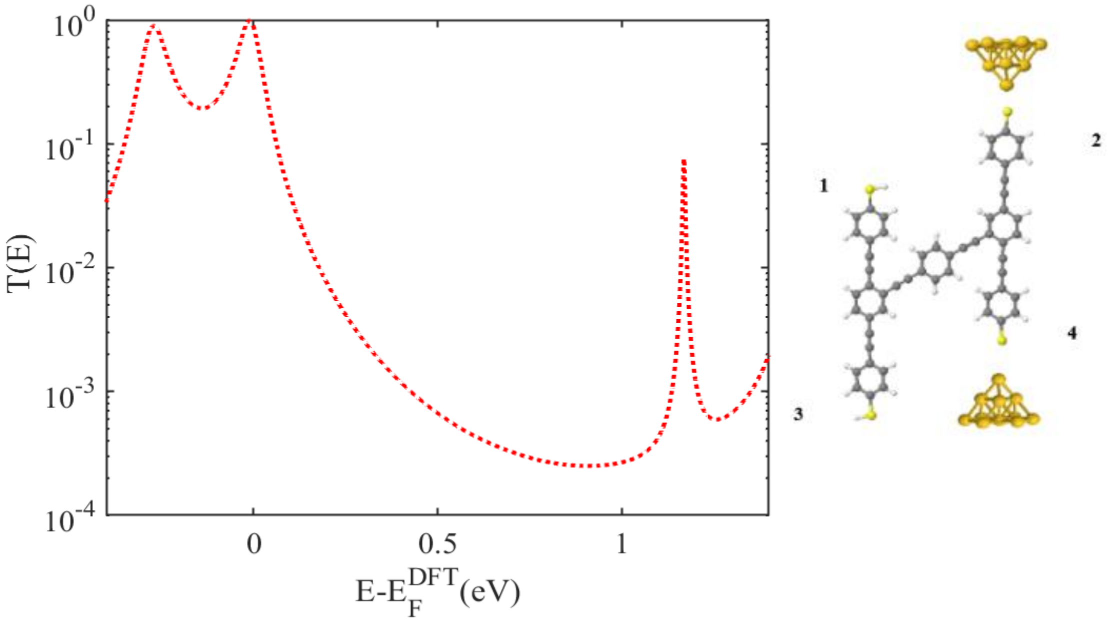

Figure 4. 38: Right panel: Schematic illustration of the Au/C-L**2**/Au junctions in (**2**-**4**) contact points. **Left panel**: Transmission coefficient $T(E)$ of Au/C-L**2**/Au junctions against electron energy E.

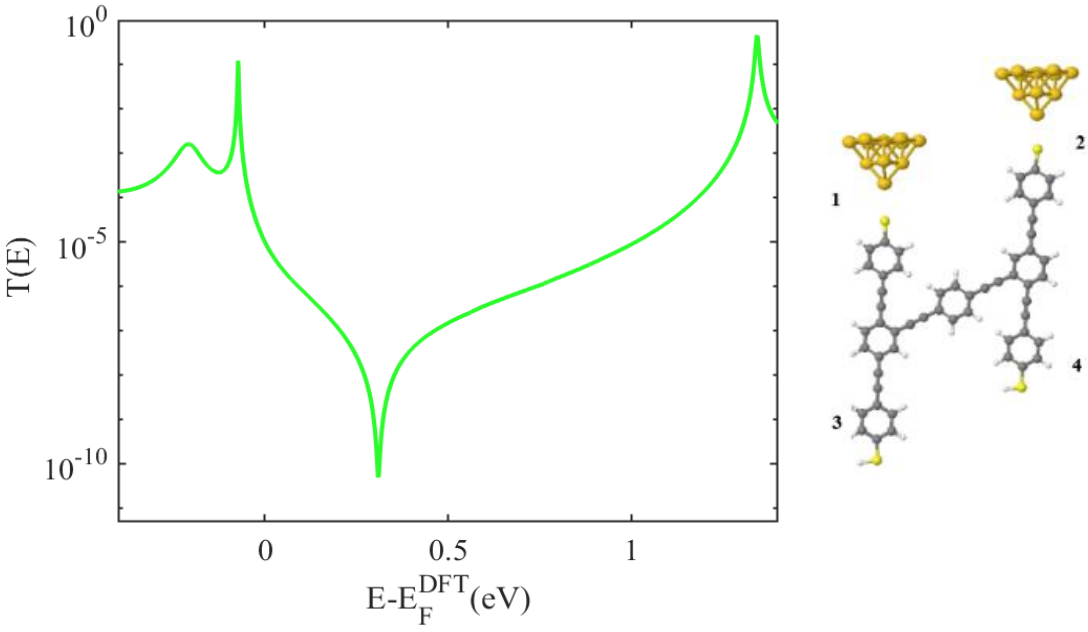

Figure 4. 39: Right panel: Schematic illustration of the Au/C-L**2**/Au junctions in (**1-2**) contact points. **Left panel**: Transmission coefficient $T(E)$ of Au/C-L**2**/Au junctions against electron energy E.

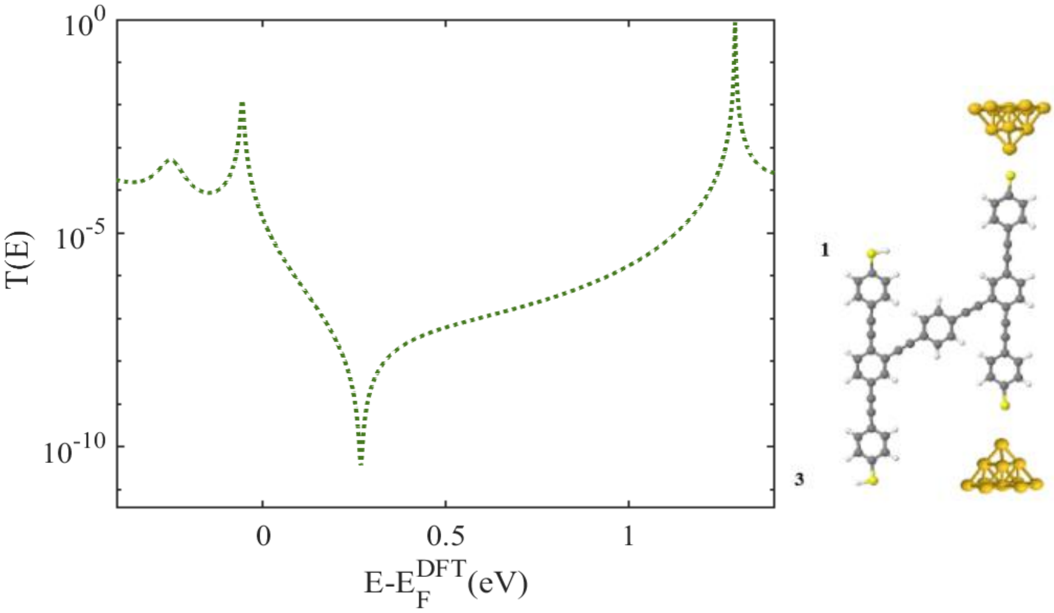

Figure 4. 40: Right panel: Schematic illustration of the Au/C-L**2**/Au junctions in (**3-4**) contact points. **Left panel**: Transmission coefficient $T(E)$ of Au/C-L**2**/Au junctions against electron energy E.

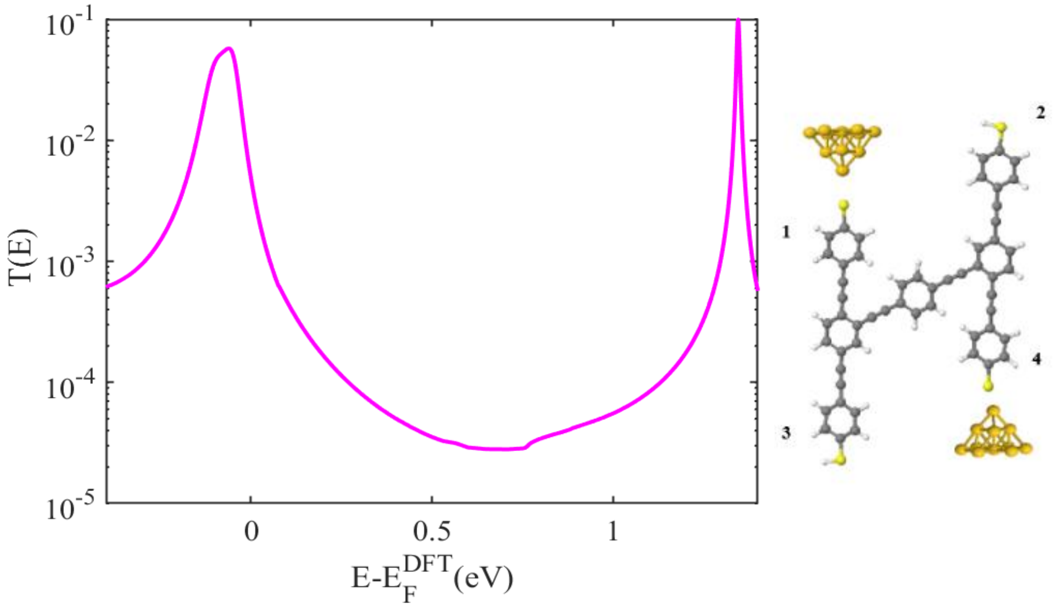

Figure 4. 41: Right panel: Schematic illustration of the Au/C-L**2**/Au junctions in (**1**-**4**) contact points. **Left panel:** Transmission coefficient $T(E)$ of Au/C-L**2**/Au junctions against electron energy E.

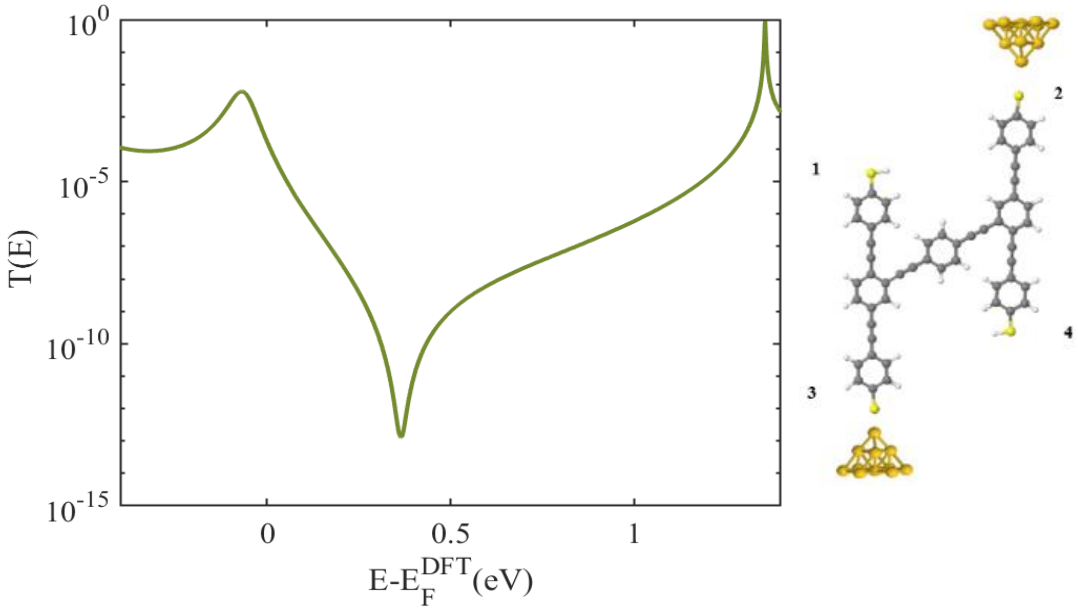

Figure 4. 42: Right panel: Schematic illustration of the Au/C-L**2**/Au junctions in (**2**-**3**) contact points. **Left panel:** Transmission coefficient $T(E)$ of Au/C-L**2**/Au junctions against electron energy E.

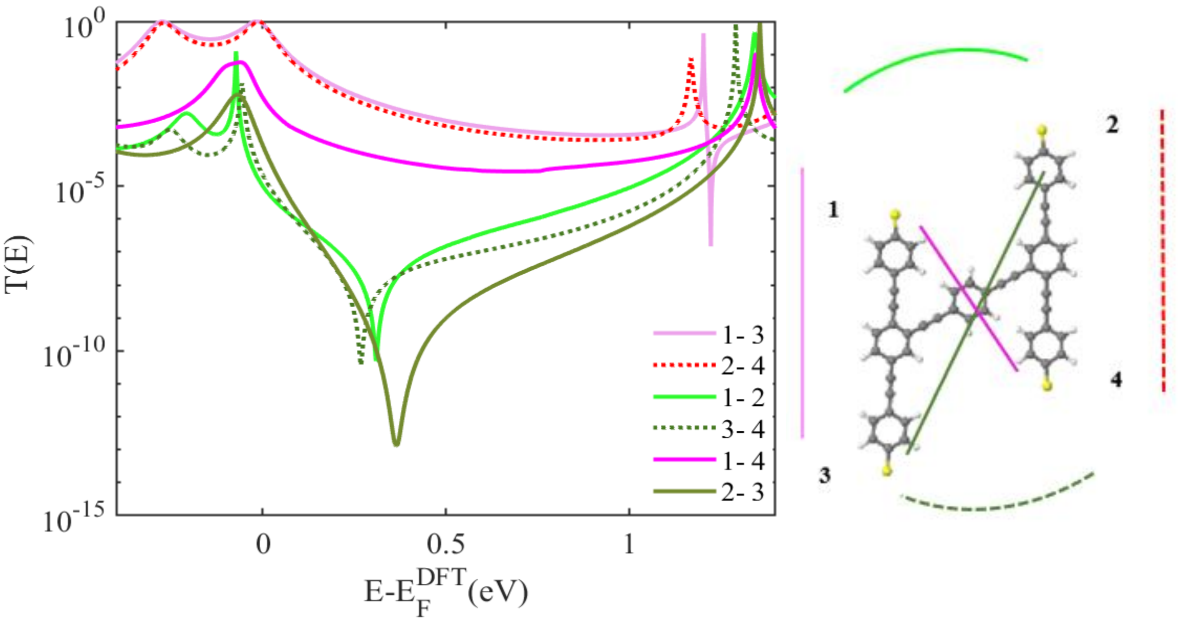

Figure 4. 43: Right panel: Schematic illustration of the Au/C-L**2**/Au junctions in in six contact points: (**1-3**), (**2-4**), (**1-2**), (**3-4**), (**1-4**), and (**2-3**). **Left panel:** Transmission coefficients $T(E)$ of Au/C-L**2**/Au junctions against electron energy E.

Table 4. 3 illustrates the transmission functions for the studied molecules, which are cross-linked **1** and cross-linked **2** (C-L**1** and C-L**2**). The calculations were conducted at the lead contact linked to the anchor across six points to determine whether the quantum interference is constructive CQI or distractive DQI. As shown below, this DFT results agree partially with the orbital product rule and align well with the TBM results.

Table 4. 3: DFT results for cross-linked **1** and **2**, in six different contact points (Note: C for constructive and D for destructive QI).

Cross-linked	Contact point	DFT result	Transmission Figures
C-L**1**	**1-3, 2-4** **1-2, 3-4** **1-4, 2-3**	C, C D, D C, D	Figure 4. 30-Figure 4. 31 Figure 4. 32-Figure 4. 33 Figure 4. 34-Figure 4. 35
C-L**2**	**1-3, 2-4** **1-2, 3-4** **1-4, 2-3**	C, C D, D C, D	Figure 4. 37-Figure 4. 38 Figure 4. 39-Figure 4. 40 Figure 4. 41-Figure 4. 42

4.11 TBM versus DFT

To compare the results of TBM, I performed DFT transport simulations for the C-L**1** and C-L**2** dimers, each with six different pairs of electrode contacts. TBM curves are in qualitative agreement with the DFT transmission coefficients $T(E)$ of the C-L**1** and C-L**2**, as shown in **Figure 4. 44** and **Figure 4. 45**. Both TBM and DFT approaches illustrate that in the presence of the **1-3**,**2-4** and **1-4** connectivities, there is no signature of a DQI (i.e., dip). However, the identical dimers with **1-2**, **3-4** and **2-3** conductive switch from CQI to DQI regardless of the bridging linker chemical structure. The main qualitative difference between the DFT results and the TBM results arises from the fact that the tight-binding model is a nearest-neighbour bipartite lattice, in which atoms can be labelled, such that odd-numbered atoms interact with even-numbered atoms only and vice versa. This chiral symmetry guarantees that the transmission coefficient is a symmetric function of the electron energy E.

In summary, using density functional theory and a tight-binding model, I have demonstrated that the appearance of destructive or constructive quantum interference in cross-linked OPE-based dimers is independent of the nature of the molecular cross-link. Instead, the nature of the interference is controlled by the connectivity to external electrodes. It is determined by the presence or otherwise of *meta*-connected phenyl rings on the transport path. This is expected to be an essential design feature when synthesising molecules with cross-links of different stiffnesses because the stiffness and phonon transport properties can be tuned whilst maintaining CQI or DQI.

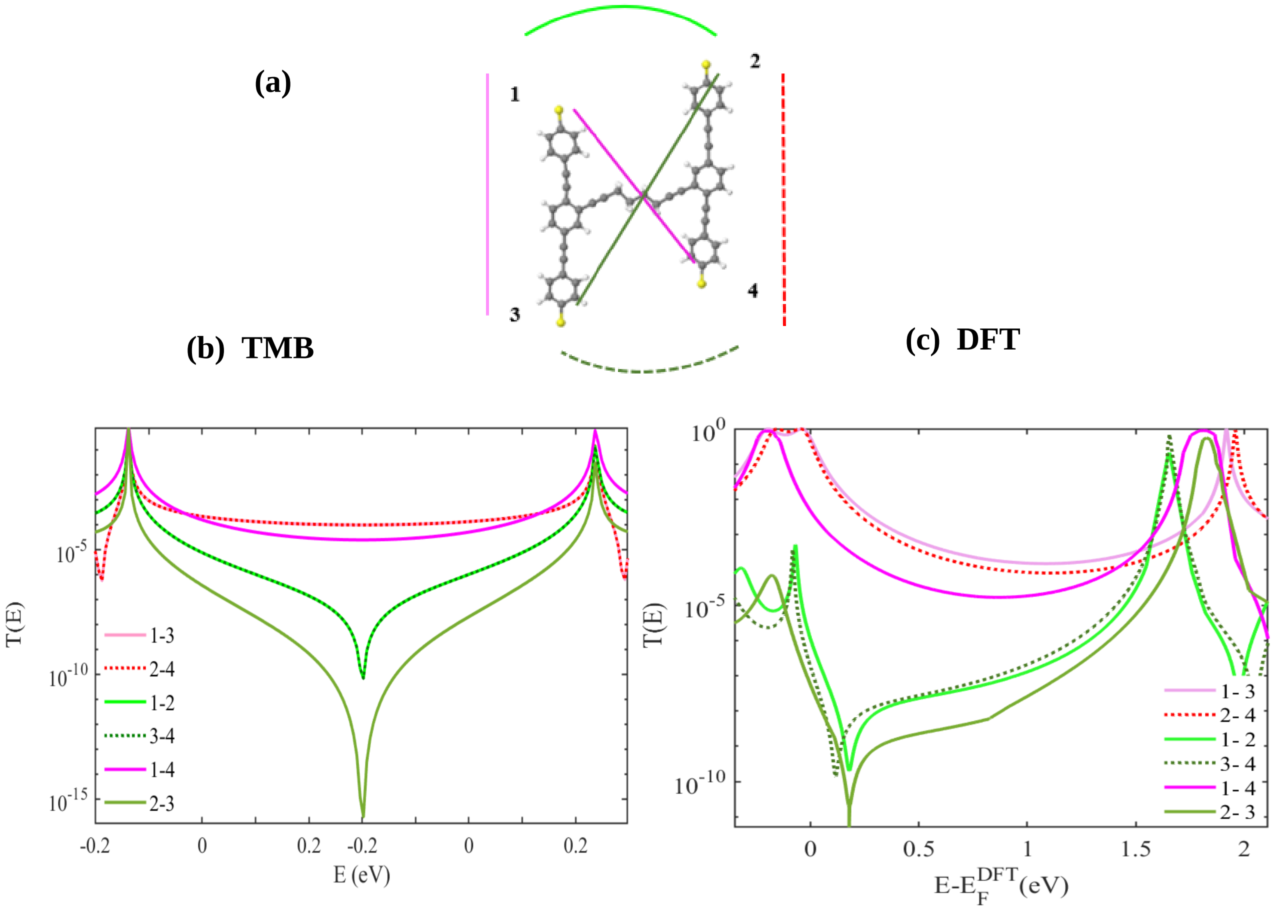

Figure 4. 44: (a): Schematic illustration of the Au/C-L**1**/Au junctions in in six contact points: (**1-3**), (**2-4**), (**1-2**), (**3-4**), (**1-4**), and (**2-3**). **(b):** Tight binding transmission coefficients $T(E)$ of 1D lead/C-**1**/1D lead. **(c):** Transmission coefficients $T(E)$ by DFT of Au/C-L**1**/Au junctions against electron energy E.

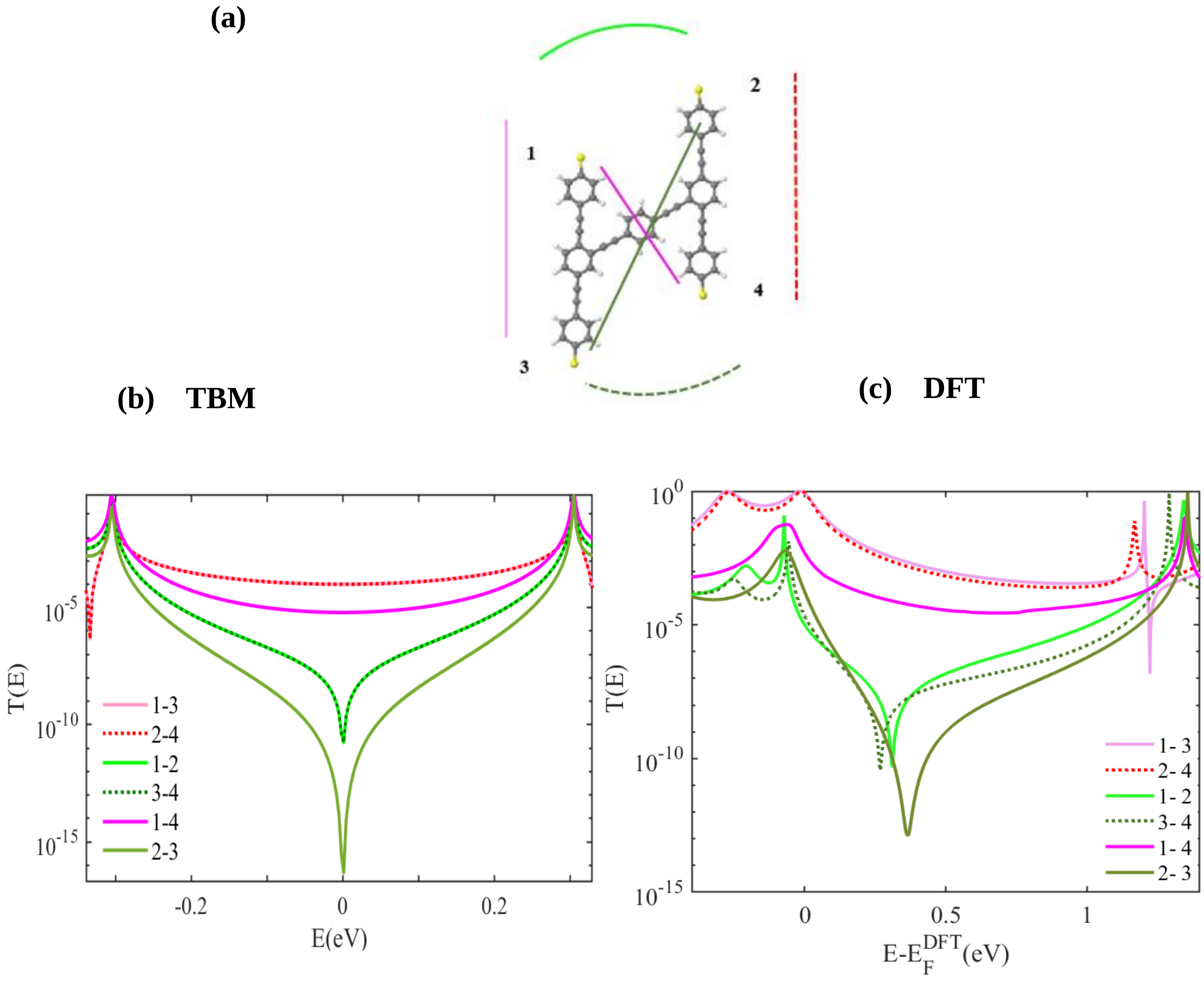

Figure 4. 45: (a): Schematic illustration of the Au/C-L**2**/Au junctions in in six contact points: (**1-3**), (**2-4**), (**1-2**), (**3-4**), (**1-4**), and (**2-3**). **(b):** Tight binding transmission coefficients $T(E)$ of 1D lead/C-**2**/1D lead. **(c):** Transmission coefficients $T(E)$ by DFT of Au/C-L**2**/Au junctions against electron energy E.

4.12 Checking OPR predictions by both DFT and TBM

Table 4. 4: Orbital product rule predictions for cross-linked **1** and **2**, against the DFT and TBM results (Note: ✓: OPR and DFT agree while x: OPR and DFT don't agree).

cross-linked	Contact points	OPR prediction	DFT & TBM	OPR and DFT -TBM agreement	wavefunction plot Figures
C-L**1**	**1-3, 2-4** **1-2, 3-4** **1-4, 2-3**	C, C C, C D, D	C, C D, D C, D	✓, ✓ x, x x, ✓	Figure 4. 4 (a) Figure 4. 4 (a) Figure 4. 4 (a)
C-L**2**	**1-3, 2-4** **1-2, 3-4** **1-4, 2-3**	C, C C, C D, D	C, C D, D C, D	✓, ✓ x, x x, ✓	Figure 4. 5 (a) Figure 4. 5 (a) Figure 4. 5 (a)

Based on the results presented in **Table 4. 2** and **Table 4. 3**, the findings indicate a complete (100%) agreement between the tight-binding model calculations and the density functional theory results, demonstrating the reliability and accuracy of the TBM in describing the system. However, the agreement with the product rule is only partial, at 50%, as shown in **Table 4. 4**. This discrepancy suggests that while the TBM effectively captures the electronic structure and behaviour predicted by DFT, it may not fully align with the simplifications or assumptions inherent in the product rule. These dimers clearly display a degeneracies in both their HOMOs and LUIMOs levels. For example, in the case of C-L**1,** $E_{HOMO} = -4.32$ and $E_{HOMO-1} = -4.33\ eV$, $E_{LUMO} = -2.21$ and $E_{LUMO+1} = -2.20\ eV$ as shown in **Figure 4. 4** and in the case of C-L**2,** $E_{HOMO} = -4.32$ and $E_{HOMO-1} = -4.33\ eV$, $E_{LUMO} = -2.24$ and $E_{LUMO+1} = -2.22\ eV$ as shown in **Figure 4. 5**.

4.13 Seebeck coefficient $S(E_F)$

The measurement of the Seebeck coefficient $S(E_F)$ in molecular junctions offers complementary information to conductance measurements and is becoming essential for understanding transport processes at the nanoscale. In this section, the thermoelectric properties of the molecules discussed in section (3.7), cross-linked **1** (C-L**1**) and cross-linked **2** (C-L**2**), are examined theoretically.

4.13.1 Thermopower calculations

In the previse section, the electronic transmission coefficient $T(E)$ function for the cross-linked junctions was computed. In the subsequent step, Seebeck coefficients $S(E_F)$ will be calculated as described in Chapter 3. To calculate the thermopower of the studied molecular junctions, it is helpful to introduce the non-normalised probability distribution $P(E)$ defined by

$$P(E) = -T(E)\frac{df(E)}{dE} \tag{4. 5}$$

where $f(E)$ represents the Fermi-Dirac distribution function and $T(E)$ represents the transmission coefficients and whose moments L_i are denoted as follows

$$L_i = \int dEP(E)(E - E_F)^i \tag{4. 6}$$

where E_F is Fermi energy. The Seebeck coefficient, $S(E_F)$, is then given by

$$S(T) = -\frac{1}{eT}\frac{L_1}{L_0} \tag{4. 7}$$

where e represents the magnitude of the electronic charge. It is apparent that the Seebeck coefficient is proportional to the slope of the logarithm of the transmission coefficient at the Fermi level. In general, depending on the sign of the slope of the transmission function at the Fermi energy E_F, the value of $S(E_F)$ can either be positive or negative. This arises from the nature of the charge carriers: a positive $S(E_F)$ indicates that holes dominate transport. At the same time, a negative $S(E_F)$ signals that transport is primarily due to electrons [38, 55].

Figure 4. 46 shows the Seebeck coefficient $S(E_F)$ evaluated at room temperature for different ranges $E_F - E_F^{DFT}$ for C-L**1**, while **Figure 4. 48** for C-L**2**.

By using DFT combined with the quantum transport code Gollum, the Seebeck coefficient $S(E_F)$ has been calculated. **Figure 4. 47** and **Figure 4. 49** show the corresponding $S(E_F)$ as a function of the Fermi energy E_F. The thermopower has been calculated for the twelve junctions, where the $E_F = 0$.

4.13.2 Seebeck coefficient for cross-linked molecule C-L1

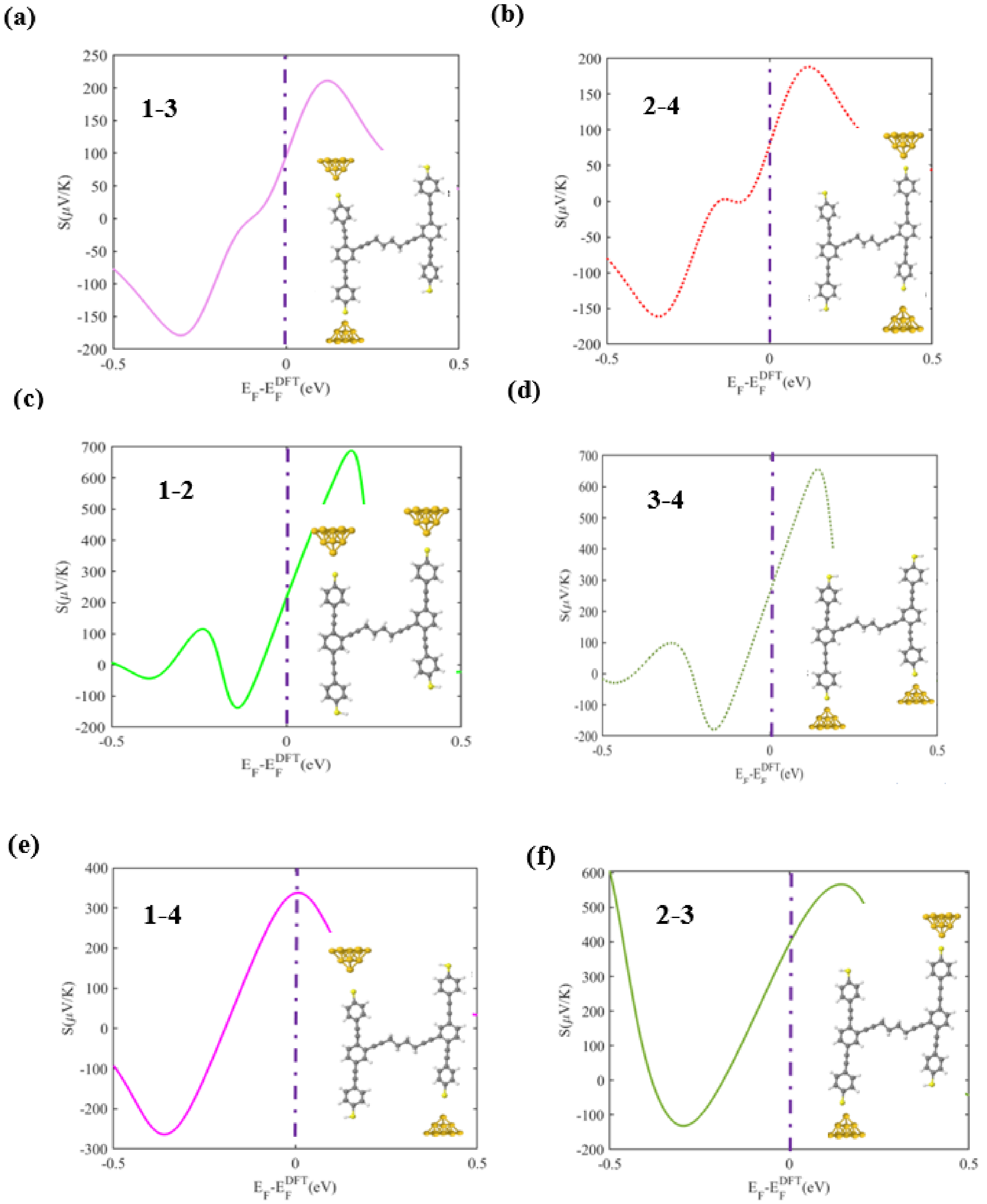

Figure 4. 46: Seebeck coefficient of the Au/C-L**1**/Au junctions in in six contact points (a) (**1-3**), (b) (**2-4**), (c) (**1-2**), (d) (**3-4**), (e) (**1-4**), and (f) (**2-3**).

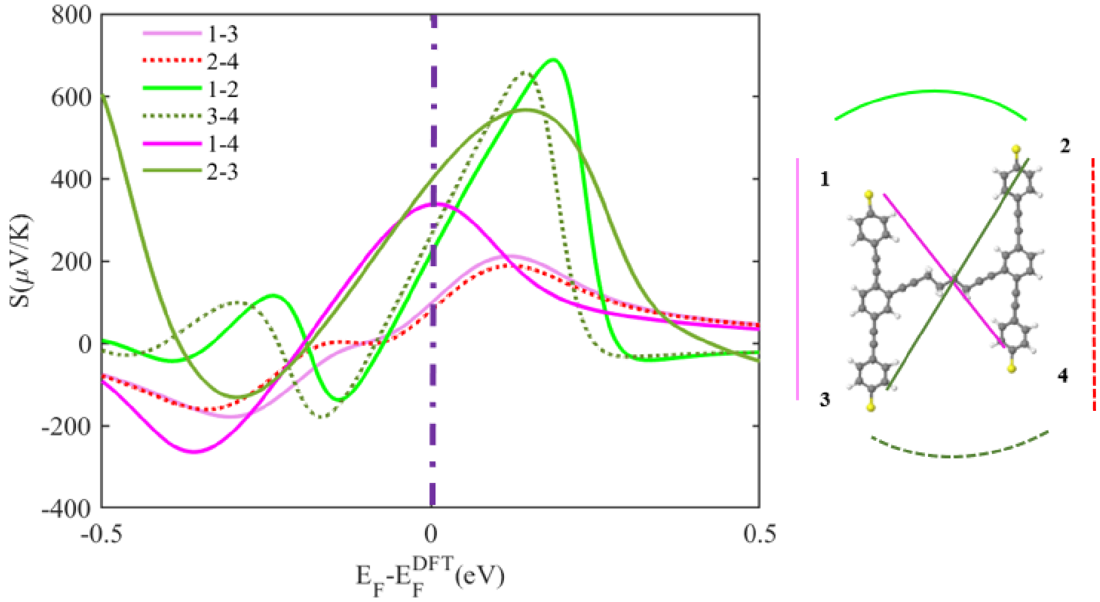

Figure 4. 47: Right panel: Schematic illustration of the Au/C-L**1**/Au junctions in in six contact points: (**1-3**), (**2-4**), (**1-2**), (**3-4**), (**1-4**), and **(2-3)**. **Left panel:** Seebeck coefficient $S(E_F)$ of Au/C-L**1**/Au junctions against electron energy E.

Table 4. 5: Seebeck coefficient $S(E_F)$ at DFT-predicted Fermi $E_F - E_F^{DFT} = 0\ eV$ for C-L**1**.

Compound	$S\ (\mu V\ K^{-1})$	Seebeck plot Figures
1-3	95.9	Figure 4. 46 (a)
2-4	78.3	Figure 4. 46 (b)
1-2	215	Figure 4. 46 (c)
3-4	260	Figure 4. 46 (d)
1-4	330	Figure 4. 46 (e)
2-3	390	Figure 4. 46 (f)

4.13.3 Seebeck coefficient for cross-linked molecule C-L2

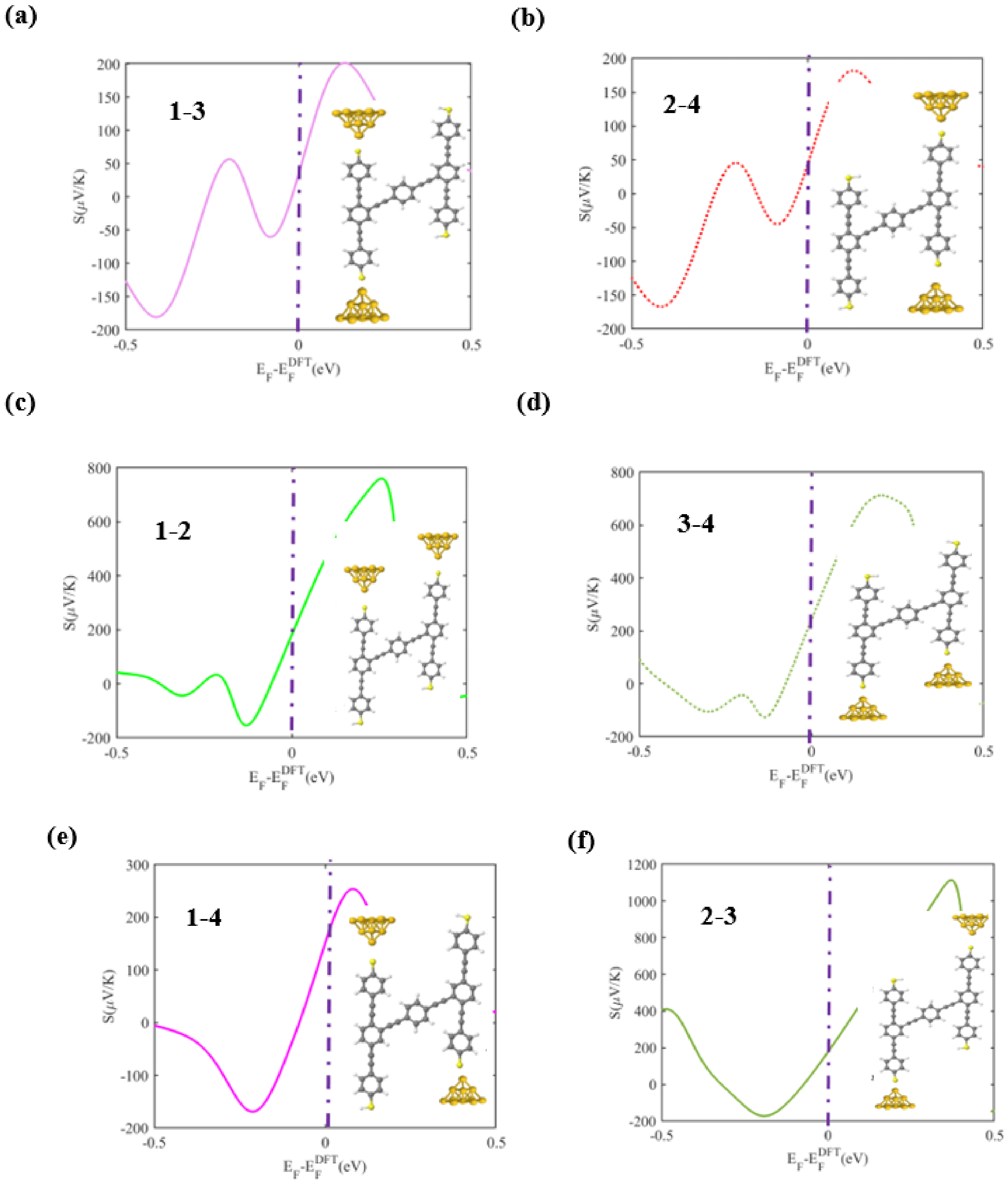

Figure 4. 48: Seebeck coefficient of the Au/C-L**2**/Au junctions in in six contact points (a) (**1-3**), (b) (**2-4**), (c) (**1-2**), (d) (**3-4**), (e) (**1-4**), and (f) (**2-3**).

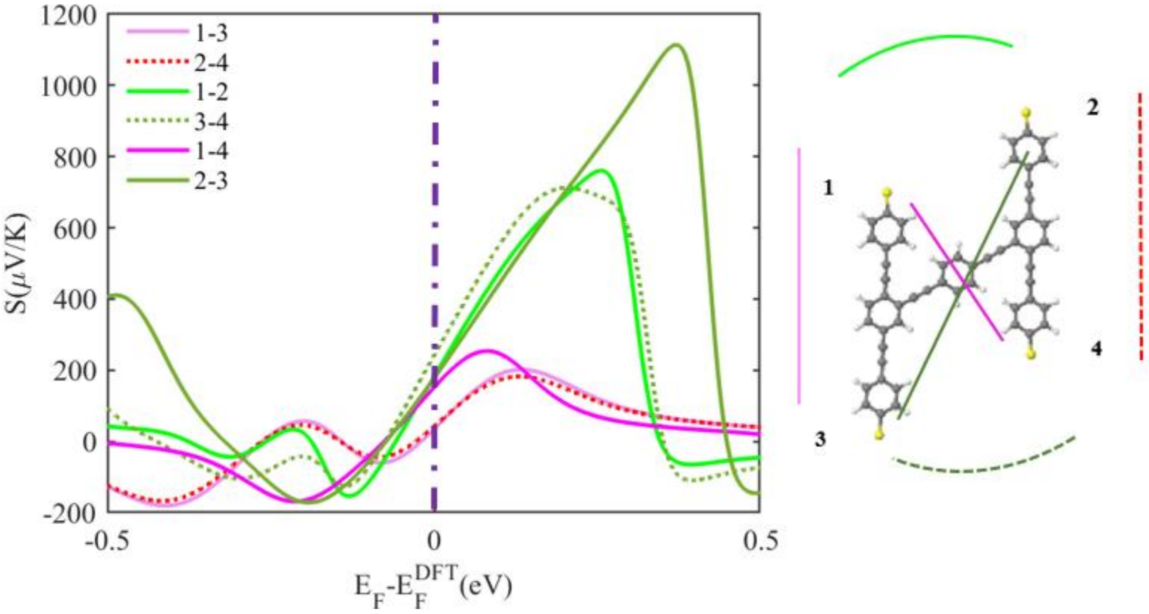

Figure 4. 49: Right panel: Schematic illustration of the Au/C-L**2**/Au junctions in in six contact points: (**1-3**), (**2-4**), (**1-2**), (**3-4**), (**1-4**), and (**2-3**). **Left panel:** Seebeck coefficient $S(E_F)$ of Au/C-L**2**/Au junctions against electron energy E.

Table 4. 6: Seebeck coefficient $S(E_F)$ at DFT-predicted Fermi $E_F - E_F^{DFT} = 0\ eV$ for C-L**2**.

Compound	$S\ (\mu V\ K^{-1})$	Seebeck plot Figures
1-3	34	Figure 4. 48 (a)
2-4	45	Figure 4. 48 (b)
1-2	181	Figure 4. 48 (c)
3-4	241	Figure 4. 48 (d)
1-4	151	Figure 4. 48 (e)
2-3	177	Figure 4. 48 (f)

Table 4. 5 shows the Seebeck coefficient values at the DFT-predicted Fermi $E_F - E_F^{DFT} = 0\ eV$ for the C-L**1** with six different options for thiol pair including **1-3**, **2-4**, **1-2**, **3-4**, **1-4**, and **2-3**. These are in the range between 78.3 and 390 $(\mu V\ K^{-1})$ for **2-4** *'para-para'* and **2-3** *'meta-meta'*. For **2-4** with '*para-para'* connectivity, the conductance G is high, but the Seebeck coefficient $S(E_E)$ is low. On the other hand, for **2-3**, if the connectivity is '*meta-meta*' the conductance is low, but the Seebeck coefficient is high. **Table 4. 6** shows the Seebeck coefficient values at the DFT-predicted Fermi energy $E_F - E_F^{DFT} = 0\ eV$ for the C-L**2** with six different options for thiol pair including **1-3**, **2-4**, **1-2**, **3-4**, **1-4**, and **2-3** which are in the range between 34 and $241(\mu V\ K^{-1})$ for **1-3** *'para-para'* and **3-4** '*meta-ortho'*. On the other hand, **1-3** if the connected *'Para-Para'* leading to high conductance, but a low Seebeck coefficient. On the other hand, for **3-4**, which is connected *meta-ortho* G is high conductance, and the Seebeck coefficient is high.

For the connectivity *meta-meta, meta-ortho*, the high Seebeck coefficient in this configuration arises from the stronger energy-dependent transmission near the Fermi level compared with the *meta-meta* or *meta-ortho* connections. This could be due to the molecular orbital alignment and the asymmetry introduced by the *meta-ortho* contact points, which enhance the thermoelectric response. For the connectivity *para-para*, this configuration might correspond to symmetry or constructive quantum interference in the electronic coupling, leading to a lower thermopower. The small value suggests a flatter energy dependence of the transmission near the Fermi level. These variations highlight how the quantum interference and contact geometry influence the thermoelectric properties of the molecule.

4.14 Conclusion

In this chapter, using both density functional theory and a tight-binding model, I have shown that the occurrence of destructive quantum interference DQI or constructive quantum interference CQI in cross-linked OPE3-based dimers is influenced by the way they are connected to external electrodes and depends on the pathway connectivity; in particular on whether *meta*-connected, *para*-connected or *ortho*-connected phenyl rings are present along the transport pathway. The transition from high to low electrical conductance when the connectivity to electrodes is switched is accompanied by an on-off ratio that can reach up to six orders of magnitude, as illustrated in **Figure 4. 44** and **Figure 4. 45**.

In the case the Seebeck coefficient, which reflects the degree to which the transmission changes with energy, I conclude that configurations with higher asymmetry or destructive quantum interference tend to increase $S(E_F)$, while symmetric or constructive interference configurations result in lower $S(E_F)$.

4.15 Bibliography

[1] X. Li, Y. Zheng, Y. Zhou, Z. Zhu, J. Wu, W. Ge, Y. Zhang, Y. Ye, L. Chen, J. Shi, Supramolecular Transistors with Quantum Interference Effect, Journal of the American Chemical Society, 145 (2023) 21679-21686.
[2] A. Alanazy, E. Leary, T. Kobatake, S. Sangtarash, M.T. González, H.-W. Jiang, G.R. Bollinger, N. Agräit, H. Sadeghi, I. Grace, Cross-conjugation increases the conductance of meta-connected fluorenones, Nanoscale, 11 (2019) 13720-13724.
[3] C. Tang, L. Huang, S. Sangtarash, M. Noori, H. Sadeghi, H. Xia, W. Hong, Reversible switching between destructive and constructive quantum interference using atomically precise chemical gating of single-molecule junctions, Journal of the American Chemical Society, 143 (2021) 9385-9392.
[4] S.-X. Liu, A.K. Ismael, A. Al-Jobory, C.J. Lambert, Signatures of room-temperature quantum interference in molecular junctions, Accounts of chemical research, 56 (2023) 322-331.
[5] V.M. García-Suárez, C.J. Lambert, D.Z. Manrique, T. Wandlowski, Redox control of thermopower and figure of merit in phase-coherent molecular wires, Nanotechnology, 25 (2014) 205402.
[6] Z. Wei, T. Li, K. Jennum, M. Santella, N. Bovet, W. Hu, M.B. Nielsen, T. Bjørnholm, G.C. Solomon, B.W. Laursen, Molecular junctions based on SAMs of cruciform oligo (phenylene ethynylene) s, Langmuir, 28 (2012) 4016-4023.
[7] Y.-Y. Sun, Z.-L. Peng, R. Hou, J.-H. Liang, J.-F. Zheng, X.-Y. Zhou, X.-S. Zhou, S. Jin, Z.-J. Niu, B.-W. Mao, Enhancing electron transport in molecular wires by insertion of a ferrocene center, Physical Chemistry Chemical Physics, 16 (2014) 2260-2267.
[8] L.A. Zotti, T. Kirchner, J.C. Cuevas, F. Pauly, T. Huhn, E. Scheer, A. Erbe, Revealing the role of anchoring groups in the electrical conduction through single-molecule junctions, small, 6 (2010) 1529-1535.
[9] Y. Li, M. Buerkle, G. Li, A. Rostamian, H. Wang, Z. Wang, D.R. Bowler, T. Miyazaki, L. Xiang, Y. Asai, Gate controlling of quantum interference and direct observation of anti-resonances in single molecule charge transport, Nature materials, 18 (2019) 357-363.
[10] C. Jia, M. Famili, M. Carlotti, Y. Liu, P. Wang, I.M. Grace, Z. Feng, Y. Wang, Z. Zhao, M. Ding, Quantum interference mediated vertical molecular tunneling transistors, Science advances, 4 (2018) eaat8237.

[11] Y. Kim, W. Jeong, K. Kim, W. Lee, P. Reddy, Electrostatic control of thermoelectricity in molecular junctions, Nature nanotechnology, 9 (2014) 881-885.

[12] A. Ismael, X. Wang, A. Al-Jobory, S. Ning, T. Alotaibi, B. Alanazi, H. Althobaiti, J. Wang, N. Wei, C.J. Ford, Tuning the electrical conductance of oligo (phenylene-ethynylene) derivatives-PbS quantum-dot bilayers, J Mater Chem C, 12 (2024) 14004-14012.

[13] C. Thiele, L. Gerhard, T.R. Eaton, D.M. Torres, M. Mayor, W. Wulfhekel, H. v Löhneysen, M. Lukas, STM study of oligo (phenylene-ethynylene) s, New journal of physics, 17 (2015) 053043.

[14] L.J. O'Driscoll, M.R. Bryce, A review of oligo (arylene ethynylene) derivatives in molecular junctions, Nanoscale, 13 (2021) 10668-10711.

[15] Y. Yang, A.L. Boehman, J.M. Simmie, Uniqueness in the low temperature oxidation of cycloalkanes, Combustion and Flame, 157 (2010) 2357-2368.

[16] S. Dooley, J. Heyne, S.H. Won, P. Dievart, Y. Ju, F.L. Dryer, Importance of a Cycloalkane Functionality in the Oxidation of a Real Fuel, Energy & fuels, 28 (2014) 7649-7661.

[17] V. Dragojlovic, Conformational analysis of cycloalkanes, ChemTexts, 1 (2015) 14.

[18] C. Jia, I.M. Grace, P. Wang, A. Almeshal, Z. Huang, Y. Wang, P. Chen, L. Wang, J. Zhou, Z. Feng, Redox control of charge transport in vertical ferrocene molecular tunnel junctions, Chem, 6 (2020) 1172-1182.

[19] A.K. Ismael, C.J. Lambert, Single-molecule conductance oscillations in alkane rings, J Mater Chem C, 7 (2019) 6578-6581.

[20] V. Obersteiner, D.A. Egger, E. Zojer, Impact of anchoring groups on ballistic transport: single molecule vs monolayer junctions, The Journal of Physical Chemistry C, 119 (2015) 21198-21208.

[21] D. Xiang, X. Wang, C. Jia, T. Lee, X. Guo, Molecular-scale electronics: from concept to function, Chemical reviews, 116 (2016) 4318-4440.

[22] E. Artacho, E. Anglada, O. Diéguez, J.D. Gale, A. García, J. Junquera, R.M. Martin, P. Ordejón, J.M. Pruneda, D. Sánchez-Portal, The SIESTA method; developments and applicability, Journal of Physics: Condensed Matter, 20 (2008) 064208.

[23] J.M. Soler, E. Artacho, J.D. Gale, A. García, J. Junquera, P. Ordejón, D. Sánchez-Portal, The SIESTA method for ab initio order-N materials simulation, Journal of Physics: Condensed Matter, 14 (2002) 2745.

[24] E. Engel, A. Höck, S. Varga, Relativistic extension of the Troullier-Martins scheme: Accurate pseudopotentials for transition-metal elements, Physical Review B, 63 (2001) 125121.

[25] P. Bugnion, P. López Ríos, R. Needs, G. Conduit, High-fidelity pseudopotentials for the contact interaction, Physical Review A, 90 (2014) 033626.

[26] I.L. Herrer, A.K. Ismael, D.C. Milán, A. Vezzoli, S. Martín, A. González-Orive, I. Grace, C. Lambert, J.L. Serrano, R.J. Nichols, Unconventional single-molecule conductance behavior for a new heterocyclic anchoring group: pyrazolyl, The journal of physical chemistry letters, 9 (2018) 5364-5372.

[27] H. Peng, J.P. Perdew, Rehabilitation of the Perdew-Burke-Ernzerhof generalized gradient approximation for layered materials, Physical Review B, 95 (2017) 081105.

[28] C.J. Lambert, S.X. Liu, A magic ratio rule for beginners: a chemist's guide to quantum interference in molecules, Chemistry–A European Journal, 24 (2018) 4193-4201.

[29] M. Famili, C. Jia, X. Liu, P. Wang, I.M. Grace, J. Guo, Y. Liu, Z. Feng, Y. Wang, Z. Zhao, Self-assembled molecular-electronic films controlled by room temperature quantum interference, Chem, 5 (2019) 474-484.

[30] R. Hoffmann, The many guises of aromaticity, Am. Sci, 103 (2015) 1511.

[31] P. De Clercq, We Need to Talk about Kekulé: The 150th Anniversary of the Benzene Structure, European Journal of Organic Chemistry, 2022 (2022) e202200171.

[32] N.R. Rajamohan, S.R. Ramanathan, S.R. Francis, Resolving set for line graph of linear benzene and polyphenyl structures, in: AIP Conference Proceedings, AIP Publishing, 2024.

[33] A. Almeshal, A.A. Al-Jobory, Z.Y. Mijbil, Precise control of single-phenanthrene junction’s conductance, Journal of Computational Electronics, 21 (2022) 71-79.

[34] I.M. Grace, G. Olsen, J. Hurtado-Gallego, L. Rincón-García, G. Rubio-Bollinger, M.R. Bryce, N. Agraït, C.J. Lambert, Connectivity dependent thermopower of bridged biphenyl molecules in single-molecule junctions, Nanoscale, 12 (2020) 14682-14688.

[35] A. Ismael, X. Wang, T.L. Bennett, L.A. Wilkinson, B.J. Robinson, N.J. Long, L.F. Cohen, C.J. Lambert, Tuning the thermoelectrical properties of anthracene-based self-assembled monolayers, Chemical science, 11 (2020) 6836-6841.

[36] A.K. Ismael, I. Grace, C.J. Lambert, Connectivity dependence of Fano resonances in single molecules, Physical Chemistry Chemical Physics, 19 (2017) 6416-6421.

[37] N. Kobko, J. Dannenberg, Effect of basis set superposition error (BSSE) upon ab initio calculations of organic transition states, The Journal of Physical Chemistry A, 105 (2001) 1944-1950.

[38] M. Alshammari, A.A. Al-Jobory, T. Alotaibi, C.J. Lambert, A. Ismael, Orientational control of molecular scale thermoelectricity, Nanoscale Advances, 4 (2022) 4635-4638.

[39] A. Alshehab, Quantum Transport of Alkane Derivatives in Nanoscale Structures, Lancaster University (United Kingdom), 2022.

[40] C.R. Arroyo, S. Tarkuc, R. Frisenda, J.S. Seldenthuis, C.H. Woerde, R. Eelkema, F.C. Grozema, H.S. Van Der Zant, Signatures of quantum interference effects on charge transport through a single benzene ring, Angewandte Chemie International Edition, 52 (2013) 3152-3155.

[41] A.A. Al-Jobory, A.K. Ismael, Controlling quantum interference in tetraphenyl-aza-BODIPYs, Current Applied Physics, 54 (2023) 1-4.

[42] J. Ye, A. Al-Jobory, Q.-C. Zhang, W. Cao, A. Alshehab, K. Qu, T. Alotaibi, H. Chen, J. Liu, A.K. Ismael, Highly insulating alkane rings with destructive σ-interference, Science China Chemistry, 65 (2022) 1822-1828.

[43] T. Kim, P. Darancet, J.R. Widawsky, M. Kotiuga, S.Y. Quek, J.B. Neaton, L. Venkataraman, Determination of energy level alignment and coupling strength in 4, 4′-bipyridine single-molecule junctions, Nano letters, 14 (2014) 794-798.

[44] J. Ferrer, C.J. Lambert, V.M. García-Suárez, D.Z. Manrique, D. Visontai, L. Oroszlány, R. Rodríguez-Ferradás, I. Grace, S. Bailey, K. Gillemot, GOLLUM: a next-generation simulation tool for electron, thermal and spin transport, New Journal of Physics, 16 (2014) 093029.

[45] G.C. Solomon, C. Herrmann, T. Hansen, V. Mujica, M.A. Ratner, Exploring local currents in molecular junctions, Nature Chemistry, 2 (2010) 223-228.

[46] S. Grimme, C. Bannwarth, P. Shushkov, A robust and accurate tight-binding quantum chemical method for structures, vibrational frequencies, and noncovalent interactions of large molecular systems parametrized for all spd-block elements (Z= 1–86), Journal of chemical theory and computation, 13 (2017) 1989-2009.

[47] M.T. González, A.K. Ismael, M. Garcia-Iglesias, E. Leary, G. Rubio-Bollinger, I. Grace, D. Gonzalez-Rodriguez, T. Torres, C.J. Lambert, N. Agrait, Interference controls conductance in phthalocyanine molecular junctions, The Journal of Physical Chemistry C, 125 (2021) 15035-15043.

[48] A.K. Ismael, 20-state molecular switch in a Li@ C60 complex, ACS omega, 8 (2023) 19767-19771.

[49] S.V. Aradhya, L. Venkataraman, Single-molecule junctions beyond electronic transport, Nature nanotechnology, 8 (2013) 399-410.

[50] D. Miguel, L. Alvarez de Cienfuegos, A. Martín-Lasanta, S.P. Morcillo, L.A. Zotti, E. Leary, M. Bürkle, Y. Asai, R. Jurado, D.J. Cárdenas, Toward multiple conductance pathways with heterocycle-based oligo (phenyleneethynylene) derivatives, Journal of the American Chemical Society, 137 (2015) 13818-13826.

[51] L. Herrer, A. Ismael, S. Martín, D.C. Milan, J.L. Serrano, R.J. Nichols, C. Lambert, P. Cea, Single molecule vs. large area design of molecular electronic devices incorporating an efficient 2-aminepyridine double anchoring group, Nanoscale, 11 (2019) 15871-15880.

[52] T.L. Bennett, M. Alshammari, S. Au-Yong, A. Almutlg, X. Wang, L.A. Wilkinson, T. Albrecht, S.P. Jarvis, L.F. Cohen, A. Ismael, Multi-component self-assembled molecular-electronic films: towards new high-performance thermoelectric systems, Chemical Science, 13 (2022) 5176-5185.

[53] W. Hong, H. Valkenier, G. Mészáros, D.Z. Manrique, A. Mishchenko, A. Putz, P.M. García, C.J. Lambert, J.C. Hummelen, T. Wandlowski, An MCBJ case study: The influence of π-conjugation on the single-molecule conductance at a solid/liquid interface, Beilstein journal of nanotechnology, 2 (2011) 699-713.

[54] H.E. Skipper, B. Lawson, X. Pan, V. Degtiareva, M. Kamenetska, Manipulating Quantum Interference between σ and π Orbitals in Single-Molecule Junctions via Chemical Substitution and Environmental Control, ACS nano, 17 (2023) 16107-16114.

[55] A.K. Ismael, I. Grace, C.J. Lambert, Increasing the thermopower of crown-ether-bridged anthraquinones, Nanoscale, 7 (2015) 17338-17342.

Chapter 5

Influence of the linking bridge in cross-linked OPE3 dimers

5.1 Introduction

This research was conducted in collaboration with Prof. Nicholas Long's group (Department of Chemistry, Imperial College London), who suggested the studied molecules used in this work. I performed the theoretical analysis at Lancaster. The study will be submitted soon.

This chapter is an extension to chapter 4. In this chapter, I am going to include two more bridges donated **3** and **4** in **Figure 5. 1**, to form cross-linked molecules C-L**3** and C-L**4** shown in **Figure 5. 2**. I Consider the role of linker **3**, which is called oligophenylene vinylene[1, 2] and **4**, which is called 2,6-bis (2-pyridyl) benzene [3], obtained by inserting thiophenes into the bridges of C-L**1** and C-L**2**, respectively, as shown in **Figure 5. 1** to examine the effect of introducing 5-membered rings, which break the bipartite nature of dimers C-L**1** and C-L**2** in chapter 4. The density functional theory DFT-based transport simulations were investigated to analyse the electrical conductance exhibited by two cross-linked OPE3 dimers (i.e., C-L**3** and C-L**4**). To identify specific connectivity configurations conducive to high conductance and those leading to lower levels of electrical conductivity (CQI and DQI). I aim to examine whether different types of bridges have cross-linked impact transport properties. **Figure 5. 1** shows the fully relaxed isolated structures of the three building blocks, OPE3 and **3, 4**.

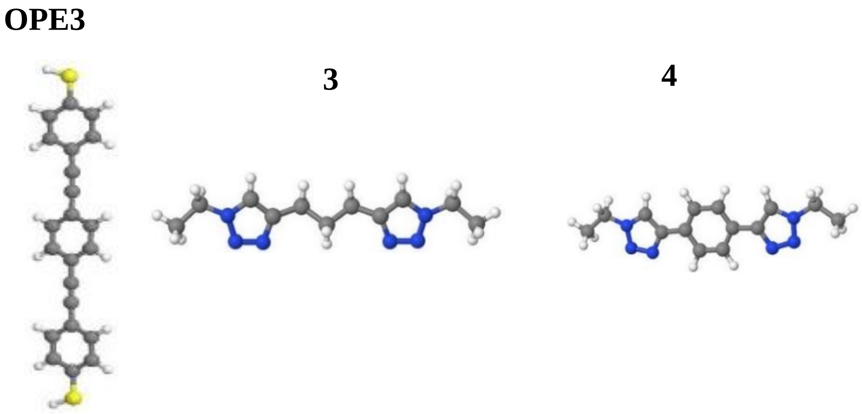

Figure 5. 1: Fully relaxed isolated molecules of three single components, OPE3 and (**3)** oligophenylene vinylene**, (4)** 2,6-bis (2-pyridyl) benzene. (Note: see **1** and **2** bridges in chapter 4).

The two molecular structures C-L**3** and C-L**4** were cross-linked by connecting components **3** and **4** with OPE (as depicted in **Figure 5.1**), and subsequently, the system was allowed to relax fully, resulting in the formation of cross-linked dimers, shown in **Figure 5. 2**.

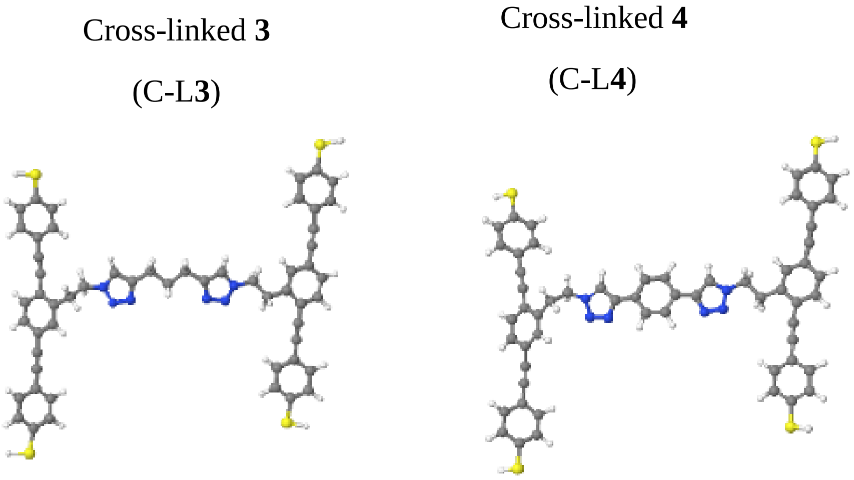

Figure 5. 2: Schematic illustrations of two OPE3 molecules bridged by **3** and **4** components (Figure 5. 1), to form cross-linked dimers C-L**3** and C-L**4,** respectively.

5.2 Frontier molecular orbitals

I repeated the same procedures mentioned in section (4.4), to better understand the electronic properties of the studied molecules **Figure 5. 3** and **Figure 5. 4**. First, the frontier orbitals were investigated for all the gas-phase molecules. Their highest occupied molecular orbitals (HOMO) and lowest unoccupied orbitals (LUMO), (HOMO+1), and (LUMO-1), in addition to (HOMO+2) and (LUMO-2), along with their energies were computed. The plots below show iso-surfaces of the HOMO, LUMO, HOMO-1, LUMO+1 HOMO-2 and LUMO+2 of isolated monomer and dimer molecules. I applied the orbital product rule OPR in the next section. Typically, the Fermi energy E_F falls within the energy gap between the highest occupied molecular orbital HOMO and the lowest unoccupied molecular orbital LUMO of the molecule. This positioning allows for certain simplifications that would not apply if E_F were aligned with either the HOMO or energy levels[4, 5]. Later on, I shall check this OPR prediction against the DFT results. It should be noted that both C-L**3** and C-L**4** have degenerate HOMO and LUMO levels, as we also noted for C-L**1** and C-L**2** in chapter 4 (see **Figure 4. 4** and **Figure 4. 5**).

5.2.1 Cross-linked molecule C-L3

E_F= - 2.86 eV

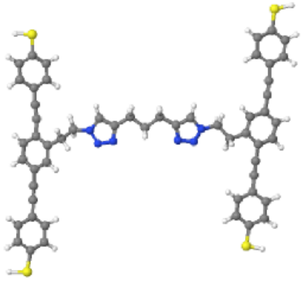

(a)

HOMO= - 4.56 eV LUMO= - 2.16 eV

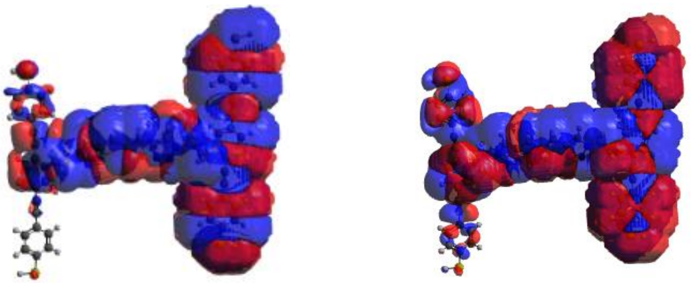

(b)

HOMO-1= - 4.57 eV LUMO+1= - 2.05 eV

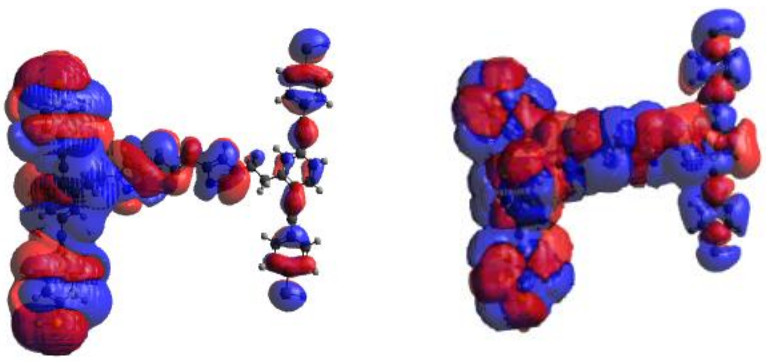

(c)

HOMO-2= - 4.74 eV LUMO+2= - 1.50 eV

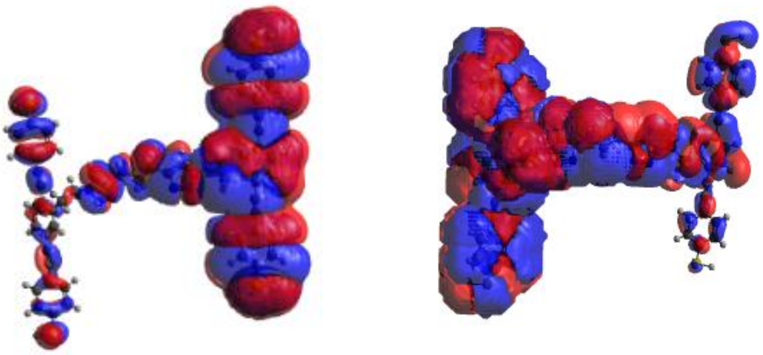

Figure 5. 3: Wave function for cross-linked **3**. **Top panel**: fully optimised geometry of C-L**3**. **Lower panel**: HOMO, LUMO, HOMO-1, LUMO+1, HOMO-2, LUMO+2 of cross-linked **3**, along with their energies.

5.2.2 Cross-linked molecule C-L4

E_F= - 4.69 eV

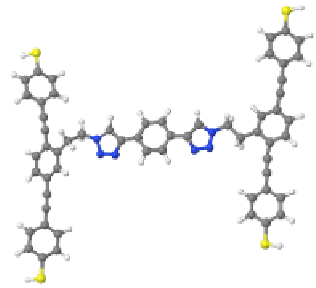

(a)

HOMO= - 4.70 eV

LUMO= - 2.33 eV

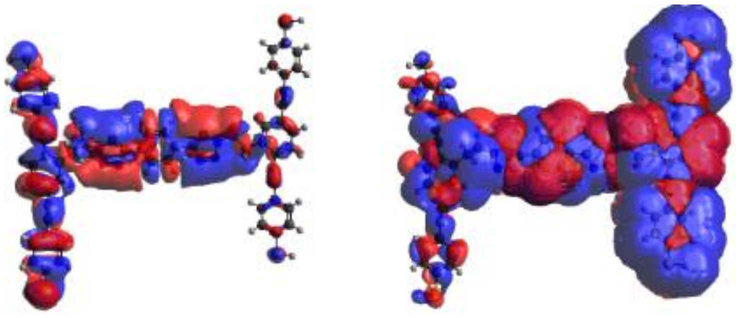

(b)

LUMO+1= - 2.11 eV

HOMO-1= - 4.72 eV

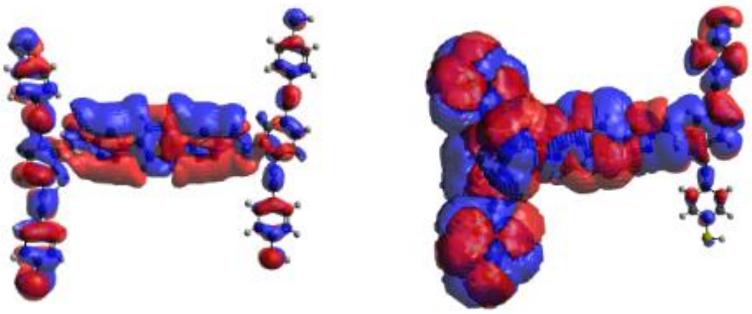

(c)

HOMO-2= - 4.82 eV

LUMO+2= - 1.54 eV

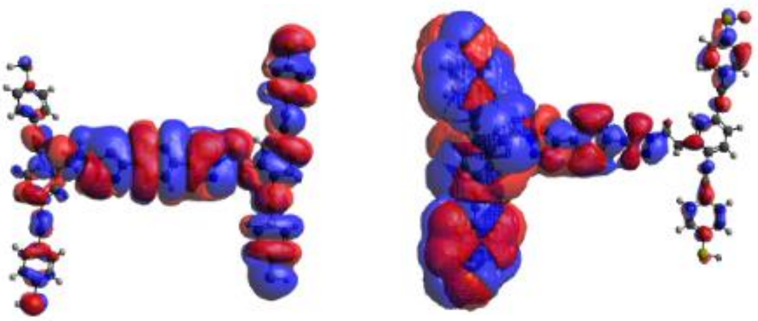

Figure 5. 4: Wave function for cross-linked **4**. **Top panel:** fully optimised geometry of C-L4. **Lower panel:** HOMO, LUMO, HOMO-1, LUMO+1, HOMO-2, LUMO+2 of cross-linked **4**, along with their energies.

5.3 Orbital product rule (OPR)

This section aims to examine the electrical conductance of a novel dimer, where a source electrode is connected to one thiol group and a drain electrode to another. These C-L dimers involve four terminal thiol end-groups. The orbital product rule shall be employed to predict the quantum interference properties for six distinct electrode contact configurations for the two cross-linked dimers in **Figure 5. 3** and **Figure 5. 4**.

To apply this rule, two contact points are considered as follows: **1-3**, **2-4**, **1-2**, **3-4**, **1-4**, and **2-3**. These six pairs of contacting points are shown in **Figure 5.5** [6-11]. It is worth mentioning that the studied molecules possess four contacting points (**1, 2, 3** and **4**), as shown in Error! R eference source not found. below.

Table 5. 1 illustrates the orbital product rule predictions for the two studied molecules: cross-linked **3** and cross-linked **4** (C-L**3** and C-L**4**). The product rule applies to the six contact points to determine whether the quantum interference is constructive (CQI) or distractive (DQI). The OPR predicts a constructive quantum interference (CQI) for the contact points **2-3**, **2-4**, **1-2** and **3-4**. On the other hand, it predicts a destructive quantum interference (DQI) for the contact points **1-3**, **1-4**, and **3-4**. These predictions for the cross-linked **3** and the cross-linked **4** are presented in the second and third rows of **Table 5. 1**.

Table 5. 1: Orbital product rule predictions of six contact points **1-3**, **2-4**, **1-2**, **3-4**, **1-4**, and **2-3**, for cross-linked dimers C-L**3** and C-L**4** (Note: C for constructive and D for destructive QI).

Cross-linked	Contact points	OPR prediction	Wavefunction plot Figure
C-L**3**	**1-3**, **2-4**	D, C	Figure 5. 3 (a)
	1-2, **3-4**	C, D	Figure 5. 3 (a)
	1-4, **2-3**	D, C	Figure 5. 3 (a)
C-L**4**	**1-3**, **2-4**	D, C	Figure 5. 4 (a)
	1-2, **3-4**	C, D	Figure 5. 4 (a)
	1-4, **2-3**	D, C	Figure 5. 4 (a)

5.4 Cross-linked dimers in Au-Au junction

Starting from the optimised structures and geometries for the compounds shown in **Figure 5. 2**. The tight-binding model TBM will be applied to the C-L**3** and C-L**4** illustrated in **Figure 5. 5** and **Figure 5. 6** to evaluate whether the results are consistent with the product rule outlined in Section 5.5. In addition, the SIESTA code was employed to compute self-consistent optimised geometries, ground-state Hamiltonians, and overlap matrix elements [12-14]. Subsequently, the Gollum quantum transport code was utilised to calculate the transmission coefficient, as detailed in Section 5.6. The final parameter to be calculated is the Seebeck coefficient, $S(E_F)$, for the gold-molecule-gold junction, as described in detail in Section 5.7. This section includes C-L**3** and C-L**4**, with SH as the anchor group. For more information about all studied components, see Chapter 4.

5.4.1 Cross-linked 3 possible contact points

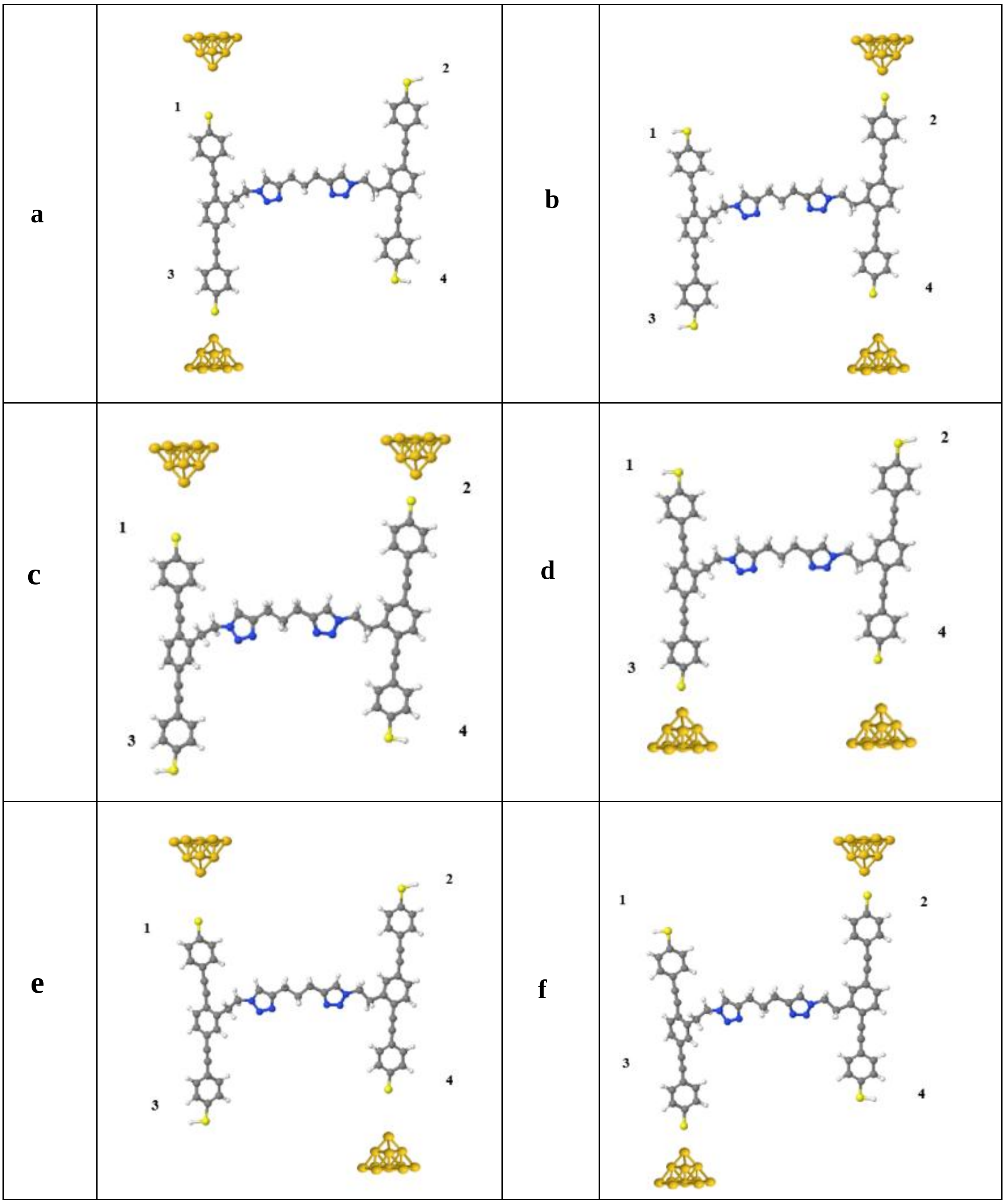

Figure 5. 5: Schematic illustration of the Au/C-L**3**/Au junctions in six different contact points: a (**1-3**), b (**2-4**), c (**1-2**), d (**3-4**), e (**1-4**), and f (**2-3**).

5.4.2 Cross-linked 4 possible contact points

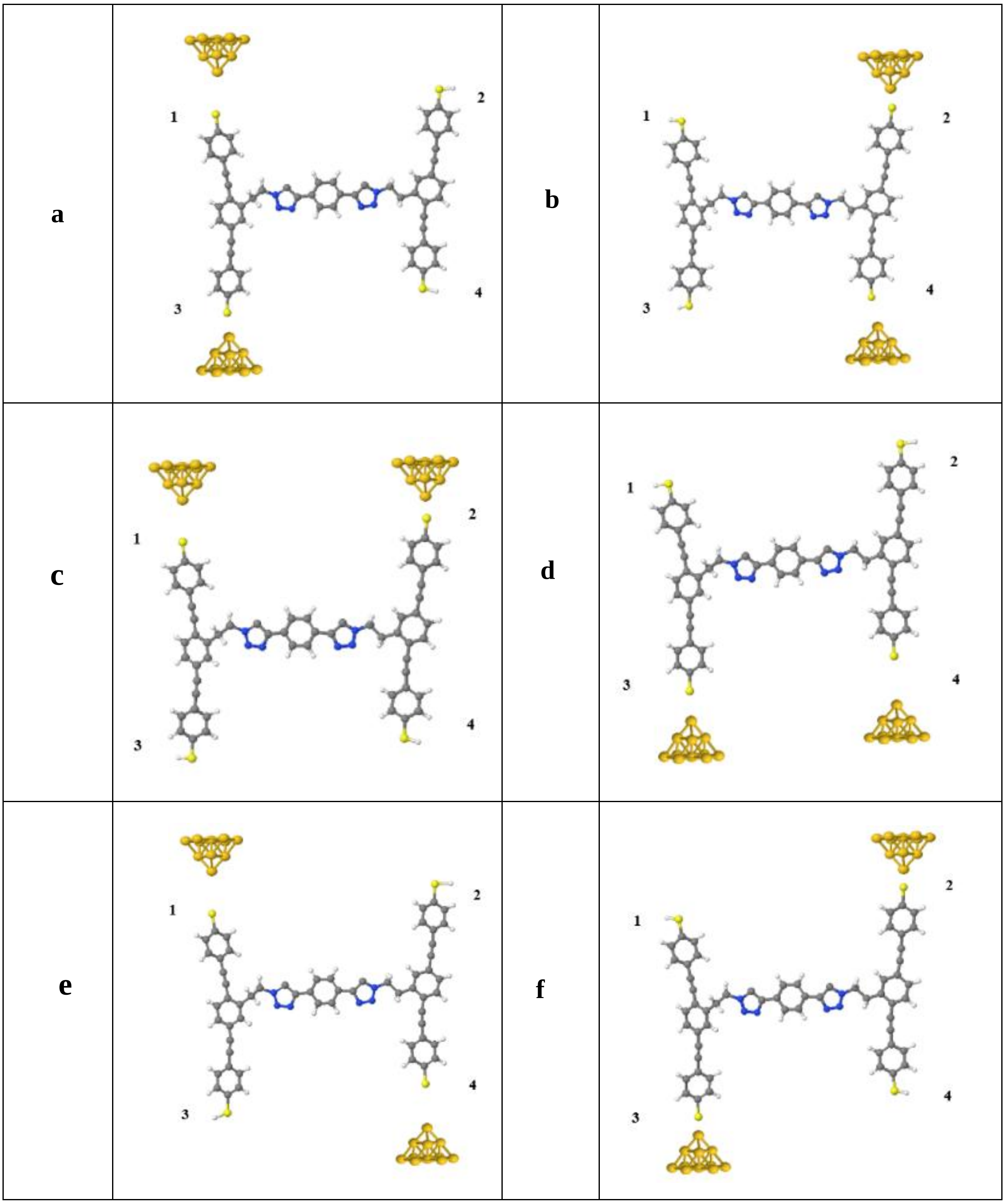

Figure 5. 6: Schematic illustration of the Au/C-L**4**/Au junctions in six different contact points: a (**1-3**), b (**2-4**), c (**1-2**), d (**3-4**), e (**1-4**), and f (**2-3**).

5.5 Tight binding model (TBM)

To investigate the quantum interference predictions mentioned above, I develop a Hückel (tight-binding, TB) Hamiltonian model [15-21]. As discussed in the previous chapter, section (4.9). **Figure 5. 7** and **Figure 5. 8** show the transmission coefficient $T(E)$ for cross-linked C-L**3** and the $T(E)$ for cross-linked C-L**4**, respectively. Illustrate similar behaviours, with three junctions resulting in CQI; on the other hand, the remaining junctions result in DQI (dimers **1** and **2** display the same behaviour, see section 4.9 in chapter 4).

The first set of results involves coupling semi-infinite one-dimensional crystalline leads to sites **1** and **3** or **2** and **4**, producing the red solid and dotted curves in **Figure 5. 7** and **Figure 5. 8**, respectively. These curves clearly indicate constructive quantum interference CQI. Conversely, when leads are connected to sites **1** and **2** in the second set, the green solid curve is observed, showing a signature transmission dip, indicating destructive quantum interference DQI. Similarly, coupling to sites **3** and **4** yields the green dotted curve, also indicative of DQI. When leads are attached to sites **1** and **4**, the purple solid curve is generated, showing no DQI signature (it reflects CQI). In contrast, coupling to sites **2** and **3** produces the light green solid curve, which displays a DQI dip. The tight-binding transmission coefficients for cross-linked dimers **3** and **4** reveal that the nature of the bridging linker has no significant impact on the transmission curves, as all four dimers exhibit similar behaviour across the six different contact pairings. (Note: at the TBM level).

Table 5. 2 presents the TBM results, which reveal that the occurrence of destructive quantum interference DQI is independent of the type of bridging linker. Additionally, the results confirm that the **1-3**, **2-4**, and **1-4** connectivities display high conductance, attributed to constructive quantum interference CQI, while the **1-2**, **3-4**, and **2-3** connectivities exhibit low conductance

due to the presence of DQI. Now, to have a full comparison, meaning include dimers **1** and **2** (studied in chapter 4), the only difference one could notice is that the transmission curves of dimers (**1** and **2**) are symmetric, whereas (**3** and **4**) are asymmetric. I attribute that to the fact that (**1** and **2**) are bipartite molecules while (**3** and **4**) are not (please compare **Figure 4. 22** and **Figure 4. 29** against **Figure 5. 7** and **Figure 5. 8**).

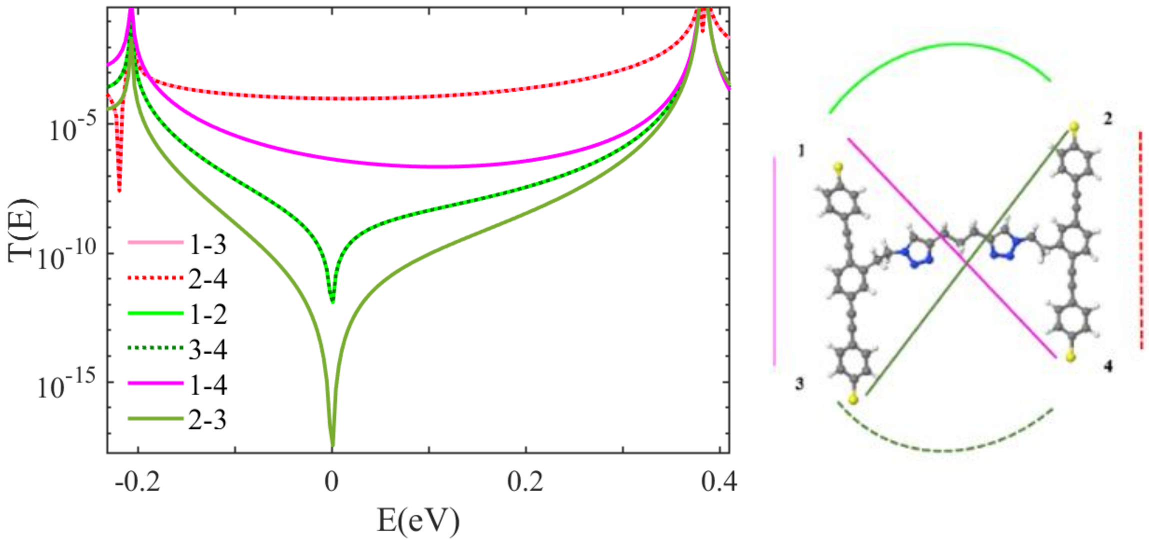

Figure 5. 7: Right panel: Schematic illustration of the Tight binding transmission coefficients $T(E)$ of 1D lead/C-**3**/1D lead, in six contact points: (**1-3**), (**2-4**), (**1-2**), (**3-4**), (**1-4**), and (**2-3**). **Left panel:** Transmission coefficients $T(E)$ by TBM of Au/C-L**1**/Au junctions against electron energy E.

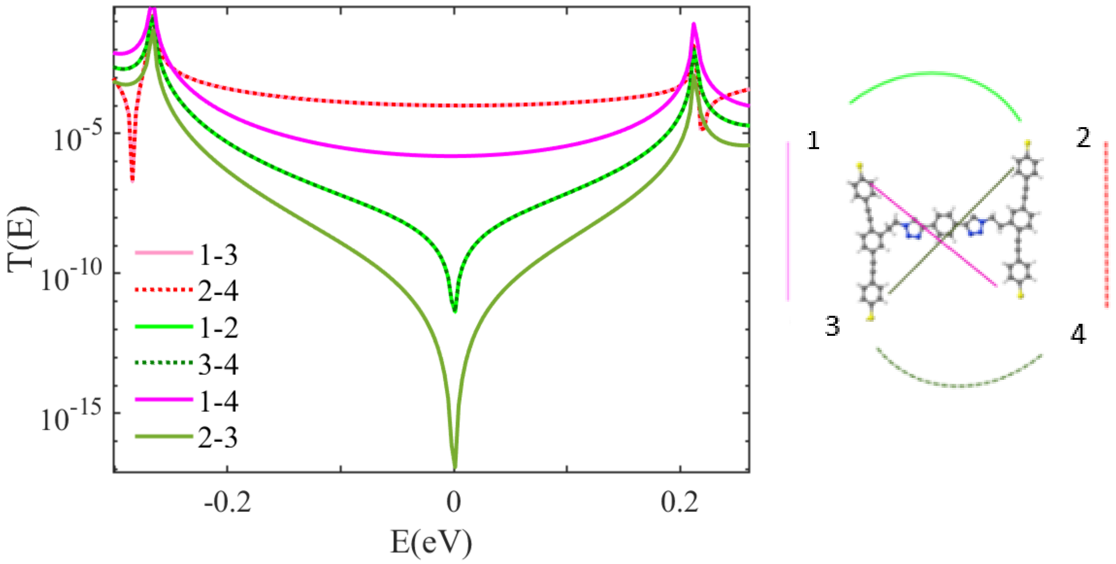

Figure 5. 8: Right panel: Schematic illustration of the tight binding transmission coefficients $T(E)$ of 1D lead/C-**4**/1D lead in six contact points: (**1-3**), (**2-4**), (**1-2**), (**3-4**), (**1-4**), and (**2-3**). **Left panel:** Transmission coefficients $T(E)$ by TBM of Au/C-L**1**/Au junctions against electron energy E.

Table 5. 2: TBM results for cross-linked **3** and **4**, in six different contact points (Note: C for constructive and D for destructive QI).

Cross-linked	Contact point	TBM results	TBM Figures
C-L**3**	**1-3, 2-4** **1-2, 3-4** **1-4, 2-3**	C, C D, D C, D	Figure 5. 7 Figure 5. 7 Figure 5. 7
C-L**4**	**1-3, 2-4** **1-2, 3-4** **1-4, 2-3**	C, C D, D C, D	Figure 5. 8 Figure 5. 8 Figure 5. 8

5.6 DFT transport simulation in Au-Au junction

As described in section (4.10) of chapter 4, I started with the wholly optimised gas-phase molecules to investigate the transmission coefficient. Then, I constructed the junctions by attaching the molecules via the thiol anchor group to gold. Similar to the computations shown in Chapter 4, the transmission coefficient $T(E)$ will be investigated by DFT. The ground state Hamiltonian and optimised geometry of each compound were obtained using the density functional theory DFT code and combined with the Gollum transport code [22, 23]. Section (5.6.1) will show the results of C-L**3**, while section (5.6.2) will show the C-L**4** results. The transmission coefficients $T(E)$ for cross-linked **3** are shown **Figure 5. 9** to **Figure 5. 14**. Meanwhile, **Figure 5. 16** to **Figure 5. 21** show the transmission coefficients $T(E)$ for C-L**4**.

5.6.1 Transport simulation in Au-Au junction for cross-linked (3)

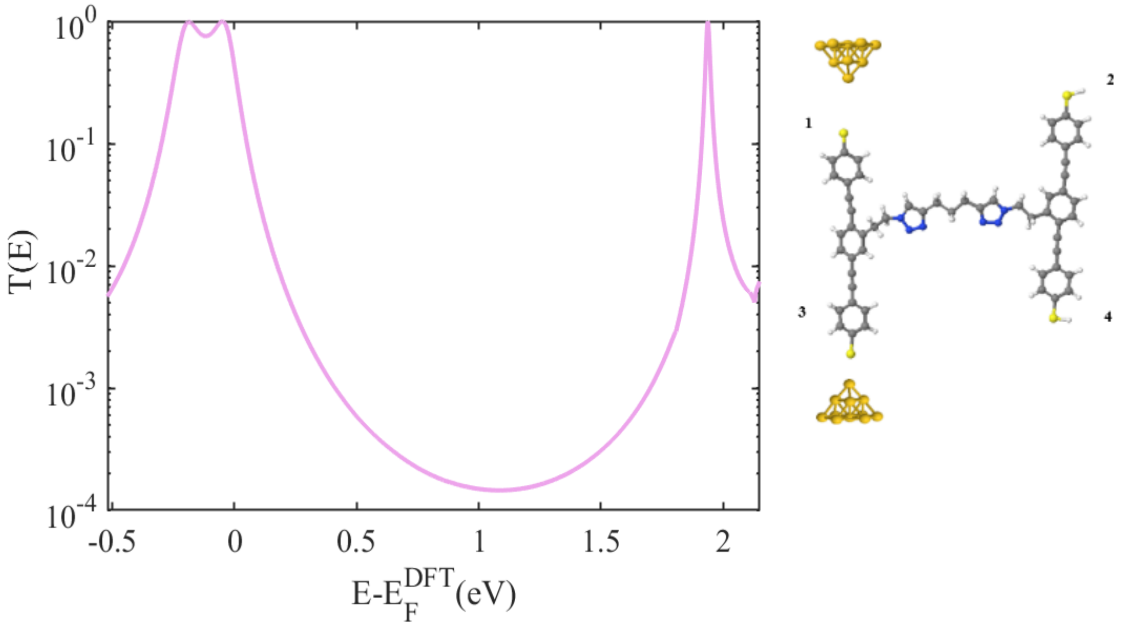

Figure 5. 9: Right panel: Schematic illustration of the Au/C-L**3**/Au junctions in (**1**-**3**) contact points. **Left panel**: Transmission coefficient $T(E)$ of Au/C-L**3**/Au junctions against electron energy E.

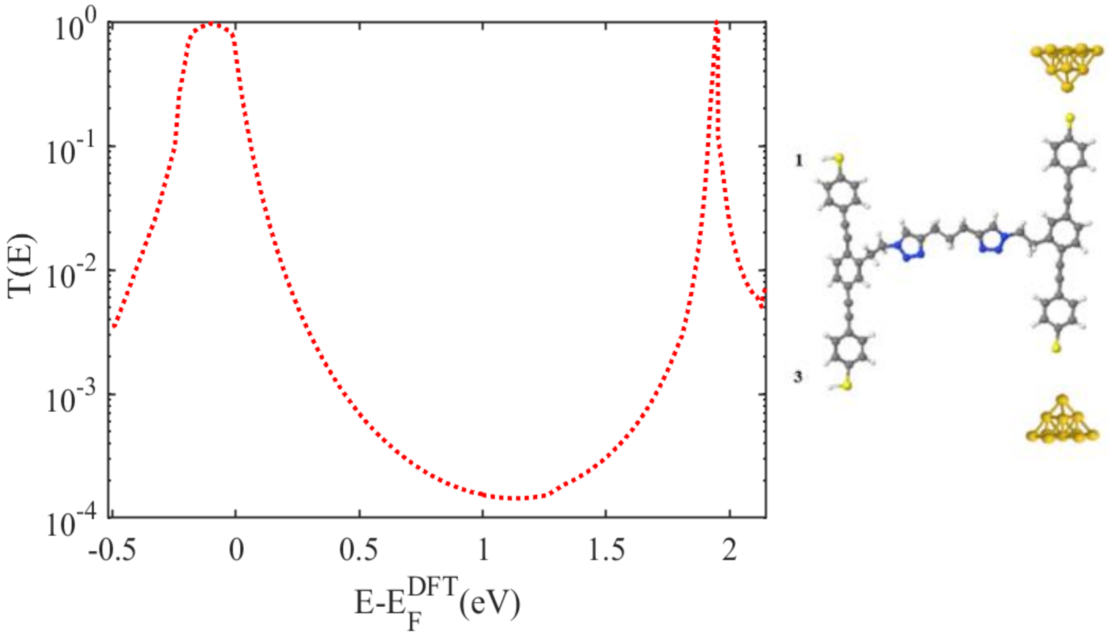

Figure 5. 10: Right panel: Schematic illustration of the Au/C-L**3**/Au junctions in (**2**-**4**) contact points. **Left panel**: Transmission coefficient $T(E)$ of Au/C-L**3**/Au junctions against electron energy E.

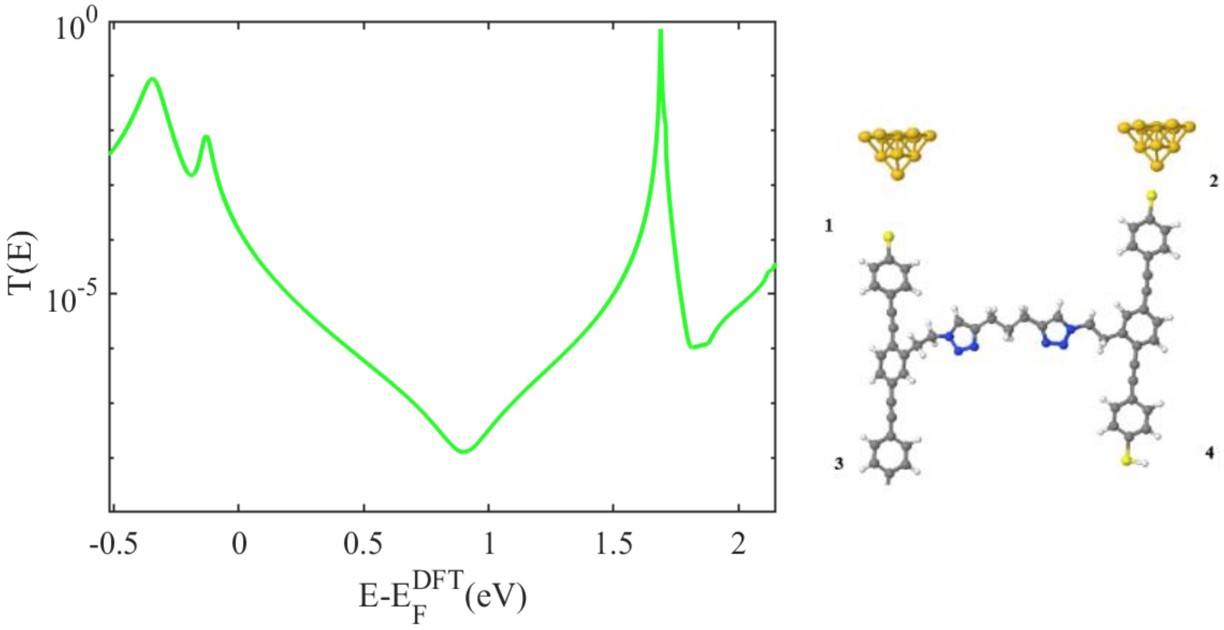

Figure 5. 11: Right panel: Schematic illustration of the Au/C-L**3**/Au junctions in (**1**-**2**) contact points. **Left panel**: Transmission coefficient $T(E)$ of Au/C-L**3**/Au junctions against electron energy E.

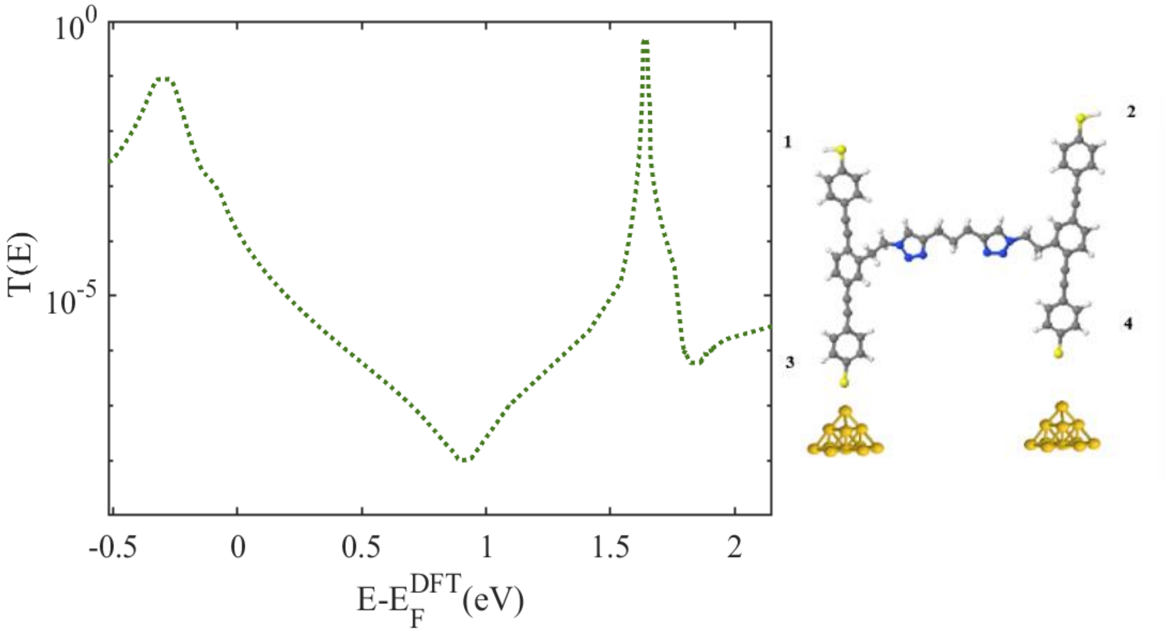

Figure 5. 12: Right panel: Schematic illustration of the Au/C-L**3**/Au junctions in (**3-4**) contact points. **Left panel**: Transmission coefficient $T(E)$ of Au/C-L**3**/Au junctions against electron energy E.

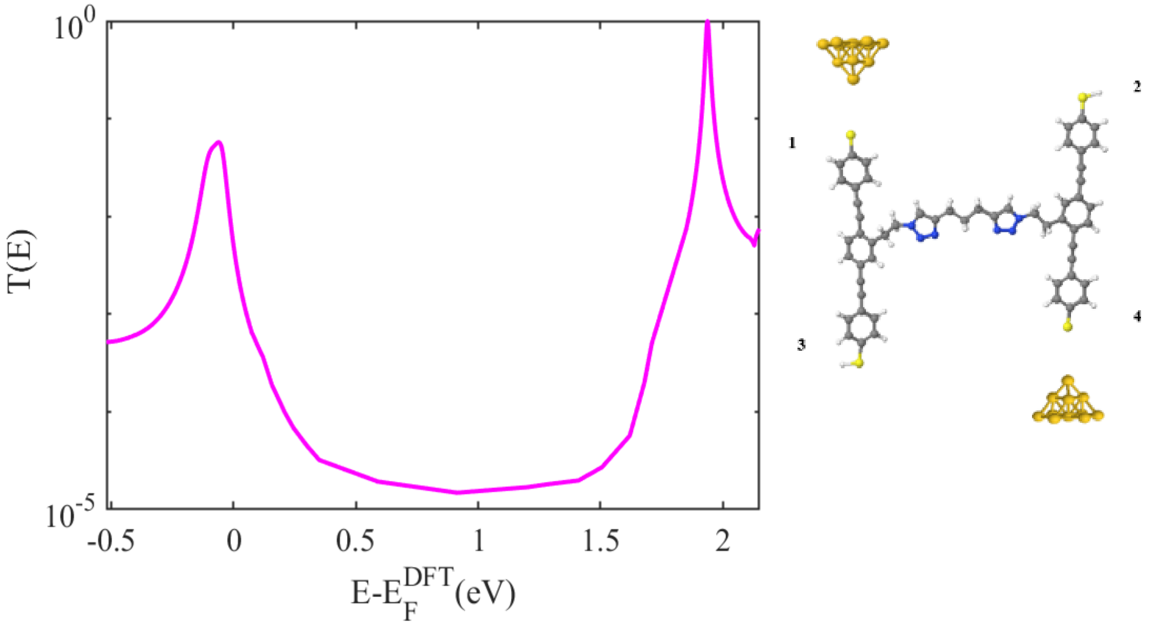

Figure 5. 13: Right panel: Schematic illustration of the Au/C-L**3**/Au junctions in (**1-4**) contact points. **Left panel**: Transmission coefficient $T(E)$ of Au/C-L**3**/Au junctions against electron energy E.

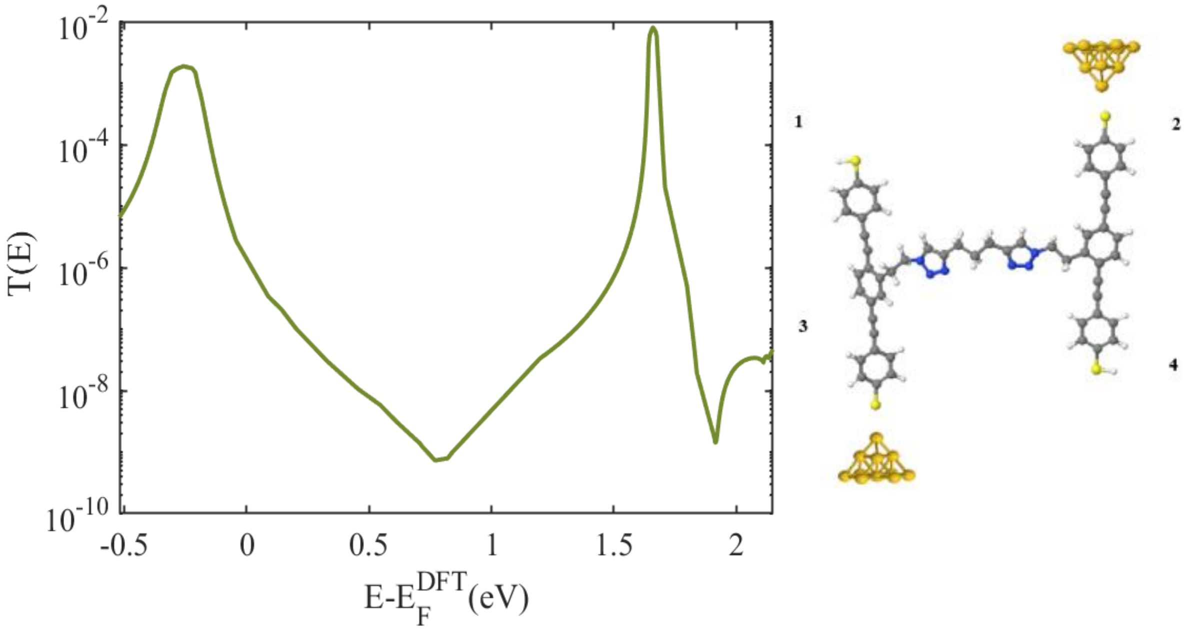

Figure 5. 14: Right panel: Schematic illustration of the Au/C-L**3**/Au junctions in (**2-3**) contact points. **Left panel:** Transmission coefficient $T(E)$ of Au/C-L**3**/Au junctions against electron energy E.

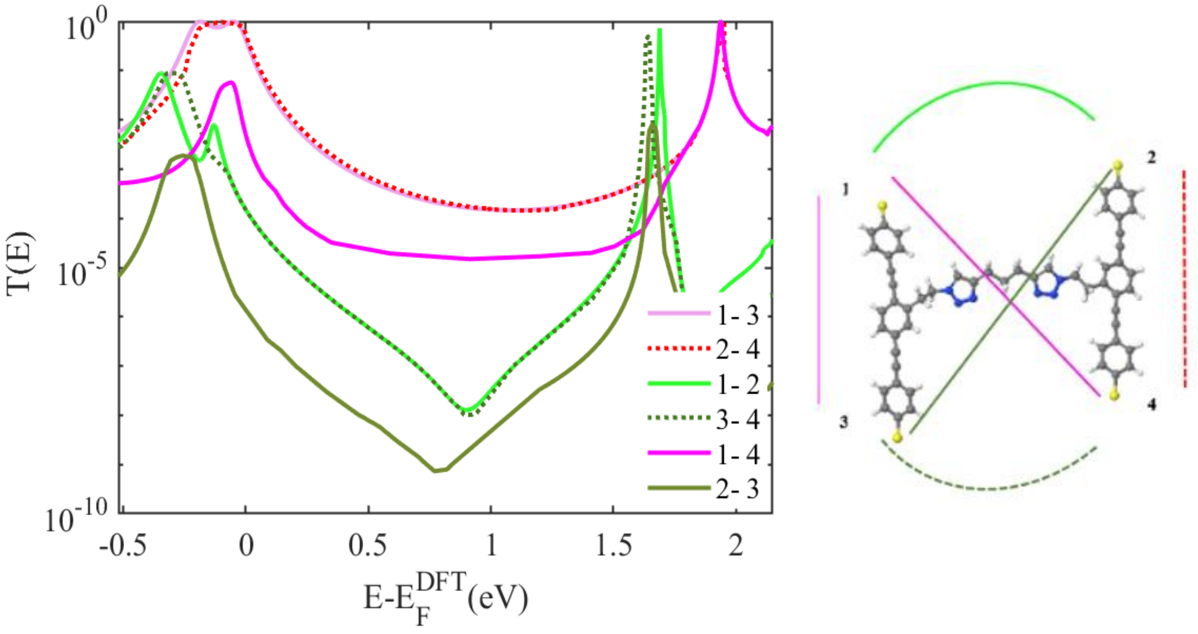

Figure 5. 15: Right panel: Schematic illustration of the Au/C-L**3**/Au junctions in in six contact points: (**1-3**), (**2-4**), (**1-2**), (**3-4**), (**1-4**), and (**2-3**). **Left panel:** Transmission coefficients $T(E)$ of Au/C-L**3**/Au junctions against electron energy E.

5.6.2 Transport simulation in Au-Au junction for cross-linked (4)

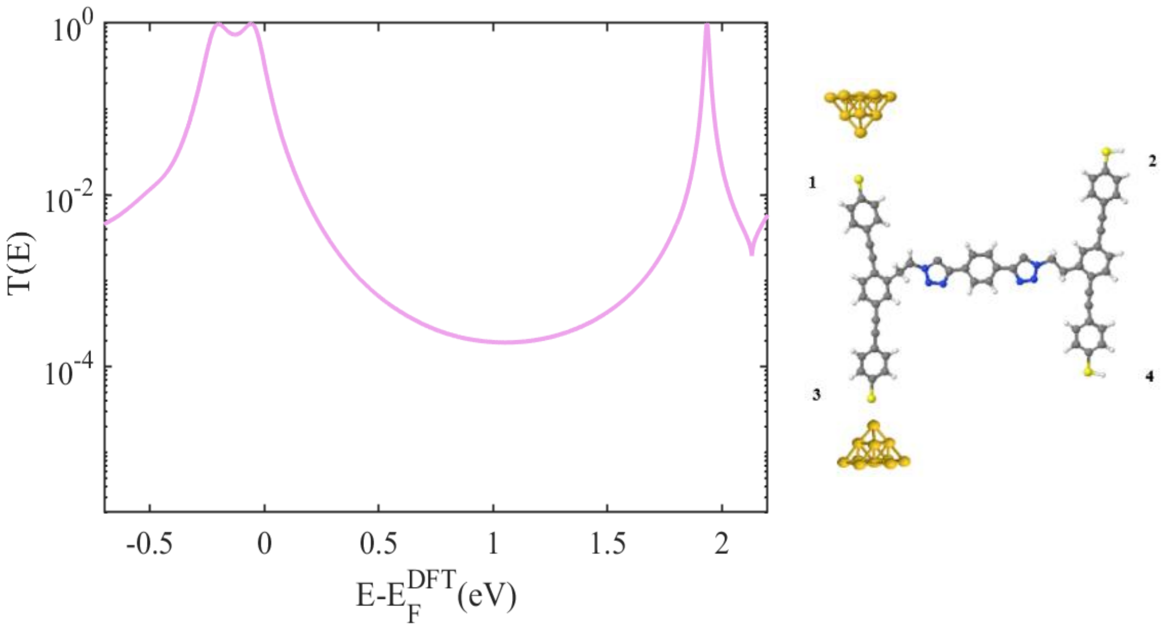

Figure 5. 16: Right panel: Schematic illustration of the Au/C-L**4**/Au junctions in (**1-3**) contact points. **Left panel**: Transmission coefficient $T(E)$ of Au/C-L**4**/Au junctions against electron energy E.

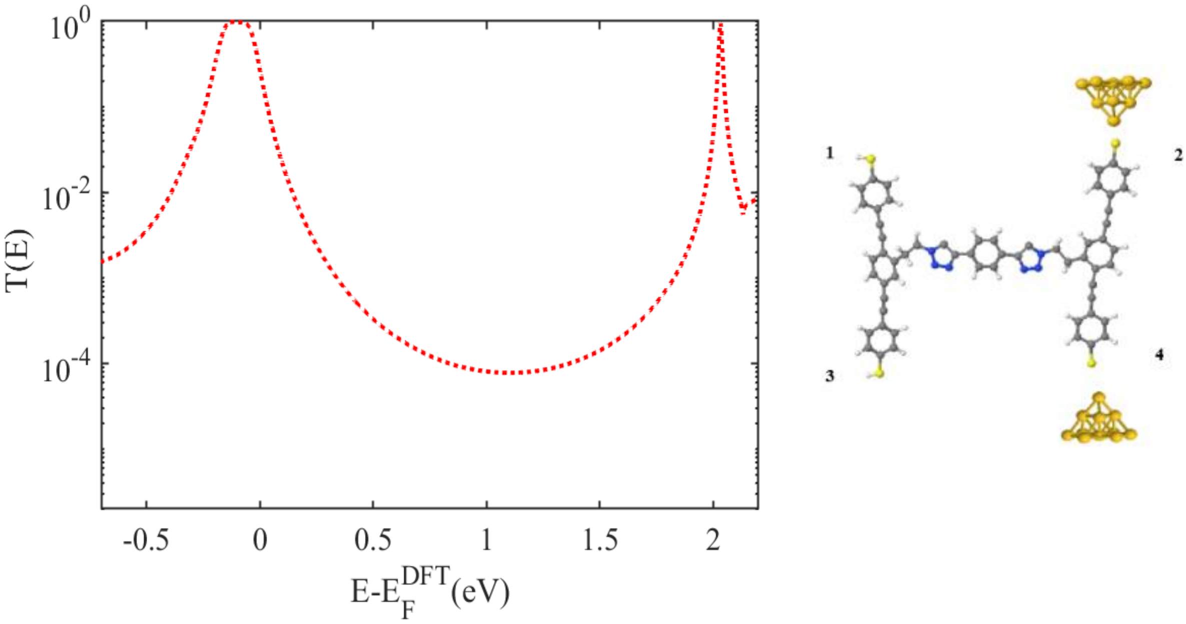

Figure 5. 17: Right panel: Schematic illustration of the Au/C-L**4**/Au junctions in (**2-4**) contact points. **Left panel**: Transmission coefficient $T(E)$ of Au/C-L**4**/Au junctions against electron energy E.

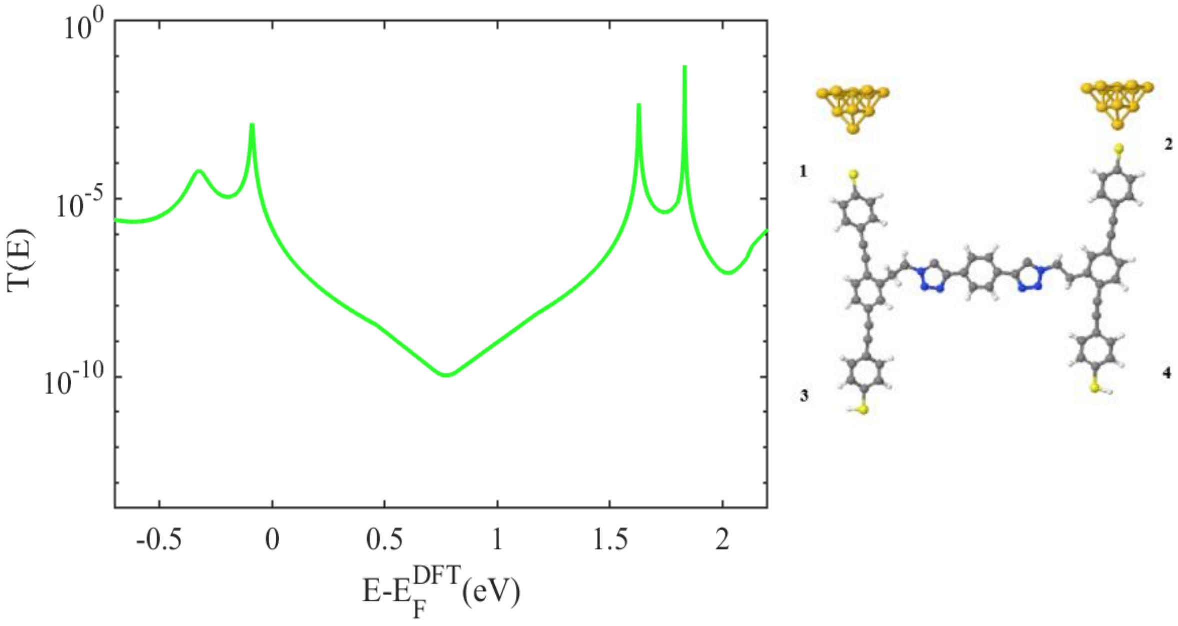

Figure 5. 18: Right panel: Schematic illustration of the Au/C-L**4**/Au junctions in (**1-2**) contact points. **Left panel**: Transmission coefficient $T(E)$ of Au/C-L**4**/Au junctions against electron energy E.

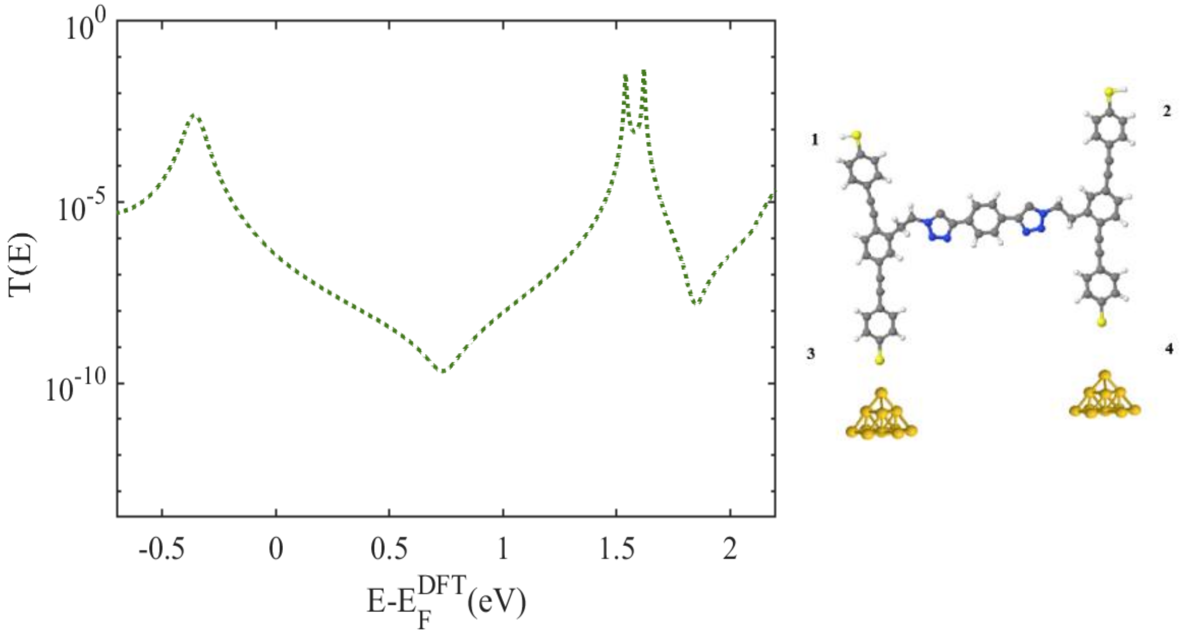

Figure 5. 19: Right panel: Schematic illustration of the Au/C-L**4**/Au junctions in (**3-4)** contact points. **Left panel**: Transmission coefficient $T(E)$ of Au/C-L**4**/Au junctions against electron energy E.

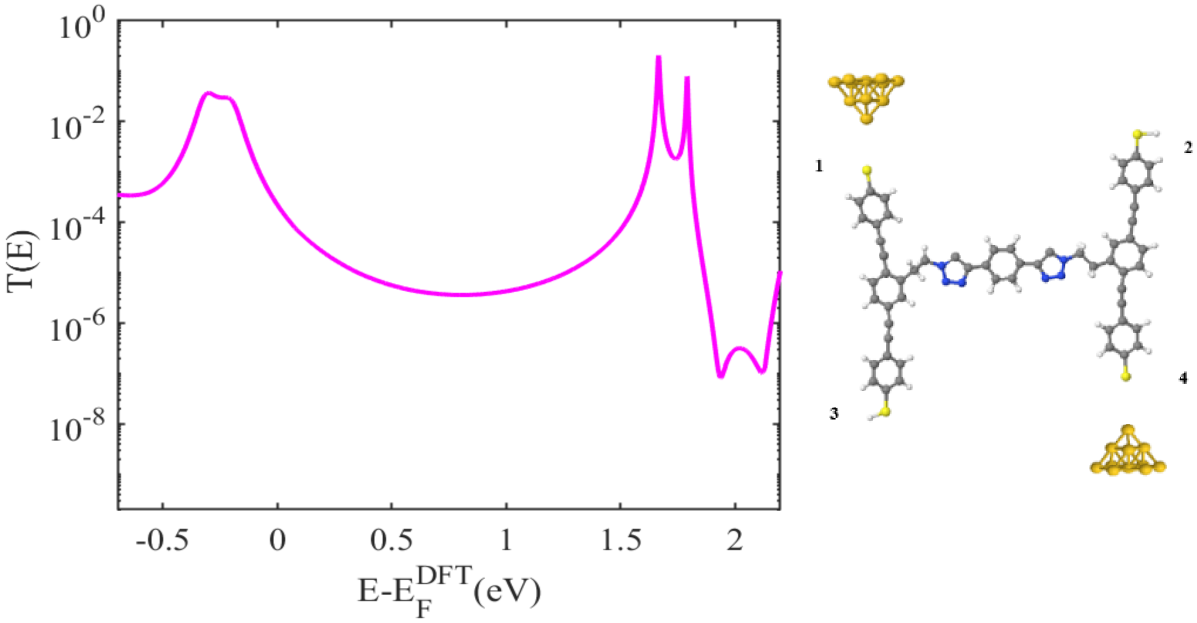

Figure 5. 20: Right panel: Schematic illustration of the Au/C-L**4**/Au junctions in (**1-4**) contact points. **Left panel:** Transmission coefficient $T(E)$ of Au/C-L**4**/Au junctions against electron energy E.

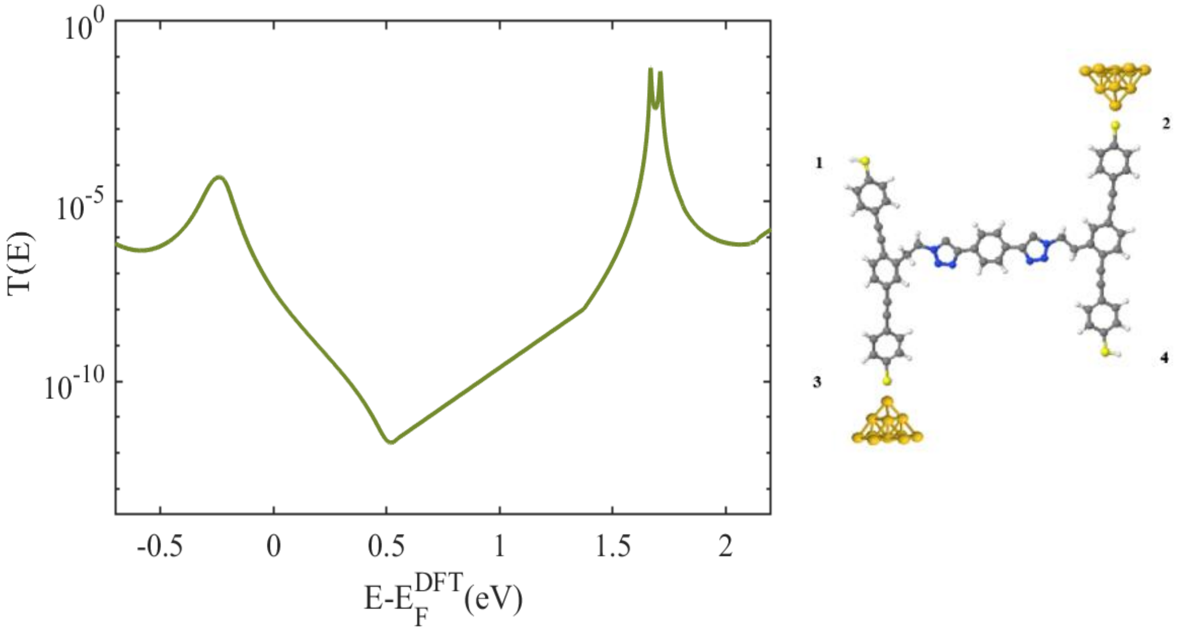

Figure 5. 21: Right panel: Schematic illustration of the Au/C-L**4**/Au junctions in (**2-3**) contact points. **Left panel**: Transmission coefficient $T(E)$ of Au/C-L**4**/Au junctions against electron energy E.

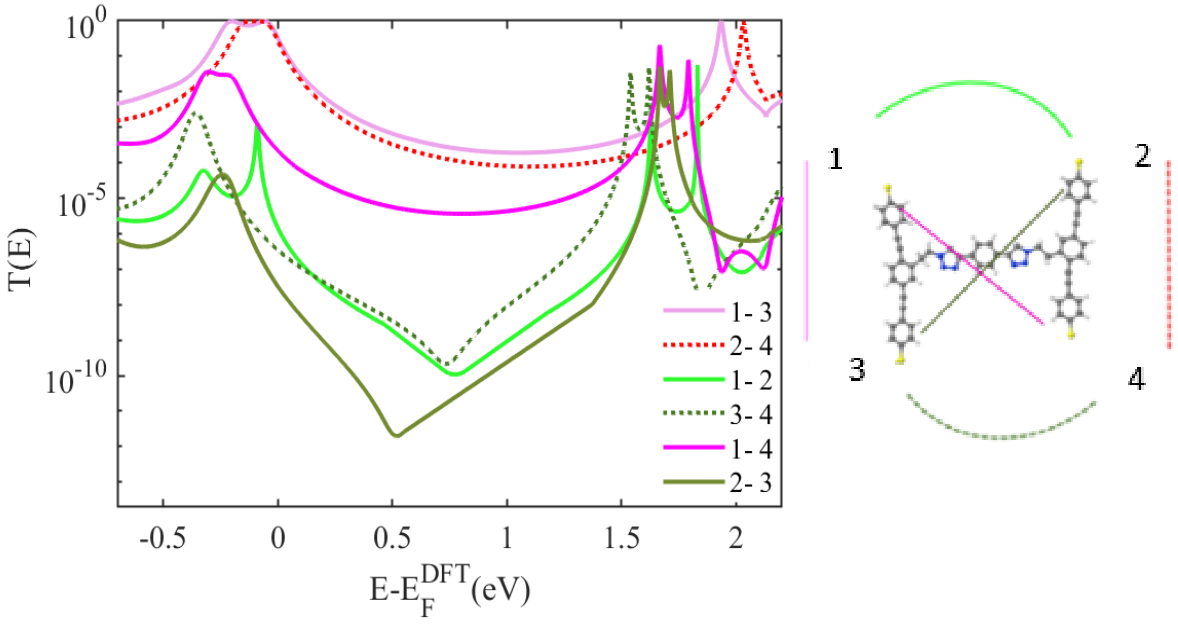

Figure 5. 22: Right panel: Schematic illustration of the Au/C-L**4**/Au junctions in in six contact points: (**1-3**), (**2-4**), (**1-2**), (**3-4**), (**1-4**), and (**2-3**). **Left panel:** Transmission coefficients $T(E)$ of Au/C-L**4**/Au junctions against electron energy E.

Table 5. 3 shows the DFT results indicate that the occurrence of destructive quantum interference DQI remains unaffected by the type of bridging linker. They also confirm that the **1-3**, **2-4**, and **1-4** connectivities exhibit high conductance due to constructive quantum interference CQI, whereas the **1-2**, **3-4**, and **2-3** connectivities show low conductance because of the presence of DQI [23-28].

Table 5. 3: DFT results for cross-linked **3** and **4**, in six different contact points (Note: C for constructive and D for destructive QI).

Cross-linked	Contact point	DFT results	Transmission Figures
C-L**3**	**1-3**, **2-4** **1-2**, **3-4** **1-4**, **2-3**	C, C D, D C, D	Figure 5. 9-Figure 5. 10 Figure 5. 11-Figure 5. 12 Figure 5. 13-Figure 5. 14
C-L**4**	**1-3**, **2-4** **1-2**, **3-4** **1-4**, **2-3**	C, C D, D C, D	Figure 5. 16-Figure 5. 17 Figure 5. 18-Figure 5. 19 Figure 5. 20-Figure 5. 21

5.7 TBM versus DFT

To compare the outcomes of the tight-binding model, I conducted density functional theory DFT transport simulations for the C-L**3** and C-L**4** dimers, considering six different electrode contact pairs for each. The TBM curves qualitatively align with the DFT-derived transmission coefficients, $T(E)$, for C-L**3** and C-L**4**, as illustrated in Figures 4.44 and 4.45. Both methods indicate that in the cases of **1-3**, **2-4**, and **1-4** connectivities, there is no evidence of destructive quantum interference, as no dip is observed. Conversely, for the **1-2**, **3-4**, and **2-3** connectivities, the dimers consistently switch between constructive quantum interference CQI and DQI, irrespective of the chemical structure of the bridging linker. A key qualitative difference between the DFT and TBM results arises from the nature of the TBM, which for C-L**1** and C-L**2** is based on a nearest-neighbor bipartite lattice. In this lattice, atoms are arranged so that odd-numbered atoms interact exclusively with even-numbered atoms, and vice versa. This inherent chiral symmetry ensures that the transmission coefficient is symmetric with respect to the electron energy E.

(a)

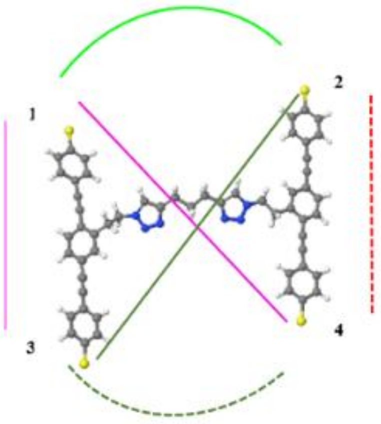

(b) TBM **(c) DFT**

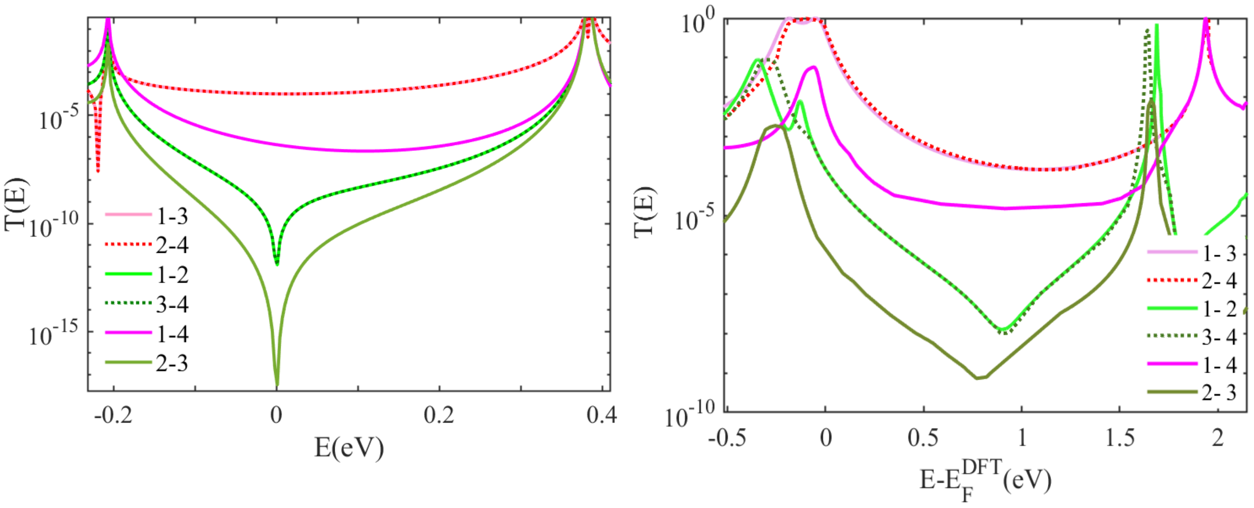

Figure 5. 23: (a): Schematic illustration of the Au/C-L**3**/Au junctions in in six contact points: (**1-3**), (**2-4**), (**1-2**), (**3-4**), (**1-4**), and (**2-3**). **(b):** Tight binding transmission coefficients $T(E)$ of 1D lead/C-**3**/1D lead. **(c):** Transmission coefficients $T(E)$ by DFT of Au/C-L**3**/Au junctions against electron energy E.

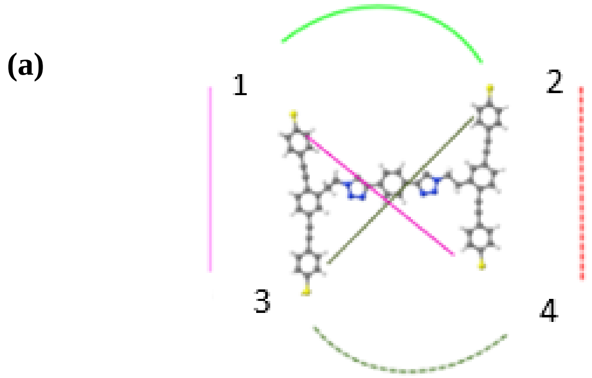

(b) TBM **(c) DFT**

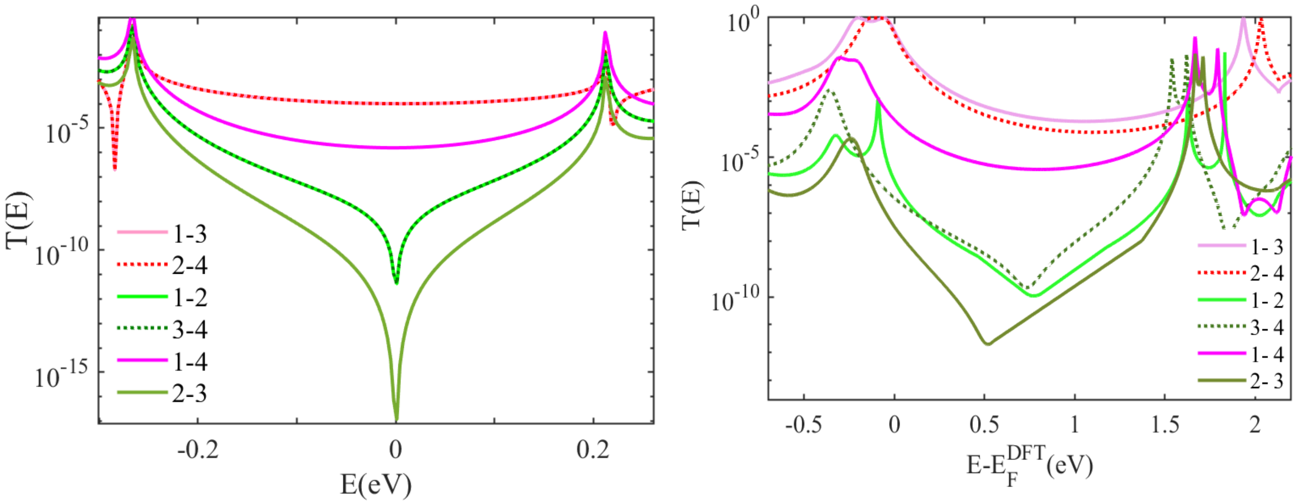

Figure 5. 24: (a): Schematic illustration of the Au/C-L**4**/Au junctions in in six contact points: (**1-3**), (**2-4**), (**1-2**), (**3-4**), (**1-4**), and (**2-3**). **(b):** Tight binding transmission coefficients $T(E)$ of 1D lead/C-**4**/1D lead. **(c):** Transmission coefficients $T(E)$ by DFT of Au/C-L**4**/Au junctions against electron energy E.

5.8 Checking OPR predictions by both DFT and TBM

Table 5. 4: Orbital product rule predictions for cross-linked **3**and **4**, against the DFT and TBM results (Note: ✓: OPR and DFT agree while x: OPR and DFT don't agree).

cross-linked	Contact points	OPR prediction	DFT & TBM	OPR and DFT-TBM agreement	wavefunction plot Figures
C-L**3**	**1-3**, **2-4** **1-2**, **3-4** **1-4**, **2-3**	D, C C, D D, C	C, C D, D C, D	x, ✓ x, ✓ x, x	Figure 5. 3(a) Figure 5. 3(a) Figure 5. 3(a)
C-L**4**	**1-3**, **2-4** **1-2**, **3-4** **1-4**, **2-3**	D, C C, D D, C	C, C D, D C, D	x, ✓ x, ✓ x, x	Figure 5. 4(a) Figure 5. 4(a) Figure 5. 4(a)

The results presented in **Table 5. 1** and **Table 5. 3** show a perfect 100% agreement between the tight-binding model TBM calculations and the density functional theory DFT results, highlighting the TBM's reliability and accuracy in modelling the system. However, as indicated in **Table 5. 4**, the agreement with the product rule is only partial, with less than 50% consistency. It should be noted that the OPR is not expected to work if there is a degeneracy in the energy levels. These dimers clearly display a degeneracies in both their HOMOs and LUIMOs levels. For example, in the case of C-L**3,** $E_{HOMO} = -4.56$ and $E_{HOMO-1} = -5.57\ eV$, $E_{LUMO} = -2.16$ and $E_{LUMO+1} = -2.05\ eV$ as shown in **Figure 5. 3** and in the case of C-L**4,** $E_{HOMO} = -4.70$ and $E_{HOMO-1} = -4.72\ eV$, $E_{LUMO} = -2.33$ and $E_{LUMO+1} = -2.11\ eV$ as shown in **Figure 5. 4**.

5.9 Seebeck behaviour of Au-dimer-Au junctions

The measurement of the Seebeck coefficient $S(E_F)$ in molecular junctions offers complementary information to conductance measurements and is becoming essential for understanding transport processes at the nanoscale. In this section, the thermoelectric properties of the molecules discussed in section (3.7), cross-linked **3** (C-L**3**) and cross-linked **4** (C-L**4**), are examined theoretically.

As note in chapter 4, the Seebeck coefficient is directly related to the slope of the logarithmic transmission coefficient at the Fermi level. In essence, the sign of the Seebeck coefficient $S(E_F)$ depends on the transmission function's slope at the Fermi energy E_F. When $S(E_F)$ is positive, it indicates that holes are the main charge carriers in transport. Conversely, a negative $S(E_F)$ suggests that electrons are primarily responsible for transport [29, 30].

Figure 5. 25 shows the Seebeck coefficient $S(E_F)$ evaluated at room temperature for different ranges $E_F - E_F^{DFT}$ for C-L**3**, while **Figure 5. 26**. By using DFT combined with the quantum transport code Gollum, the Seebeck coefficient $S(E_F)$ has been calculated. **Figure 5. 27** and **Figure 5. 28** shows how $S(E_F)$ varies as a function of the Fermi energy E_F. The thermopower has been calculated for the twelve junctions, where the $E_F = 0$.

5.9.1 Seebeck coefficient for cross-linked molecule C-L3

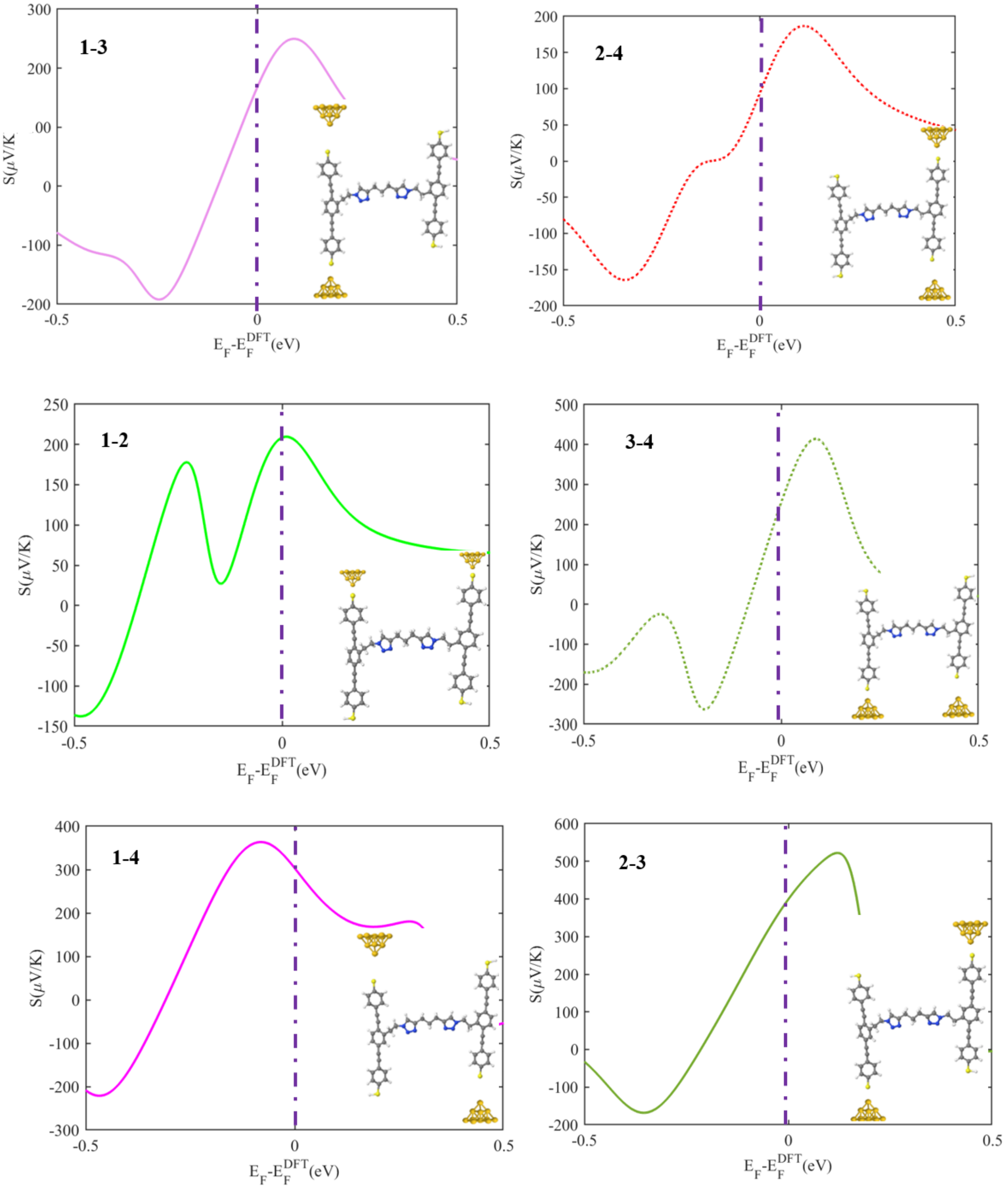

Figure 5. 25: The Seebeck behavior of the Au/C-L**3**/Au junctions in in six contact points (a) (**1-3**), (b) (**2-4**), (c) (**1-2**), (d) (**3-4**), (e) (**1-4**), and (f) **(2-3)**.

5.9.2 Seebeck coefficient for cross-linked molecule C-L4

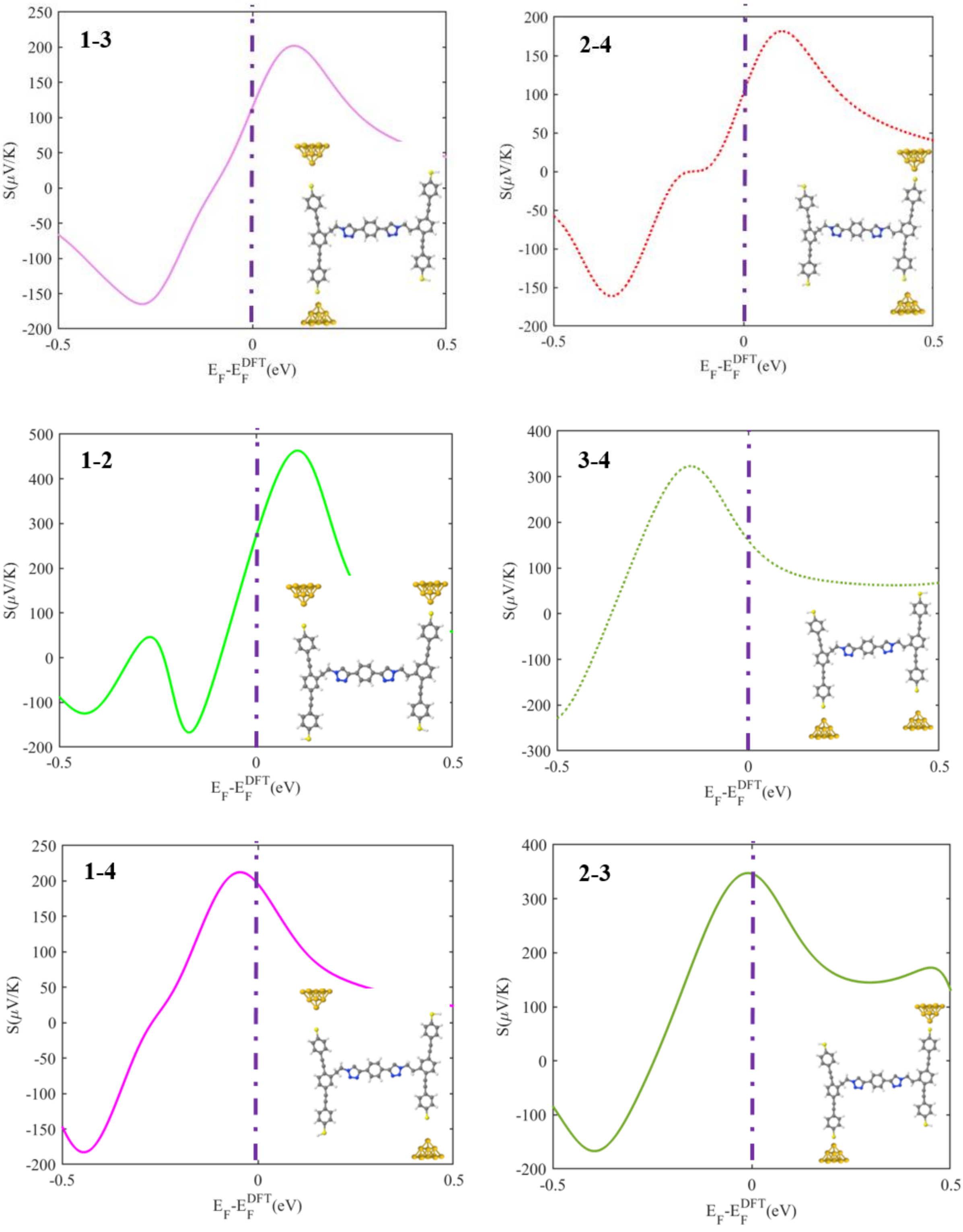

Figure 5. 26: The Seebeck behavior of the Au/C-L**4**/Au junctions in in six contact points (a) (**1-3**), (b) (**2-4**), (c) (**1-2**), (d) (**3-4**), (e) (**1-4**), and (f) **(2-3)**.

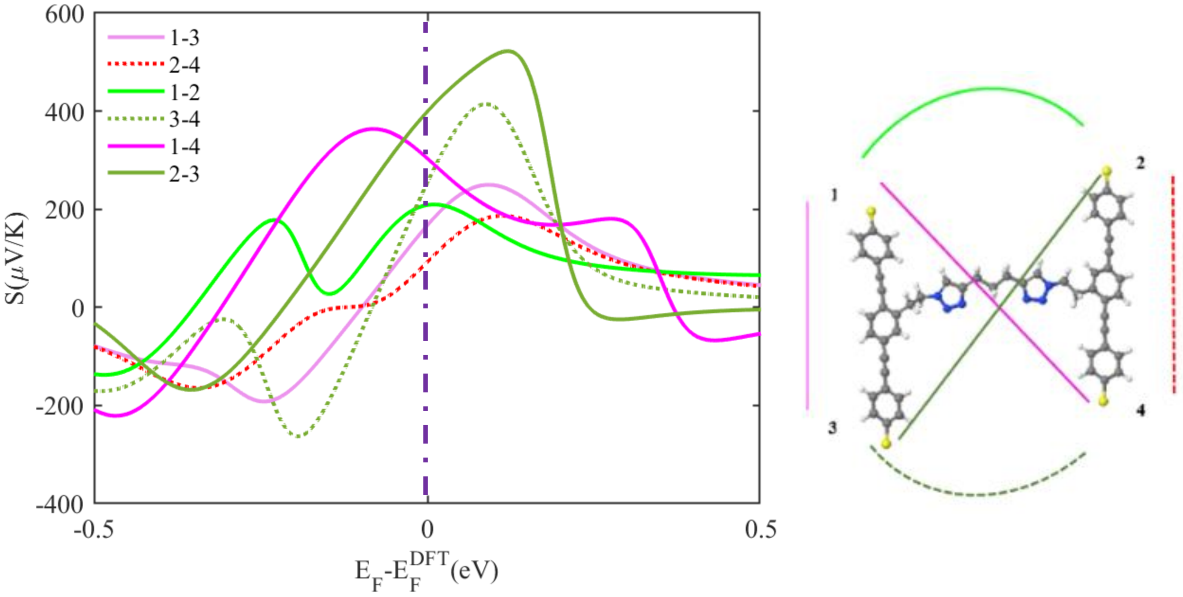

Figure 5. 27: Right panel: Schematic illustration of the Au/C-L**3**/Au junctions in in six contact points: (**1-3**), (**2-4**), (**1-2**), (**3-4**), (**1-4**), and (**2-3**). **Left panel:** Seebeck coefficient $S(E_F)$ of Au/C-L**3**/Au junctions against electron energy E.

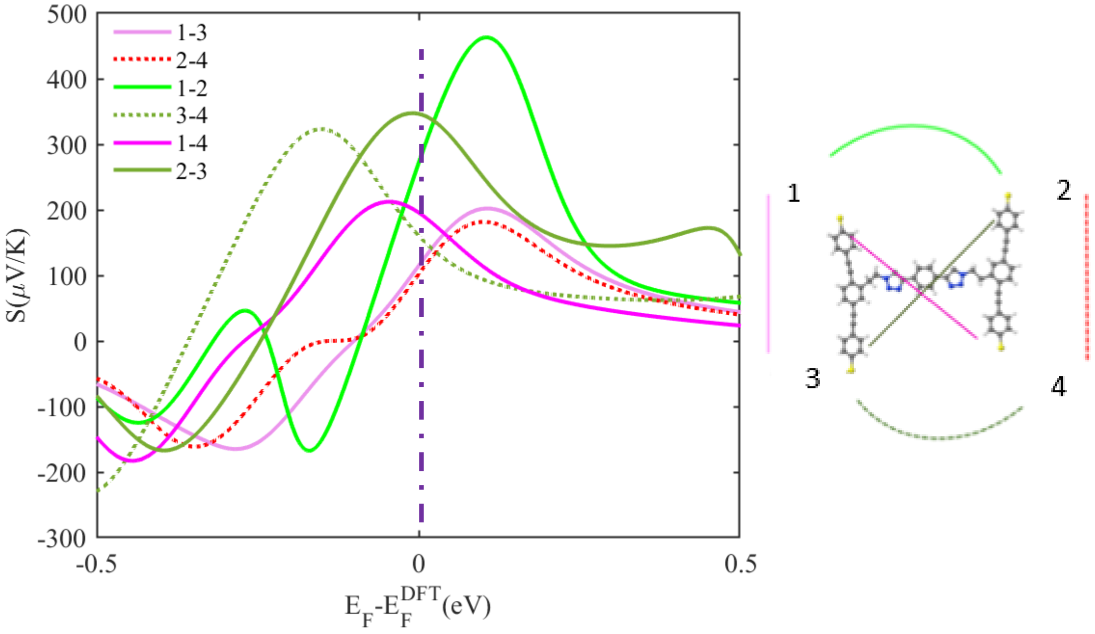

Figure 5. 28: Right panel: Schematic illustration of the Au/C-L**4**/Au junctions in in six contact points: (**1-3**), (**2-4**), (**1-2**), (**3-4**), (**1-4**), and (**2-3**). **Left panel:** Seebeck coefficient $S(E_F)$ of Au/C-L**4**/Au junctions against electron energy E.

Table 5.5 shows the Seebeck coefficient values at DFT-predicted Fermi $E_F - E_F^{DFT} = 0\ eV$ for the C-L**3** with six different options for thiol pair including **1-3**, **2-4**, **1-2**, **3-4**, **1-4**, and **2-3** which are in the range between 92.2 and $390\ (\mu V\ K^{-1})$ for contact point **2-4** *'Para-Para'* and contact point **2-3** *'meta-meta'*. The **2-4** '*Para-Para'* connectivity produces high conductance and low Seebeck coefficient, whereas the **2-3** *'meta-meta'* connectivity produces low conductance, and a high Seebeck coefficient. **Table 5.6** shows the Seebeck coefficient values at DFT-predicted Fermi $E_F - E_F^{DFT} = 0\ eV$ for the C-L**4** with six different options for thiol pair including **1-3**, **2-4**, **1-2**, **3-4**, **1-4**, and **2-3** which are in the range between 101 and $340\ (\mu V\ K^{-1})$ for **2-4** *'para-para'* and **2-3** *'meta-meta'*. For the **2-4** *'para-para'* connectivity, the conductance corresponds is high and the Seebeck coefficient is low, whereas for the **2-3** '*meta-meta'* connectivity, the conductance is low and, the high Seebeck coefficient is high.

So, the *'meta-meta'* connectivity involves more significant asymmetry or destructive quantum interference effects, enhancing the Seebeck coefficient. The higher value indicates stronger energy dependence of the transmission function near the Fermi level. The *'para-para'* connectivity might correspond to constructive quantum interference or better symmetry in the electronic coupling, leading to a lower Seebeck coefficient. The small value suggests a flatter energy dependence of the transmission near the Fermi level. These variations highlight how the quantum interference and contact geometry influence the thermoelectric properties of the molecule.

Table 5. 5: Seebeck coefficient $S(E_F)$ at DFT-predicted Fermi $E_F - E_F^{DFT} = 0\ eV$ for C-L**3**.

Compound	$S\ (\mu V\ K^{-1})$	Seebeck plot Figures
1-3	167	Figure 5. 23 (a)
2-4	92.2	Figure 5. 23 (b)
1-2	208	Figure 5. 23 (c)
3-4	225	Figure 5. 23 (d)
1-4	303	Figure 5. 23 (e)
2-3	390	Figure 5. 23 (f)

Table 5. 6: Seebeck coefficient $S(E_F)$ at DFT-predicted Fermi $E_F - E_F^{DFT} = 0\ eV$ for C-L**4**.

Compound	$S\ (\mu V\ K^{-1})$	Seebeck plot Figures
1-3	114	Figure 5. 24 (a)
2-4	101	Figure 5. 24 (b)
1-2	270	Figure 5. 24 (c)
3-4	160	Figure 5. 24 (d)
1-4	190	Figure 5. 24 (e)
2-3	340	Figure 5. 24 (f)

5.10 Conclusion

In this study, I investigated the influence of bridge on electronic transport, using the product rule, tight-binding model TBM, and density functional theory DFT calculations. In total, I have employed four different linker bridges (**1-4**), which involve linear chain (alkane), six-membered rings (benzene ring), 2(five-membered rings) with linear chain (oligophenylene vinylene), and 2(five-membered rings) with benzene ring **(**2,6-bis(2-pyridyl) benzene). I have found that the interference behaviour is mainly dictated by the connectivity to external electrodes rather than the bridge and depends on whether *meta*-connected phenyl rings are present in the transport pathway. This insight is expected to be a critical design consideration when synthesising molecules with cross-links of varying stiffness, as it allows the stiffness and phonon transport properties to be adjusted while preserving either constructive or destructive quantum interference.

I have also found that the quantum interference effects, contact geometry, and the alignment of molecular orbitals with the Fermi level strongly influence the Seebeck coefficient. Configurations that induce destructive interference or asymmetry tend to increase the Seebeck coefficient, while configurations with stronger symmetry or constructive interference reduce it. These results indicate that the specific nature of the cross-linking bridge does not significantly affect the observed outcomes. Instead, the connectivity, particularly the electron pathway from one electrode to the other, plays a crucial role in governing the system's behaviour.

5.11 Bibliography

[1] H. Tsuji, E. Nakamura, Carbon-bridged oligo (phenylene vinylene) s: a de novo designed, flat, rigid, and stable π-conjugated system, Accounts of Chemical Research, 52 (2019) 2939-2949.
[2] F. Grozema, L. Candeias, M. Swart, P.T. Van Duijnen, J. Wildeman, G. Hadziioanou, L. Siebbeles, J. Warman, Theoretical and experimental studies of the opto-electronic properties of positively charged oligo (phenylene vinylene) s: Effects of chain length and alkoxy substitution, The Journal of chemical physics, 117 (2002) 11366-11378.
[3] B. Soro, S. Stoccoro, G. Minghetti, A. Zucca, M.A. Cinellu, S. Gladiali, M. Manassero, M. Sansoni, Synthesis of the first C-2 cyclopalladated derivatives of 1, 3-Bis (2-pyridyl) benzene. Crystal structures of [Hg (NCN) Cl],[Pd (NCN) Cl], and [Pd2 (NCN) 2 (μ-OAc)] 2 [Hg2Cl6]. Catalytic activity in the Heck reaction, Organometallics, 24 (2005) 53-61.
[4] C.M. Finch, S. Sirichantaropass, S.W. Bailey, I.M. Grace, V.M. Garcia-Suarez, C.J. Lambert, Conformation dependence of molecular conductance: chemistry versus geometry, Journal of Physics: Condensed Matter, 20 (2007) 022203.
[5] A.K. Ismael, C.J. Lambert, Molecular-scale thermoelectricity: a worst-case scenario, Nanoscale Horizons, 5 (2020) 1073-1080.
[6] C.J. Lambert, S.X. Liu, A magic ratio rule for beginners: a chemist's guide to quantum interference in molecules, Chemistry–A European Journal, 24 (2018) 4193-4201.
[7] M. Famili, C. Jia, X. Liu, P. Wang, I.M. Grace, J. Guo, Y. Liu, Z. Feng, Y. Wang, Z. Zhao, Self-assembled molecular-electronic films controlled by room temperature quantum interference, Chem, 5 (2019) 474-484.
[8] Y. Li, M. Buerkle, G. Li, A. Rostamian, H. Wang, Z. Wang, D.R. Bowler, T. Miyazaki, L. Xiang, Y. Asai, Gate controlling of quantum interference and direct observation of anti-resonances in single molecule charge transport, Nature materials, 18 (2019) 357-363.
[9] R. Hoffmann, The many guises of aromaticity, Am. Sci, 103 (2015) 1511.
[10] N.R. Rajamohan, S.R. Ramanathan, S.R. Francis, Resolving set for line graph of linear benzene and polyphenyl structures, in: AIP Conference Proceedings, AIP Publishing, 2024.
[11] I.M. Grace, G. Olsen, J. Hurtado-Gallego, L. Rincón-García, G. Rubio-Bollinger, M.R. Bryce, N. Agraït, C.J. Lambert, Connectivity dependent thermopower of bridged biphenyl molecules in single-molecule junctions, Nanoscale, 12 (2020) 14682-14688.

[12] R.J. Davidson, D.C. Milan, O.A. Al-Owaedi, A.K. Ismael, R.J. Nichols, S.J. Higgins, C.J. Lambert, D.S. Yufit, A. Beeby, Conductance of ‘bare-bones’ tripodal molecular wires, RSC advances, 8 (2018) 23585-23590.

[13] A. Markin, A.K. Ismael, R.J. Davidson, D.C. Milan, R.J. Nichols, S.J. Higgins, C.J. Lambert, Y.-T. Hsu, D.S. Yufit, A. Beeby, Conductance Behavior of Tetraphenyl-Aza-BODIPYs, The Journal of Physical Chemistry C, 124 (2020) 6479-6485.

[14] A. Alshehab, A.K. Ismael, Impact of the terminal end-group on the electrical conductance in alkane linear chains, RSC advances, 13 (2023) 5869-5873.

[15] Y. Tsuji, E. Estrada, Influence of long-range interactions on quantum interference in molecular conduction. A tight-binding (Hückel) approach, The Journal of chemical physics, 150 (2019).

[16] M.T. González, A.K. Ismael, M. Garcia-Iglesias, E. Leary, G. Rubio-Bollinger, I. Grace, D. Gonzalez-Rodriguez, T. Torres, C.J. Lambert, N. Agrait, Interference controls conductance in phthalocyanine molecular junctions, The Journal of Physical Chemistry C, 125 (2021) 15035-15043.

[17] C. Bannwarth, E. Caldeweyher, S. Ehlert, A. Hansen, P. Pracht, J. Seibert, S. Spicher, S. Grimme, Extended tight-binding quantum chemistry methods, Wiley Interdisciplinary Reviews: Computational Molecular Science, 11 (2021) e1493.

[18] S. Grimme, C. Bannwarth, P. Shushkov, A robust and accurate tight-binding quantum chemical method for structures, vibrational frequencies, and noncovalent interactions of large molecular systems parametrized for all spd-block elements (Z= 1–86), Journal of chemical theory and computation, 13 (2017) 1989-2009.

[19] A.K. Ismael, 20-state molecular switch in a Li@ C60 complex, ACS omega, 8 (2023) 19767-19771.

[20] A.A. Al-Jobory, A.K. Ismael, Controlling quantum interference in tetraphenyl-aza-BODIPYs, Current Applied Physics, 54 (2023) 1-4.

[21] S.V. Aradhya, L. Venkataraman, Single-molecule junctions beyond electronic transport, Nature nanotechnology, 8 (2013) 399-410.

[22] L.A. Zotti, T. Kirchner, J.C. Cuevas, F. Pauly, T. Huhn, E. Scheer, A. Erbe, Revealing the role of anchoring groups in the electrical conduction through single-molecule junctions, small, 6 (2010) 1529-1535.

[23] D. Miguel, L. Alvarez de Cienfuegos, A. Martín-Lasanta, S.P. Morcillo, L.A. Zotti, E. Leary, M. Bürkle, Y. Asai, R. Jurado, D.J. Cárdenas, Toward multiple conductance pathways

with heterocycle-based oligo (phenyleneethynylene) derivatives, Journal of the American Chemical Society, 137 (2015) 13818-13826.

[24] G.C. Solomon, C. Herrmann, T. Hansen, V. Mujica, M.A. Ratner, Exploring local currents in molecular junctions, Nature Chemistry, 2 (2010) 223-228.

[25] A.K. Ismael, I. Grace, C.J. Lambert, Connectivity dependence of Fano resonances in single molecules, Physical Chemistry Chemical Physics, 19 (2017) 6416-6421.

[26] L. Herrer, A. Ismael, S. Martín, D.C. Milan, J.L. Serrano, R.J. Nichols, C. Lambert, P. Cea, Single molecule vs. large area design of molecular electronic devices incorporating an efficient 2-aminepyridine double anchoring group, Nanoscale, 11 (2019) 15871-15880.

[27] A.K. Ismael, C.J. Lambert, Single-molecule conductance oscillations in alkane rings, J Mater Chem C, 7 (2019) 6578-6581.

[28] T.L. Bennett, M. Alshammari, S. Au-Yong, A. Almutlg, X. Wang, L.A. Wilkinson, T. Albrecht, S.P. Jarvis, L.F. Cohen, A. Ismael, Multi-component self-assembled molecular-electronic films: towards new high-performance thermoelectric systems, Chemical Science, 13 (2022) 5176-5185.

[29] M. Alshammari, A.A. Al-Jobory, T. Alotaibi, C.J. Lambert, A. Ismael, Orientational control of molecular scale thermoelectricity, Nanoscale Advances, 4 (2022) 4635-4638.

[30] A.K. Ismael, I. Grace, C.J. Lambert, Increasing the thermopower of crown-ether-bridged anthraquinones, Nanoscale, 7 (2015) 17338-17342.

Chapter 6

Summary and future works

6.1 Introduction

This thesis has investigated electron transport through cross-linked OPE3 dimers, employing several theoretical techniques and methods such as the orbital product rule OPR, tight binding model TBM and density functional theory. The latter has allowed me to utilise the counterpoised method CP and examine frontier molecular orbitals (FMOs). Using density functional theory DFT, in combination with Green's function scattering techniques, their electrical conductance (G) and the Seebeck coefficient (S) have been evaluated with the aim of understanding fundamentals of their transport properties, which may underpin future designs for high performance thermoelectric materials. This thesis is composed of the following chapters:

Chapter 1 provided a brief overview of molecular electronics, incorporating a discussion on molecular junctions and outlining the structure of the thesis.

Chapter 2 introduced general concepts of density functional theory, its implementation of the SIESTA code, and the exchange correlation functional to analyse the electrical properties.

Chapter 3 described the single electron scattering theory equilibrium Green's functions, and relating topics such as Landauer formalism, with examples of calculating the transmission coefficient for different systems using the Hamiltonian and Green's functions.

Chapter 4 studied symmetric dimer molecules to demonstrate a general principle for

molecular-scale quantum transport (QI), which opens up new material design and discovery routes.

The density-functional theory was used to model the transport properties of the two molecular junctions. I investigated the charge transport properties of the *SH*-anchored molecular junctions, starting with the electronic structure properties involving the wave function plots and the binding geometry.

The two compounds, C-L**1** and C-L**2**, each have six connection points organised into two groups based on their connectivity patterns. These groups are defined as follows:

- CQI Group: the constrictive quantum interference group includes connections along the pathways **1-3**, **2-4**, and **1-4**.
- DQI Group: the distractive quantum interference group includes connections along the pathways **1-2**, **3-4**, and **2-3**.

This arrangement classifies the structural connectivity of C-L**1** and C-L**2** into these two distinct categories, CQI and DQI, based on their respective connection patterns.

Chapter 5 studied two new compounds, C-L**3** and C-L**4**. I found that the type of cross-linking bridges had no impact; however, the connectivity itself did influence the results.

6.2 Future work

This thesis used many theoretical methods to predict the electrical properties of different cross-linked dimers attached to gold leads. One may consider expanding these results in various directions for future work. One interesting study would be an assessment of transport properties when the cross-linked OPE3 dimers are terminated by other anchor groups such as pyridyl (*PY*), methyl sulphide (*SMe*), or amine (NH_2). Secondly, it would be interesting to examine the electronic properties of different electrodes such as cross-linked OPE3 dimers linked to a graphene lead.

Another suggestion for this chapter is to change the molecular core structure of the cross-linked dimer to have different contact connectivities; more specifically with a mixture of *paras, metas* and *orthos* pathways. For example, **Figure 6. 1** below, suggests four dimers (**b-e**), and elucidates how they differ from the origin dimer (**a**). These different mixtures of *paras, metas* and *orthos* pathways shall result in different values of on/off ratios which are necessary designing different types of memristives.

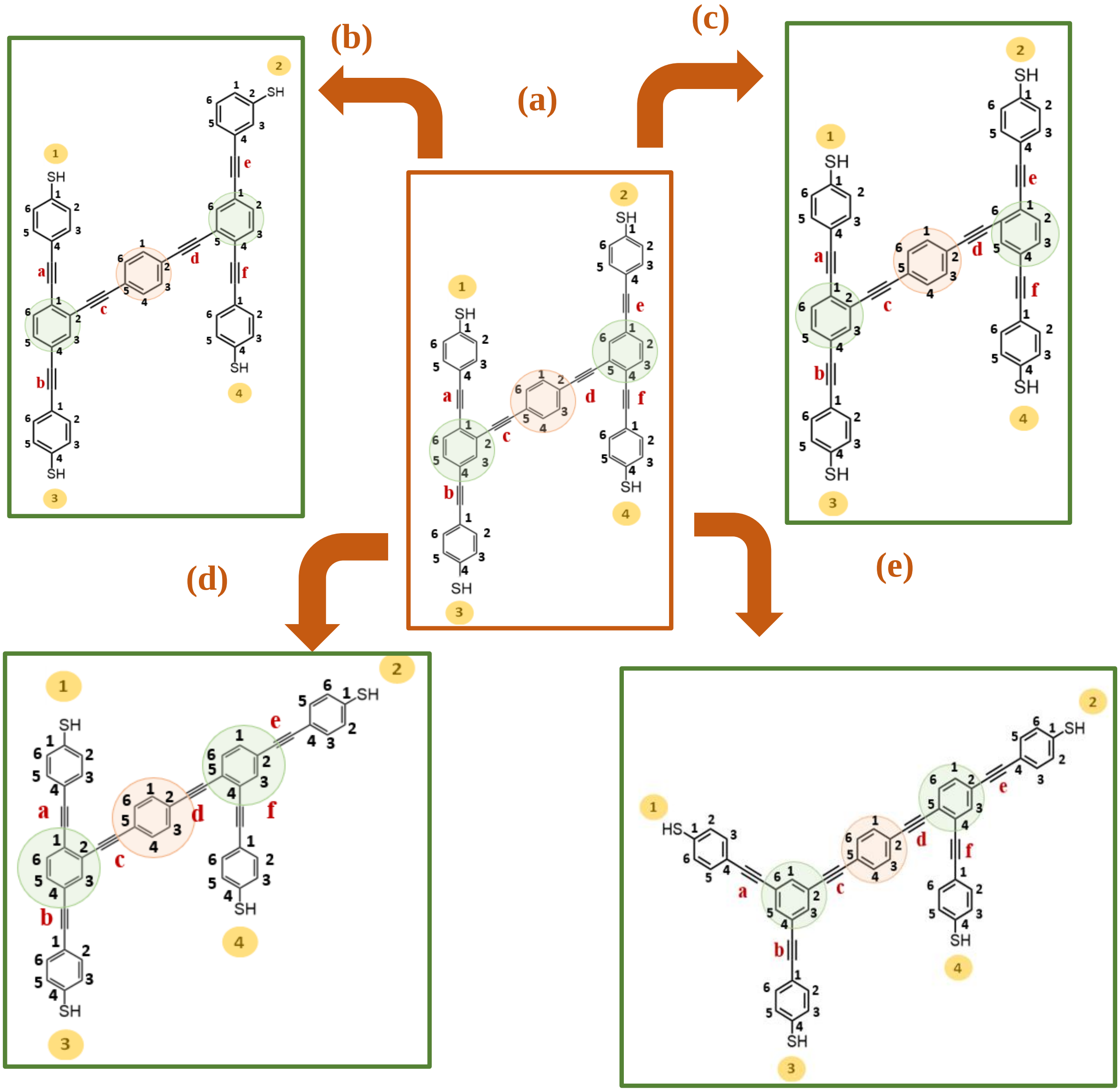

Figure 6. 1: (**a**) Schematic illustration of a dimer in six different contact points. (**b**, **c**, **d**, and **e**) new suggested dimers with different mixture of *paras, metas* and *orthos* pathways.

Figure 6. 1 shows the future work (**a**)Schematic illustration of a dimer in six different contact points. (**b**) the case when the thiol group connects to atom **2** instead of atom **1**, it changes from a para position to a meta position. (**c**) when the triple bond labelled '**d**' shifts to position **6** instead of **5**, it will yield a new outcome. (**d**) when the triple bond labelled '**e**' shifts to position **2** instead of **1**, it will result in new connectivities. In this study, I initially have three symmetric cases: *para-para*, *meta-meta*, and *ortho-ortho*, along with one asymmetric case, *meta-ortho*. However, with these changes, two additional asymmetries, *para-ortho* and *para-meta*, will emerge. Specifically, when electrons travel from position **1** to thiol **2**, this corresponds to a *para-ortho* asymmetry. On the other hand, if electrons travel from thiol **2** to thiol **3**, it results in a *para-meta*-asymmetry. (**e**) when the triple bond labelled '**a**' shifts to position **6** instead of **1**, and the triple bond labelled '**e**' shifts to position **2** instead of **1**, it will result in a new configuration.

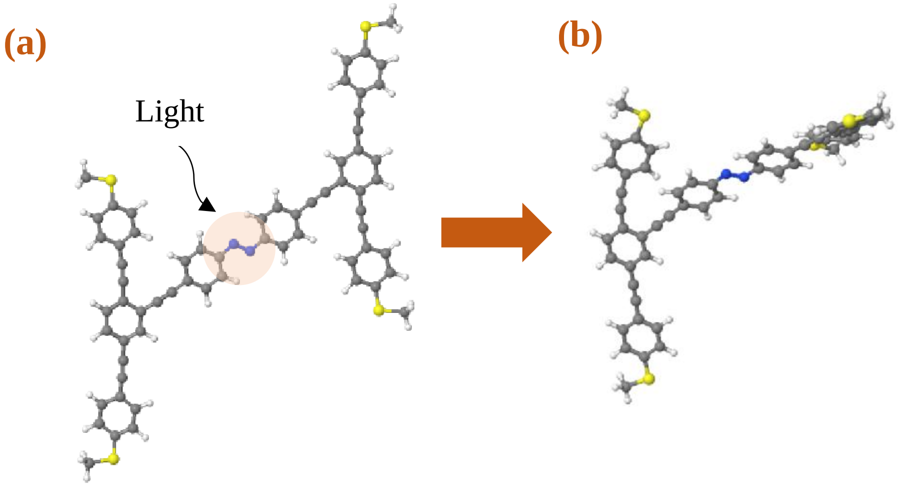

Figure 6. 2: (a) Schematic illustration of Cross-linked with Azobenzene. (b) Schematic illustration of cross-linked after rotation.

Furthermore, the molecular in **Figure 6. 2** was conducted in collaboration with Prof. Nicholas Long's group (Department of Chemistry, Imperial College London), who suggested the studied molecules used in this work. I performed the theoretical analysis at Lancaster. Since the position between the two benzene rings has an important influence on the electron transport due to quantum interference effects, I think that adding two nitrogen atoms (Azobenzene), may enhance the QI via an azobenzene bridge. Azobenzene is an organic compound consisting of two phenyl rings (benzene rings) connected by a central azo (-N=N-) group. It has the chemical formula $C_{12}H_{10}N_2$. Azobenzene is a well-studied compound in chemistry, mainly because of its photoisomerization properties, which make it a key player in materials science and molecular [1-4]. In addition to the above future work relating to electron transport, it would also be of interest to study how the above molecular features affect phonon transport, since there is a strong correlation between mechanical forces in molecular junctions and electrical conductance [5]. Based on theories of phonon transport in disordered solids [6], a DFT-based theory of phonon transport through molecules was developed recently and shown to be in excellent agreement with experimental measurements of single-molecule thermal transport [7]. Like DQI for electrons, theory suggests that phonon interference effects can be used to suppress phonon transport [8],which would be useful for increasing thermoelectric figure of merit ZT for molecular-scale junctions, which is proportional to the inverse of the thermal conductance.

6.3 Bibliography

[1] R.T. Ayinla, M. Shiri, B. Song, M. Gangishetty, K. Wang, The pivotal role of non-covalent interactions in single-molecule charge transport, Materials Chemistry Frontiers, 7 (2023) 3524-3542.
[2] H.D. Bandara, S.C. Burdette, Photoisomerization in different classes of azobenzene, Chemical Society Reviews, 41 (2012) 1809-1825.
[3] Y. Guo, M. Li, C. Zhao, Y. Zhang, C. Jia, X. Guo, Understanding Emergent Complexity from a Single-Molecule Perspective, JACS Au, 4 (2024) 1278-1294.
[4] Z. Mahimwalla, K.G. Yager, J.-i. Mamiya, A. Shishido, A. Priimagi, C.J. Barrett, Azobenzene photomechanics: prospects and potential applications, Polymer bulletin, 69 (2012) 967-1006.
[5] K. Yoshida, I.V. Pobelov, D.Z. Manrique, T. Pope, G. Mészáros, M. Gulcur, M.R. Bryce, C.J. Lambert, T. Wandlowski, Correlation of breaking forces, conductances and geometries of molecular junctions, Scientific reports, 5 (2015) 9002.
[6] G. Fagas, A. Kozorezov, C. Lambert, J. Wigmore, A. Peacock, A. Poelaert, R. Den Hartog, Lattice dynamics of a disordered solid-solid interface, Physical review b, 60 (1999) 6459.
[7] N. Mosso, H. Sadeghi, A. Gemma, S. Sangtarash, U. Drechsler, C. Lambert, B. Gotsmann, Thermal transport through single-molecule junctions, Nano letters, 19 (2019) 7614-7622.
[8] M. Famili, I. Grace, H. Sadeghi, C.J. Lambert, Suppression of phonon transport in molecular Christmas trees, ChemPhysChem, 18 (2017) 1234-1241.